Computational Modeling of Turbulent Ethanol Spray Flames in a Hot Diluted Coflow

Seyed Hossein Jamali

Master of Science Thesis

TU Delft Delft University of Technology

Computational Modeling of Turbulent Ethanol Spray Flames in a Hot Diluted Coflow

MASTER OF SCIENCE THESIS

For the degree of Master of Science in Mechanical Engineering at Delft University of Technology

Seyed Hossein Jamali

August 26, 2014

Faculty of Mechanical, Maritime and Materials Engineering (3mE) · Delft University of Technology


TU Delft
Delft
University of
Technology

DELFT UNIVERSITY OF TECHNOLOGY
DEPARTMENT OF
PROCESS AND ENERGY

The undersigned hereby certify that they have read and recommend to the Faculty of Mechanical, Maritime and Materials Engineering (3mE) for acceptance a thesis entitled

COMPUTATIONAL MODELING OF TURBULENT ETHANOL SPRAY FLAMES IN A HOT DILUTED COFLOW

by

SEYED HOSSEIN JAMALI

in partial fulfillment of the requirements for the degree of

MASTER OF SCIENCE MECHANICAL ENGINEERING

Dated: August 26, 2014

Supervisor(s):

Prof.dr. D.J.E.M. Roekaerts

Likun Ma, MSc

Reader(s):

Dr.ir. M.J.B.M. Pourquie

Dr.ir. Wiebren de Jong

Acknowledgments

I would like to express my sincere appreciation to my advisor Professor Dirk Roekaerts, for his valuable comments and guidance in the course of accomplishing the project. I would also like to thank my supervisor Mr. Likun Ma, for his patience and guidance from the first stages of my thesis.

Last but not least, I would like to thank my family, for their whole-hearted support through all stages of my study, as well as my friends, Arash, Ali, and Ahmadreza during studying at TU Delft.

Abstract

The phenomenon of turbulent spray combustion occurs in all industrial furnaces that consume liquid fuels. It is essential that a furnace is capable to have high efficiency and performance while the pollutant emissions meet the stricter national and international regulations. One of the recently proposed solutions to improve the aforementioned conditions is flameless spray combustion. In this process the combustion of fuel is done with oxidizer diluted with recirculated exhaust gases, which results in a lower peak temperature and more distributed reaction zone, so the NO_x produced in conventional burners is highly reduced. Hence, it can be a promising approach in order to increase efficiency and decrease pollutant emission. Because flameless combustion is a novel concept, it should be fully investigated and optimized before being applied to large-scale cases. Due to the considerable costs of experimental tests, numerical simulation is used more and more to predict the performance of the flameless furnaces before utilizing them in a real case.

The objective of this study is to develop and validate computational models for flameless spray combustion base on a validation study using the Delft Spray-in-Hot-Coflow (DSHC) flame. The burner has been designed to mimic the flameless oxidation of light oils. The properties of DSHC ethanol flames are computed by using a combination of CFD models for turbulence, chemistry and dispersed multiphase flow. The results are validated by comparison with the available experimental data for gas-phase velocity and temperature as well as droplets statistics. Furthermore, the experimental data are available for another case in which air is used instead of air diluted with exhaust gases. This case is also simulated to validate the models.

This study employs a Reynolds-Averaged Navier Stokes (RANS) simulation approach. The combination of different turbulence and combustion models is investigated while the standard Lagrangian spray model is kept the same. The steady flamelet and the Flamelet Generated Manifold (FGM) models are two combustion models that are validated. It is shown that the FGM model can predict flame structure such as double-reaction region, lift-off, etc. better than the steady flamelet model. Moreover, it was observed that the Reynolds stress and the realizable k-ε models show similar results while the standard k-ε model performs differently. The effects of other models and parameters are also investigated. The results show that radiative heat transfer, secondary atomization and coalescence of droplets as well as buoyancy have negligible effects on the DSHC ethanol flame. Still, the effects of complete two-way coupling between two phases (liquid and gas) are demonstrated to be important.

Contents

List of Figures

List of Tables

Chapter 1

Introduction

Nowadays the use of bio-fuels like ethanol has become a potential alternative to the use of fossil fuels. In spite of the fact that bio-fuels are extracted from renewable resources, how to use these fuels in burners is still an important question in order to prevent further production of pollutant emissions including unburnt Hydrocarbons and side products, and improve combustion efficiency. For instance, some of these harmful side products are carbon monoxide (CO), mono-nitrogen oxides (NO_x), nitrous oxide (N_2O), and soot. Moreover, there are quite a few number of parameters that affect the performance of a burner, so it is important to optimize those parameters in order to produce the least amount of pollutant emissions with the maximum efficiency of the burner.

Flameless combustion is a modification that may be applied to increase the efficiency of the combustion device and reduce NO_x formation. If the the fuel and oxidizer are injected with high momentum separately into a hot region to hinder the direct contact of the fuel and fresh air, the flameless combustion may occur. Under the high momentum, the strain rate is so high that under the conventional burner situations, the flame would extinguish; however, the surrounding hot temperature makes a stable flame (Danon 2011). Figure 1.1 shows the difference between these two types of burner. While the top figure demonstrates that the flame is stabilized near the injector with high flame temperature, the bottom figure gives a good representation on how the peak temperature near the injector is avoided.

The flameless spray combustion has been referred in different cases to as Excess Enthalpy Combustion (EEC), High Temperature Air Combustion (HiTAC), Flameless Oxidation (FLOX), Low NO_x Injection (LNI), or Medium or Intense Low-oxygen Dilution (MILD) combustion (Weber et al. 2005).

The correct control of the recirculation is a challenge on which the correct performance of the burner with a stable flame depends. Moreover, it can be charachterized with the following features (Wünning & Wünning 1997):

- It should provide strong recirculation rate.
- The temperature and species concentrations change smoothly without high gradients.
- At its optimal operation condition, no noise or flame are observed.
- Since high peak temperature is avoided, formation of thermal NO is suppressed.

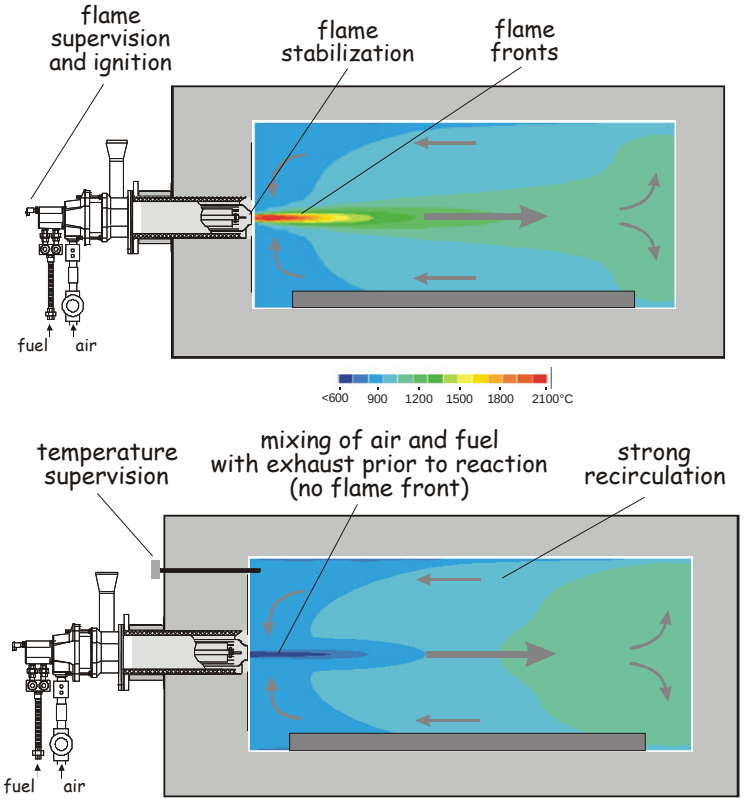

Figure 1.1: Two types of burners. Top image: a conventiaonl burner, bottom image: a flameless burner(Wünning 2003)

In this study, the flameless combustion has been studied using the Delft Spray-in-Hot-Coflow burner. Whereas the configuration of the burner is simpler than the real burners and the bounded surroundings, there are different challenges that are presented in this study. Since ethanol is used as the fuel, the spray processes such as injection, atomization, droplet evaporation should be taken into account; furthermore, the strong and complete two-way coupling between two phases is important for correct prediction of both phases. The effects of non-equilibrium in the chemistry as well as a detailed description of chemical reactions are important. Besides the liquid phase, how turbulence and chemistry interact with each other is another challenge that shapes the flame. Last but not least, the best trade off between the computational efficiency and the mathematical description of phenomena should be found (Gutheil 2011).

These are the challenges in the numerical simulation of turbulent spray combustion and they have been pointed out through this study. Therefore, it is important to briefly review the background of the current study from both the numerical and experimental points of view; then, the expectations can be reviewed at the end of this chapter.

1.1 Background

There are three types of modeling turbulent reacting flows: Direct Numerical Simulation (DNS), Large-Eddy Simulation (LES), and Reynolds-Averaged Navier Stokes (RANS). This thesis only focuses on the last method in which the turbulence is modeled rather than resolved. Moreover, there are different approaches to model combustion. Here, two combustion models are mainly considered: the steady flamelet and Flamelet Generate Manifold models. These two models along with RANS simulation is the backbone of this study. Furthermore, the fuel is supplied from the liquid phase, so it is important to consider the interaction between the liquid and gas phases. In what follows, the studies that have been done on combustion models, turbulent spray combustion, and ethanol chemical mechanism will be presented.

1.1.1 Combustion Models

In turbulent combustion whenever the thickness of the region, where chemical reactions occur, is much smaller than the turbulent length scale, the turbulent flame can be considered as a statistical ensemble of locally one-dimensional laminar flamelets, in which turbulent flow field wrinkles and stretches these laminar flamelet structures (Dixon-Lewis 1991). Peters (1984) proposed a complete formulation for the steady counterflow diffusion flamelet model, which will be referred to as the steady flamelet model in this study. In this formulation, the chemistry-turbulence interaction was split into two parts: the one-dimensional laminar diffusion flamelet, and the probabilistic behavior under the effects of turbulence. While each flamelet can be characterized by a scalar named the mixture fraction for its equilibrium condition, the non-equilibrium conditions caused by turbulence are included by a parameter named the scalar dissipation rate.

Although this method was firstly proposed for non-premixed combustion, it is possible to apply a similar approach to the premixed combustion (Peters 1986). The important criterion for this case is the smaller flame thickness compared to the turbulent length scale. The scalar used to define the flame propagation is progress variable; it can vary between 0 (unburnt mixture) and 1 (burnt mixture) to show the intermittency caused by the turbulent flow field.

Whereas the two aforementioned publications build the basis of the flamelet models; there have been a lot of investigations and improvements for the premixed and non-premixed cases. For instance, Müller et al. (1994) investigated the partially premixed turbulent flame through another formulation; they studied propagation speed and flame lift-off heights. Hollmann & Gutheil (1996) studied the turbulent spray flame of methanol with detailed chemical mechanism in which there are more species than a one-step reaction; this study included another phase (liquid methanol) to the system of equations and obtained good agreement with the experimental results. The work of Pitsch & Peters (1998) provided a comprehensive improvement to different aspects that had not been included in previous studies such as different species molecular diffusion coefficients, and different thermal and molecular diffusion coefficients. While all of these studies deployed the steady flamelet model, it is possible to use an unsteady approach; this approach is very effective to predict slow processes like NO_x formation (Pitsch et al. 1998).

One of the major improvements in the field of premixed combustion is considering the effects of slower processes rather than the assumption of quasi-equilibrium and steady-state conditions in the flamelet model. As described by (Warnatz et al. 2006), in a state space with N+2 dimensions representing N species mass fraction, pressure, and enthalpy, there are a lot of trajectories defining different processes with different time scales. However, the equilibrium state is a point in this state space, where all species, enthalpy and pressure have reached equilibrium after a long time. When the time scale is not so large that equilibrium state has been reached, and it is not so short that different trajectories are observed, all the processes can be explained by a line which is known as one-dimensional manifold. This is the main concept of the Flamelet Generated Manifold (FGM) model which combines the flamelet and manifold approaches (van Oijen & de Goey 2000) and (van Oijen et al. 2001).

While higher-dimensional manifolds were applied, good results were obtained through using only 1D manifold, in which the controlling variables were the progress variable and the enthalpy (considering energy loss) (van Oijen 2002). Bray et al. (2005) proposed that partially premixed combustion can also be described through the combination of the mixture fraction and progress variable. This is one of the approaches used in ANSYS Fluent to simulate partially premixed combustion. Despite the focus on RANS simulation, Chrigui et al. (2012) accomplished a study through LES and the FGM models, and employed detailed chemical mechanism for acetone to generate the FGM table from the mixture fraction and reaction progress variable. Based on correct prediction of droplets, the obtained gas-phase results were in fair agreement with the experimental results.

1.1.2 Turbulent Spray Combustion

The mentioned models and methods are mostly related to turbulent jet flames, where the fuel is gaseous; however, the turbulent spray combustion in which the fuel is liquid is the focus of the following section. There are two different approaches to consider the effects of the discrete phase; the first approach is to consider directly the effect of the discrete phase; therefore, the effects of droplet evaporation is added as source terms to the flamelet equations (Luo et al. 2013). Similarly, the turbulent spray combustion of ethanol was studied by Olguin & Gutheil (2014) considering the effects of droplets on the flamelet equations; both studies demonstrate the importance of evaporation on the structure of flame.

The second approach, which is investigated in this study and used by ANSYS Fluent, assumes that the flamelet or FGM table made from the gaseous fuel is still applicable and may be used as long as the gas and discrete phases are coupled completely. In the work of Rochaya (2007), Fluent 6.2 was used to solve the CFD problem. The steady flamelet model and the Reynolds stress model were used for combustion and turbulence modeling. Turbulence and combustion were coupled through a presumed β function. It was concluded that the default evaporation model (infinitely conductive model) overpredicts evaporation, so more sophisticated evaporation models should be considered. Furthermore, the steady flamelet model predicted temperature profiles inaccurately and it exaggerated the peak temperature. It should be noted that this study did not include radiaton or soot formation in spite of the luminous flame.

(Heye et al. 2014) studied the turbulent spray combustion for the Sydney burner with ethanol as the fuel; in this study, the results from four contributing groups which modeled similar configuration are shown. Three groups deployed LES and only one used the RANS simulation; moreover, the combustion models and evaporation models were different. The conclusion for different aspect of simulation was different; however, it was concluded that the evaporation model was definitely important; also, it is important to note that although RANS simulation failed to capture the flame spread and Reynolds stresses, the computational cost of LES should be considered when these two simulations are compared.

Moreover, results on the turbulent spray combustion of ethanol in a hot-diluted coflow are rare; the hot-diluted coflow is a way to simulate the flameless combustion. A first numerical study on the flameless spray combustion of ethanol was done by Ma et al. (2013) through deploying the presumed PDF steady flamelet model along with the Reynolds stress and k-ε models in ANSYS Fluent. While the discrete phase model as well as gas-phase velocities were in fair agreement with the experimental results, the steady flamelet model could not predict the flame lift-off.

The work of Ma et al. (2013) numerical results concern the experiments that were carried out on the Delft Spray-in-Hot-Coflow burner by Correia Rodrigues et al. (2014). These experiments were used also to validate another approach which considers directly solving the probability density function (Transported PDF). The results of this method along with the FGM model are given in the work of Ma et al. (2014). Since the current study does not use the transported PDF approach, further information on the difference of a presumed PDF and a transported PDF can be found on (Humza et al. 2014).

In the following part, the required detailed chemical mechanism to describe ethanol combustion is given, which is an input for both the steady flamelet and FGM models. In the next section, the experimental setup of the Delft Spray-in-Hot-Coflow (DSHC) burner is provided, that is the fundamental data for the present numerical simulation.

1.1.3 Ethanol Chemical Mechanism

The combustion of ethanol or any other fuel is a set of elementary reactions. The elementary reactions are split into three main categories: unimolecular, bimolecular, and trimolecular reactions, which have one, two, and three reactants, respectively. Therefore, the overall reaction of a fuel can be explained as a combination of these elementary reactions. For a general reaction of:

$$a_1R_1 + a_2R_2 + a_3R_3 + \cdots \longrightarrow b_1P_1 + b_2P_2 + b_3P_3 + \cdots$$

The lower case letters represent the stoichiometric coefficients of the reactants and products. According to the type of elementary reaction, some of the stoichiometric coefficients may be zero. Then, the rate of production or consumption of a species is calculated based on the type of the elementary reaction and the concentration of available species. For instance, the rate law for a trimolecular reaction with three different reactants is demonstrated in equation (1.1), in which the brackets represent the concentration of reactants.

$$\text{Rate of Reaction} = k[R_1][R_2][R_3] \tag{1.1}$$

Besides the concentration of reactants, the rate of reaction relies on the rate coefficient (k), which is obtained from Arrhenius' law (equation (1.2)).

$$k = AT^b \exp\left(\frac{E_a}{RT}\right) \tag{1.2}$$

In this equation, the coefficients A, b, and E_a are constant for a specific elementary reaction, so from these coefficients the rate of reaction for each species can be easily calculated for different temperatures; noted that the ratio of the activation energy (E_a) and the gas constant (R) may be directly provided in articles as T_a which has the dimension of temperature (K).

According to the characteristics of elementary reactions, the combustion at different temperature can be easily defined for a fuel by a set of elementary reactions, known as the chemical mechanism. Different chemical mechanisms have been proposed for the combustion of ethanol, each of which has been validated for a specific range of temperatures and air-fuel equivalence ratios. However, the main goal is to reduce the number of species and elementary reactions as much as possible with the least loss of accuracy. This reduction causes huge reduction in amount of computational costs and memory usage.

One of the most famous detailed chemical kinetic model for ethanol combustion was proposed by Marinov (1999). This model consists of 383 elementary reactions for 57 species. Moreover, the chemical mechanism proposed by (Röhl & Peters 2009), reduces the number of species and reactions to 38 and 228, respectively. As mentioned earlier, this is an advantage for the current numerical simulation since making the flamelet tables can take a lot of time as well as quite a bit space on the memory of the computer. This chemical mechanism was validated with correct prediction of ignition delay time for the equivalence ratios of 0.5, 1.0, and 2.0 along with different pressures ranging from 1 to 3.5 bar. Moreover, laminar burning velocities for different unburnt mixture temperatures and pressures were validated. The results show good agreement with the detailed mechanism.

There are also other chemical mechanisms proposed for ethanol combustion which are shown in table (1.1); although there are more chemical mechanisms, those used in recent articles are mainly mentioned in this table.

Table 1.1: Different chemical mechanisms of ethanol oxidation

Mechanism	Number of species	Number of reactions
Marinov (1999)	57	383
Saxena & Williams (2007)	46	235
Röhl & Peters (2009)	38	228
Okuyama et al. (2010)	46	215

The reduced chemical mechanism by Röhl & Peters (2009) was selected for accomplishing this project because of its smaller number of species while it was argued that the results do not deviate from the detailed chemical mechanism by Marinov (1999). The flamelet tables will be generated from this chemical mechanism by the CHEMKIN code, which is integrated in ANSYS Fluent.

1.2 Experiments

There are different groups around the world that have investigated the turbulent spray or turbulent spray combustion. Some of their experiments as provided by Jenny et al. (2012) are: University of Halle-Wittenberg experiments, UC Irvine combustion laboratory experiments, NIST reference spray combustion, UC Berkeley/University Heidelberg jet in coflow burner, CNRS Orleans pre-evaporation spray burner, Yale University experiments, and University of Sydney experiments. In this study, the experimental results from the Delft Spray-in-Hot-Coflow (DSHC) burner will be studied; therefore, in what follows, the setup and available experimental data are described briefly.

1.2.1 DSHC Burner Configuration

The first step in the experimental investigation is to define the burner configuration which then is used as a basis for the numerical simulation. A schematic view of the burner used for the experimental study of the flameless spray combustion is shown in figure (1.2). The main domain, which consists of the spray and combustion regions, is the region above the cylinder and pressure-swirl atomizer. It is necessary to mention that the outlet of the cylinder containing all the devices is named coflow in this study, in which the head of the injector is located and the flow can pass through.

The required liquid fuel is provided by a commercial pressure-swirl atomizer (Delavan WDB 0.5). For this atomizer, the exit orifice is 210 μm in diameter while the spray angle is 60°. This injector is completely surrounded with the cylinder whose diameter is 160 mm (Correia Rodrigues et al. 2014).

Another important task is to prepare the hot-diluted coflow in order to simulate the situation in a flameless furnace. Although it is possible to use the exhaust gases as the exit of the coflow, it is easier to use another burner for this purpose, which is more controllable; therefore, the secondary burner which is illustrated in the middle of figure (1.2) is employed to provide the necessary hot-diluted coflow with a specific oxygen-content. After injecting Dutch Natural Gas into the air passing through a honeycomb and two perforated plates, the combustion products with a specific temperature pass through two perforated plates, and enter the spray region. The effect of these perforated plates is to make the flow homogeneous as well as control the composition and temperature at the outlet.

Moreover, data gathering from the experimental setup is carried out using five different methods that are described briefly. The first method is Laser Doppler Anemometry (LDA) with which the gas-phase axial and radial velocities at the coflow are measured. The measurement is based on small difference in light frequency caused by light scattering when small particles of Aluminum Oxide (Al_2O_3) are moving with the same speed as the gas-phase. This method uses Mie scattering in which the particles' diameters are larger than the laser wave length and it is used for regions without droplets.

The next method is Phase Doppler Anemometry (PDA) which is used to measure droplet velocities and their size distribution. This method is based on the refraction of light by the liquid when the light passes through the droplet. For small-diameter droplets, the velocity of the particles can be a good representative of the gas-phase velocity, so the gas-phase velocity inside the spray and combustion domains is measured by the velocity of small droplets.

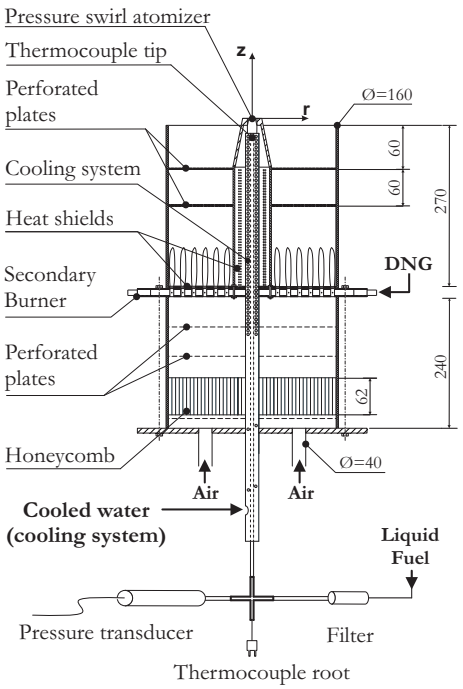

Figure 1.2: Schematic view of the DSHC burner (Correia Rodrigues et al. 2014)

In order to measure the gas-phase temperature, Coherent Anti-Stokes Raman Scattering (CARS) is used. This method is similar to Raman spectroscopy and because of its characteristics, it is a reliable method to measure the gas-phase temperature with high spatial and temporal resolution (Warnatz et al. 2006). Here, the temperature at boundaries and inside the combustion region is measured based on this technique.

The last two methods are high-speed visualization and flue gas analyzer. The former method is a way of capturing different shots from the spray under different conditions near the injector, so the effects of different parameters can be investigated on liquid injection, atomization, breakup, and evaporation. The latter measures oxygen volume fraction distribution at the coflow exit, where the head of the pressure swirl atomizer is located.

1.2.2 The Experimental Data

The burner may operate under different operating conditions; therefore, temperature, velocity, and other profiles adapt to the corresponding boundary and operating conditions. In this study two different cases are investigated. The first case, which is also known as SCHiii, deploys the secondary burner to supply hot air with low oxygen content at the coflow exit. The second case uses fresh air at the ambient temperature, known as SCCii.

According to the cases which will be used, it is important to know which set of information is necessary in order to define the operating conditions of the burner. The information required to specify the operating conditions of the DSHC burner can be split into two sets of information.

The first set is the necessary information regarding the pressure swirl atomizer operation. Either the pressure or the mass flow rate of the injector has to be assigned. These two parameters are correlated and it is not possible to change one without any change in the other.

The second data set for the burner is the boundary conditions of the gas-phase flow through the coflow. According to the DSHC burner geometry shown in figure (1.2), the coflow with a width of 160 mm provides the hot gases from the combustion products of the secondary burner in order to simulate the situation in a flameless burner; this is the operating condition of case 1 (SCHiii). Moreover, the coflow may provide fresh air which is the same as the ambient air to simulate the conventional burners; this is case 2 (SCCii).

Table 1.2: Experimental parameters of the injector for the investigated cases

Experiment	Case 1 (SHCiii)	Case 2 (SCCii)
Fuel mass flow rate (kg/hr)	1.5	1.7
Pressure (bar)	11.5	12.3
Coflow mean temperature (K)	1390	293
Coflow mean velocity (m/s)	2.5	0.29
Coflow oxygen volume fraction (%)	8.7	21

After specifying the operating condition of the injector, and the boundary conditions at the coflow, the system is completely specified, and the results recorded through time for the instantaneous temperature and velocity components are the raw data. Further postprocessing of these data is necessary to obtain other experimental results including the mean temperature, mean velocities, Reynolds stresses, etc. Figure (1.3) shows two different flames according to two different boundary conditions. The left figure was obtained when the boundary conditions for case SCCii were set, and the coflow is cold. The right figure shows when the boundary conditions of case SHCiii are set; this can also be interpreted as the flameless combustion that the air is preheated and diluted with combustion products.

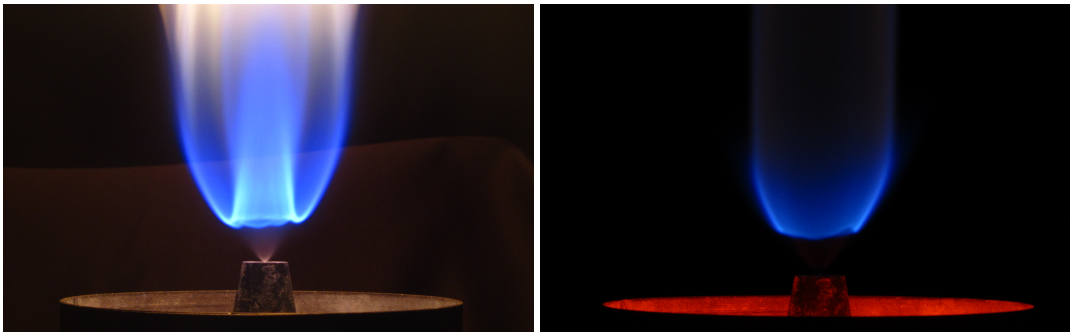

Figure 1.3: Images of different flames. Left image: cold coflow case (SCCii), right image: hot-diluted coflow case (SHCiii)

1.3 Problem Definition

According to what has been presented above, and the challenges in the field of turbulent spray combustion, the aim of this study is to investigate the RANS simulation of the hot-diluted coflow using two combustion models: the steady flamelet model as well as the Flamelet Generated Manifold model. These models are combined with three different turbulence models: the Reynolds stress model, the standard k-ε model, and the realizable k-ε model. The turbulence and combustion models as well as the discrete phase model will be studied through ANSYS Fluent 15. In a similar approach as mentioned by Rochaya (2007), the effects of radiation are neglected, and the models integrated in ANSYS Fluent will be considered.

The results for the hot-diluted coflow case will be compared with the experimental data from the DSHC burner. Whereas the main aim is to simulate the hot-diluted coflow case, the models will be investigated for the cold coflow case as well. Meanwhile, the following points have to be investigated through this study:

- The accuracy of the combustion models in both cases
- The accuracy of the turbulence models in both cases
- The effects of different sub-models or parameters that may or may not cause any difference in the final result of the hot-diluted coflow
- The main factors that may cause deficiency in numerical simulations
- A brief comparison between the capability of models to predict accurately for both the hot-diluted and cold coflow cases

1.4 The Outline

In the former sections, the background of spray turbulent combustion were reviewed briefly, and the experimental setup and its results were stated. Henceforth, based upon these important data, the numerical simulation should be carried out.

Chapter 2 reviews the theoretical approaches of the main models used in this study: turbulence, combustion, and discrete phase models. Considering the complicated theories and extensive derivation of equations, the models will not be derived in this chapter and only the models are explained.

However, how these models can correctly predict the experimental results is the main focus, that also includes validating a model as well as the combination of models. Therefore, the models are validated for two cases based on available experimental data, which is covered in chapter 3. Finally, the gist of what has been accomplished is explained in the final chapter. Furthermore, some recommendations for the future studies are given that may result in improvement of the numerical simulation and better agreement with the experimental data.

Chapter 2

Computational Models

The turbulent spray combustion is a combination of different phenomena. These phenomena consist of the flow and the corresponding turbulence, chemical reactions, the interaction between turbulence and the chemistry, radiative heat transfer, liquid fuel atomization, droplet dispersion and evaporation, and the interaction between the gas-phase flow and the liquid-phase flow. The Main focus of this project is on the turbulence, combustion, and discrete phase models.

Turbulence deals mainly with how the turbulence is modeled since the focus of this study is on RANS simulation. Two models are chosen for turbulence simulation: k-ε model and Reynolds Stress Model (RSM). The former one is the most famous model which is used in most turbulent flows while the latter is the most elaborate and comprehensive model used in RANS simulation.

Combustion models describe the chemical reactions that occurs during combustion. It is possible to model the chemical reactions completely or use models corresponding to the type of flame: premixed, non-premixed, or partially premixed flames. Moreover, turbulence affects the flame and it may wrinkle or stretch the flame; these effects are described by the turbulence-chemistry interaction, which is a part of the combustion modeling.

Finally, the fuel used in this project is liquid, and cannot burn until it evaporates and mixes with the gas-phase oxidizer; therefore, the discrete phase model (DPM) is deployed to consider all the changes arising from the injection of the liquid fuel to its evaporation. This consists of spray models such as atomization, dispersion, and the coalescence of droplets; after evaporation, the mixing process is carried out by the turbulence. Furthermore, the interaction between the gas phase and the liquid phase is important inasmuch as both the phases affect each other through mass, momentum, and heat transfer. Heat transfer reduces the energy of the gas phase while increasing the energy and temperature of the droplet and making the droplet to evaporate; the drag force causes the transfer of momentum and change in the turbulent flow as a sink or source term. Through evaporation and mass transfer from the liquid phase to the gas phase, the evaporated fuel then becomes ready to be mixed with the oxidizer; then, the mixture can ignite and burn. There are different models for each of these phenomena to be considered.

In the following sections, firstly the governing equations for the gas phase are discussed; then, models necessary to close the system of equations are explained. The final section is allocated to the discrete phase model.

2.1 The Governing Equations

The starting point for solving any laminar or turbulent flow is to define the domain and the corresponding boundary conditions; afterwards, the Navier-Stokes equations are applied to this specific problem. For a three-dimensional flow, at least four equations are needed: a continuity and three momentum equations. If there is heat loss/gain or any sort of temperature variation in the domain, an additional equation is necessary to describe the changes in the energy levels. Hence, there are five partial differential equations to describe the three-dimensional flow.

When the flow is reactive, some species are consumed and some others are produced; additional transport equations are necessary to describe this production or consumption of species. This means that if there are N species reacting in the whole domain, the total number of partial differential equations will increase to N+4.

The continuity, momentum, species, and energy equations are shown in equations (2.1a) to (2.1d).

$$\frac{\partial \rho}{\partial t} + \frac{\partial}{\partial x_j}(\rho u_j) = 0 \tag{2.1a}$$

$$\frac{\partial}{\partial t}(\rho u_i) + \frac{\partial}{\partial x_j}(\rho u_i u_j) = -\frac{\partial p}{\partial x_i} - \frac{\partial T_{ij}}{\partial x_j} + \rho g_i \tag{2.1b}$$

$$\frac{\partial}{\partial t}(\rho Y_k)\,\frac{\partial}{\partial x_j}(\rho Y_k u_j) = -\frac{\partial J_{k,j}}{\partial x_j} + \dot{\omega}_k \tag{2.1c}$$

$$\frac{\partial}{\partial t}(\rho h) + \frac{\partial}{\partial x_j}(\rho h u_j) = -\frac{\partial q_j}{\partial x_j} + Q + \ldots \tag{2.1d}$$

In this set of equations, ρ, u, Y, and h are density, velocity, species mass fraction, and enthalpy; indices i and k are defined to distinguish velocity components and different species. These are the main variables of the governing transport equations, and the equation of state is also needed to close the system of equations. Furthermore, p, q_j, and $J_{k,j}$ are pressure, diffusion flux, and heat flux. T_{ij} is the viscous part of the pressure tensor (equation (2.2)). The last terms on the right hand side of the equations present the source terms. g_i shows the sum of body forces as well as the gravity acting on the fluid; $\dot{\omega}_k$ determines the rate of production or consumption of species k. Q is the total heat loss/gain in the control volume through radiation, phase change, or any sort of heat loss/gain. It should be noted that during the derivation of enthalpy equation, some new terms appear which are not shown in equation (2.1d).

$$T_{ij} = -\mu\left(\frac{\partial u_i}{x_j} + \frac{\partial u_j}{x_i} + \frac{2}{3}\mu\frac{u_k}{x_k}\delta_{ij}\right) \tag{2.2}$$

There are three main methods to solve the set of equations (2.1) for turbulent reactive flows: Direct Numerical Simulation (DNS), Large Eddy Simulation (LES), and Reynolds Averaged Navier-Stokes (RANS). In this study the focus is only on the RANS simulation. Before explaining the averaged equations, it is important to note that for a value f which is arbitrary, $\overline{f}$ and f' represent the mean value and its fluctuation; however, the density weighted mean and its fluctuation are indicated by $\widetilde{f}$ and f'' as equation (2.3).

$$\widetilde{f} = \frac{\overline{\rho f}}{\overline{\rho}} \tag{2.3a}$$

$$f'' = f - \widetilde{f} \tag{2.3b}$$

When equation (2.1) is averaged over time, new terms appear that are functions of not only the mean values, but also their fluctuations. After time-averaging and simplifying, the results are given in equation (2.4). The species mass fractions and enthalpy given in equations (2.1c) and (2.1d) are combined to make equation (2.4c). ϕ_k represents the N species of the chemical mechanism as well as the enthalpy.

$$\frac{\partial \overline{\rho}}{\partial t} + \frac{\partial}{\partial x_j}\left(\overline{\rho}\widetilde{u_j}\right) = 0 \tag{2.4a}$$

$$\frac{\partial}{\partial t}\left(\overline{\rho}\widetilde{u_i}\right) + \frac{\partial}{\partial x_j}\left(\overline{\rho}\widetilde{u_i}\widetilde{u_j}\right) = -\frac{\partial \overline{p}}{\partial x_i} - \frac{\partial \overline{T_{ij}}}{\partial x_j} + \overline{\rho} g_i - \frac{\partial}{\partial x_j}\left(\overline{\rho}\widetilde{u_i'' u_j''}\right) \tag{2.4b}$$

$$\frac{\partial}{\partial t}\left(\overline{\rho}\widetilde{\phi_k}\right)\frac{\partial}{\partial x_j}\left(\overline{\rho}\widetilde{\phi_k}\widetilde{u_j}\right) = -\frac{\partial \overline{J_{k,j}}}{\partial x_j} + \overline{\rho}\widetilde{S_k} - \frac{\partial}{\partial x_j}\left(\overline{\rho}\widetilde{\phi_k'' u_j''}\right) \tag{2.4c}$$

In this set of equations, new terms appear that are related to the fluctuation of variables u_i and ϕ_k. While $\widetilde{u_i'' u_j''}$ represents one component of the Reynolds stress tensor, $\widetilde{\phi_k'' u_j''}$ is named turbulent scalar flux. Furthermore, $\overline{\rho}\widetilde{S_k}$ is the mean source term, which specifies species production/consumption as well as heat loss/gain. These three new terms are unknown and before solving the set of equations (2.4), they must be modeled. The last term, the mean source term, needs special attention to be calculated since it is strongly non-linear and changes dramatically as the local temperature fluctuates; this is in contrast to the other source terms which can be specified only as the function of local mean values.

These three terms make the closure problem related to RANS simulation. Hence, a different modeling is necessary to close the system of equations for each term. In the following sections, the models used to solve the closure problem are explained.

2.2 Turbulence

The Reynolds stresses introduced in equation 2.4b are the nine components of the Reynolds stress tensor that are unknown according to the mean velocity of the flow; therefore, quite a few models have been introduced in order to model the Reynolds stresses, and as a result, solve the closure problem in momentum equations.

There are two famous turbulence models which are discussed here to solve the closure problem of momentum equation: k-ε and Reynolds Stress models (RSM). The first model is predominantly used in most of the turbulent flow simulations because of its simplicity while the latter is the most comprehensive model for RANS simulation. A brief description of them are given in the following part. The detailed description of these two models are explained by Pope (2000). Furthermore, all equations solved by ANSYS Fluent and their important points can be found in ANSYS (2013).

2.2.1 k-ε Model

As mentioned earlier, this model is the most famous turbulent modeling whereas it is argued that its accuracy is lower compared to the RSM, and it can correctly predict the flow only in a limited number of cases, in which the flow is completely isotropic. The turbulent viscosity is calculated according to equation (2.5).

$$\nu_T = C_\mu k^2/\varepsilon \tag{2.5}$$

where C_μ is the model constant while k (turbulent kinetic energy) and ε (rate of dissipation of turbulent kinetic energy) are the variables of this model. In order to completely specify these variables, two transport equations for k and ε are solved. Therefore, two additional equations are added to the set of equations to solve the turbulence closure problem. If G is the rate of turbulent kinetic energy production, for instance buoyancy effect, the transport equations for turbulent kinetic energy and turbulent dissipation rate are given in equations (2.6) and (2.7) (ANSYS 2013).

$$\frac{\partial}{\partial y}(\overline{\rho}k) + \frac{\partial}{\partial x_j}(\overline{\rho}k\widetilde{u_j}) = \frac{\partial}{\partial x_j}\left[\left(\mu + \frac{\mu_t}{\sigma_k}\right)\frac{\partial k}{\partial x_j}\right] + G_k + G_b - \overline{\rho}\varepsilon - Y_M + S_k \tag{2.6}$$

$$\frac{\partial}{\partial y}(\overline{\rho}\varepsilon) + \frac{\partial}{\partial x_j}(\overline{\rho}\varepsilon u_j) = \frac{\partial}{\partial x_j}\left[\left(\mu + \frac{\mu_t}{\sigma_\varepsilon}\right)\frac{\partial \varepsilon}{\partial x_j}\right] + G_k C_{\varepsilon 1}\frac{\varepsilon}{k} + G_b C_{\varepsilon 1} C_{\varepsilon 3}\frac{\varepsilon}{k} - \rho\varepsilon\frac{\varepsilon}{k}C_{\varepsilon 2} + S_\varepsilon \tag{2.7}$$

In equations (2.5) to (2.7), C_μ, $C_{\varepsilon 1}$, $C_{\varepsilon 2}$, σ_k, and σ_ε are constants of the model. G_b and G_k are the production of turbulent kinetic energy because of buoyancy and velocity gradients in the flow. Y_m considers the effect of compressiblity on the production of k. Finally, S_k and S_ε are other source terms that may contribute towards the production or dissipation of k and ε. For instance, the injected droplets to the domain can intensify or dissipate turbulence, which will be discussed in the Discrete Phase section.

According to the standard k-ε model, the model constants, C_μ, $C_{\varepsilon 1}$, $C_{\varepsilon 2}$, σ_k, and σ_ε are 0.09, 1.44, 1.92, 1.0, and 1.3, respectively.

In addition to the standard k-ε model, other constants or modifications have been proposed. One of those modifications is the Realizable k-ε model which provides a different transport equation for turbulent dissipation rate. While the transport equation for the turbulent kinetic energy is similar to equation (2.6), the modified ε transport equation is shown in equation 2.8)

$$\frac{\partial}{\partial y}(\overline{\rho}\varepsilon) + \frac{\partial}{\partial x_j}(\overline{\rho}\varepsilon u_j) = \frac{\partial}{\partial x_j}\left[\left(\mu + \frac{\mu_t}{\sigma_\varepsilon}\right)\frac{\partial \varepsilon}{\partial x_j}\right] + \rho C_1 S\varepsilon + G_b C_{\varepsilon 1} C_{\varepsilon 3}\frac{\varepsilon}{k} - \rho\varepsilon\frac{\varepsilon}{k+\sqrt{\nu\varepsilon}}C_2 + S_\varepsilon \tag{2.8}$$

Two terms have been changed, and two additional parameters, C_1 and S, are defined as follows:

$$C_1 = \max\left[0.43, \frac{S\frac{k}{\varepsilon}}{S\frac{k}{\varepsilon}+5}\right] \tag{2.9a}$$

$$S = \sqrt{2S_{ij}S_{ij}} \tag{2.9b}$$

$$S_{ij} = \frac{1}{2}\left(\frac{\partial \widetilde{u_j}}{\partial x_i} + \frac{\partial \widetilde{u_i}}{\partial x_j}\right) \tag{2.9c}$$

Furthermore, the constants of the Realizable k-ε model,$C_{\varepsilon 1}$, C_2, σ_k, and σ_ε are 1.44, 1.9, 1.0, and 1.2, respectively.

2.2.2 Reynolds Stress Model (RSM)

In contrast to the k-ε model which models the Reynolds stresses by calculating the turbulent viscosity, the RSM solves the Reynolds stresses directly; the Reynolds stress tensor has nine components, but only six of these components need to be computed because of the symmetry in the Reynolds stress tensor; in addition, one transport equations is required to solve the dissipation rate ε (equation (2.7)), so there are seven transport equations to solve the closure problem in a three-dimensional turbulent flow.

In a two-dimensional turbulent flow, the number of Reynolds stresses decreases to four where transport equations are solved for $\widetilde{u''u''}$, $\widetilde{u''v''}$, $\widetilde{v''v''}$, and $\widetilde{w''w''}$ Reynolds stresses; in total, there are five transport equations for a two-dimensional turbulent flow. This model does not need the transport equation for turbulent kinetic energy k since this variable can be directly calculated from equation (2.10) as a function of Reynolds stresses.

$$k = \frac{1}{2}\widetilde{(u_j'')^2} = \frac{1}{2}\left[\widetilde{u''^2} + \widetilde{v''^2} + \widetilde{w''^2}\right] \tag{2.10}$$

2.3 Combustion

Similar to the Reynolds stresses, there are two terms in equation (2.4c) that are not known, so models are required to find the values of the turbulent scalar flux and mean source term in order to close the set of equations.

The turbulent scalar flux can be modeled by the gradient diffusion assumption. This assumption relates the turbulent scalar flux to the scalar mean value and the turbulent viscosity as shown in equation (2.11).

$$\widetilde{\phi_k'' u_j''} = -\nu_T \frac{\partial \widetilde{\phi}_k}{\partial x_j} \tag{2.11}$$

The turbulence viscosity is calculated according to the models described in section (2.2). However, modeling mean source term is a more challenging task. It can be explained according to the Arrhenius law. This law states that the rate of reaction for producing or consuming species grows exponentially with the local temperature. If the local temperature fluctuates, then the rate of reaction will change exponentially; therefore, it is not possible to use the local mean temperature in the Arrhenius law to obtain the mean source term, and it is of paramount importance to consider the effects of temperature fluctuations. This method is different from the approach used for the turbulent scalar flux.

Since the goal of this study is to simulate the spray combustion which is sorted as partially premixed flame, the models which are only related to this sort of combustion are discussed in this section. Still, there are different approaches used to solve the closure problem of the mean reaction source term such as eddy break up (EBU) model, eddy dissipation concept (EDC), PDF methods, flamelet methods, etc.

This study focuses on two methods: the steady flamelet and Flamelet Generated Manifold models. In these models, the turbulence and chemical processes are decoupled under certain assumptions, and detailed chemical reactions are solved in a laminar flow. Then, the results for different operating conditions are stored in lookup tables, and they will be used whenever the data for species or heat are needed. In what follows, the steady flamelet and flamelet generated manifold models are explained.

2.3.1 Steady Flamelet Model

The concept of flamelet is based on the assumption of really thin flame reaction zone, so the turbulent non-premixed flame can be seen as an ensemble of laminar diffusion flamelets (Peters 1984). There are different characteristical length scales that can be distinguished in the flame. While the integral length scale (l_t) and Kolmogorov (η_k) are two extremes of the turbulent length scales, two main lengths for the flame are defined as shown in figure (2.1). The first one is the diffusion layer thickness (l_d). This is the thickness that the oxidizer and the fuel diffuse and mix into each other. The second one is the reaction zone thickness (l_r), where the mixture of the fuel and oxidizer has the best mixing ratio to react and burn, so the reaction occurs (Poinsot & Veynante 2011).

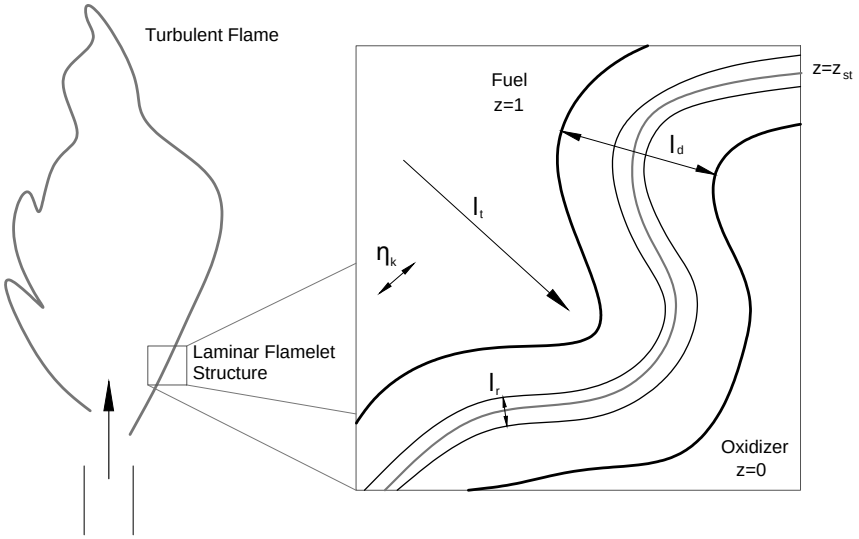

Figure 2.1: Non-premixed flame and its characteristic length scales (Poinsot & Veynante 2011)

According to the flamelet assumption that the minimum turbulent length scale, Kolmogorov length scale, is much larger than the reaction zone thickness. This means that in spite of the fact that the flame is wrinkled or corrugated by the turbulence, the thin flame front zone would not be affected by the turbulence and the its structure is the same as the laminar flame structure. In order to formulate this statement, the Damköhler number is used. It is defined as the ratio of the turbulence and chemical time scales (equation (2.12)). For very large Damköhler numbers, the flamelet assumption is correct.

$$Da = \frac{\text{flow time scale}}{\text{chemical time scale}} \tag{2.12}$$

What happens inside the diffusion zone can be simplified as figure (2.2), which shows the oxidizer and fuel mass fractions, and the temperature profiles as a function of the location on the axis orthogonal to the flame front. From the left side, as the fuel goes to this layer, its mass fraction decreases while the mass fraction of the oxidizer increases. However, The heat release happens only in the reaction zone. This is only a simplified example and it is possible to consider similar situations for reactions with more species rather than just an oxidizer and a fuel.

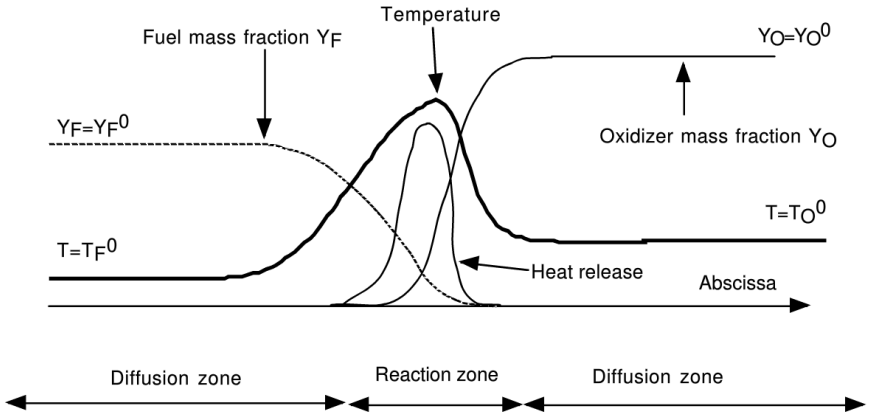

Figure 2.2: The oxidizer and fuel mass fractions as well as temperature profiles in a non-premixed diffusion zone (Poinsot & Veynante 2011)

The local flame structure inside the thin reaction zone is similar to the flame structure of a laminar counterflow shown in figure (2.3), which is known as the counterflow diffusion flamelet.

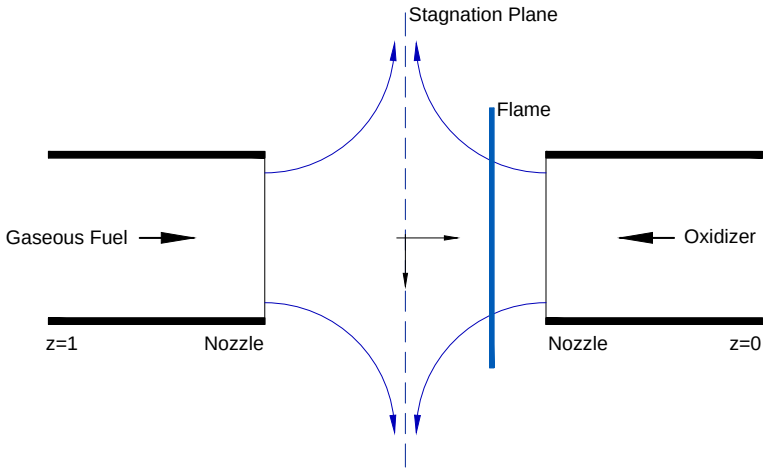

Figure 2.3: the steady counterflow diffusion flamelet configuration (de Goey et al. 2010)

Still, there is one problem with this configuration that the results are the function of physical space; therefore, the results cannot be used if the spacing between the oxidizer jet and the fuel jet changes. In order to solve the problem, the mixture fraction (Z) is defined as shown in equation (2.13), and by mapping from the physical space to the mixture fraction space, this problem would be solved. In the equation, the variable f represents the element mass fractions for any arbitrary element such as oxygen, hydrogen, or carbon. Moreover, the subscripts O and F represent the oxidizer and fuel initial element mass fractions, when they are not mixed.

$$Z = \frac{f_i - f_{i,O}}{f_{i,F} - f_{i,O}} \tag{2.13}$$

In order to derive the final flamelet equations in ANSYS Fluent, some assumptions are made as follows:

- The flame is non-premixed, so the fuel and oxidizer are not mixed in advance.
- All species diffusion coefficients are equal.
- The Lewis number, which is the ratio of thermal diffusivity to mass diffusivity, must be equal to one.

Based on these assumptions the flamelet equations for the species and temperature are derived through equations (2.14a) and (2.14b), respectively. This formulation is similar to the proposed flamelet equation by Peters (1984).

$$\rho \frac{\partial Y_k}{\partial t} = \frac{1}{2}\rho\chi\frac{\partial^2 Y_k}{\partial Z^2} + S_k \tag{2.14a}$$

$$\rho \frac{\partial T}{\partial t} = \frac{1}{2}\rho\chi\frac{\partial^2 T}{\partial Z^2} - \frac{1}{c_p}\sum_k H_k S_k + \frac{1}{2c_p}\left[\frac{\partial c_p}{\partial Z} + \sum_k c_p \frac{\partial Y_k}{\partial Z}\right]\frac{\partial T}{\partial Z} \tag{2.14b}$$

In these equations, Y_k and T are species mass fractions and temperature, for which the equations will be solved. Moreover, ρ, $c_{p,k}$, and c_p are the density, k^{th} species specific heat, and mixture-averaged specific heat, respectively. H_k and S_k are the species enthalpy and source term. The source term can be calculated according to the chemical mechanism and the Arrhenius law.

Still, there is a new parameter named the scalar dissipation rate, χ. In the physical space, as the jet velocities increase, the strain increases. In order to consider the strain rate in the mixture fraction space, the scalar dissipation rate is defined as equation (2.15), where D is the diffusion coefficient.

$$\chi = 2D|\nabla Z|^2 \tag{2.15}$$

When the combustion chemistry is relatively fast and no slow reacting species such NO_x are considered in the flame, it is possible to deploy the steady flamelet assumption. In this approach, the left hand sides of the equation set (2.14) are ignored, so only the right hand sides are solved. If there are N species which are used in the chemical mechanism, for a specified scalar dissipation rate, N+1 ordinary differential equations should be solved to obtain the species and temperature profiles. Therefore, ANSYS Fluent starts from small values of the scalar dissipation rate representing the equilibrium condition and increases the scalar dissipation rate until no feasible solution can be found for the set of equations, which means the flame has extinguished. The results are stored in two-dimensional tables for all the species and temperature, where independent variables are the mixture fraction and scalar dissipation rate. A sample of this table is shown in appendix (A.1)

The obtained results are the adiabatic steady flamelets; however, if radiative heat transfer or evaporation play roles, the table cannot be used without applying modification to the table. In order to simplify the problem, an assumption is made that the heat loss/gain does not affect the species mass fractions as long as the mixture fraction and scalar dissipation rate are constant. Thus, under this circumstance, the mixture-averaged specific heat does not change and by assigning the heat loss/gain, the temperature can be easily calculated from the adiabatic temperature.

Although the assumption of the steady flamelet is based on the thin reaction zone, it is necessary to include the effects of turbulence on the flame. Turbulence can wrinkle or stretch the flame; in addition, the intermittency in the flame position is another effect. All of these effects are included by turbulence-chemistry interaction modeling which is carried out through the probability density function (PDF) method.

According to the PDF concept, the mean value of any arbitrary variable (ϕ) such as species mass fractions or temperature can be calculated as shown in equation (2.16), where p in this equation is the joint PDF. In this definition, χ_{st} is the scalar dissipation rate at the point where the mixture reaches its stoichiometric ratio.

$$\widetilde{\phi} = \iint \phi\left(Z, \chi_{st}\right) p\left(Z, \chi_{st}\right) dZ d\chi_{st} \tag{2.16}$$

If the variables are assumed to be statistically independent, then the joint PDF can be split in two PDFs (equation (2.17)).

$$\widetilde{\phi} = \iint \phi\left(Z, \chi_{st}\right) p_Z\left(Z\right) p_\chi\left(\chi_{st}\right) dZ d\chi_{st} \tag{2.17}$$

The advantage of two independent variables is the possibility of presuming a PDF shape for each of the variables. In ANSYS Fluent, the presumed PDF shape for the mixture fraction is a β function which includes the effects of fluctuations in the mixture fraction; however, for χ_{st}, the fluctuations are ignored, so a Dirac delta function is presumed as its PDF function. The β function is defined in equation (2.18) with the definition of its powers α and β. Therefore, if the mean mixture fraction ($\widetilde{Z}$) and its variance ($\widetilde{Z''^2}$) are known, the presumed β PDF function can be calculated.

$$p(Z) = \frac{Z^{\alpha-1}(1-Z)^{\beta-1}}{\int_0^1 Z^{\alpha-1}(1-Z)^{\beta-1}dZ} \tag{2.18a}$$

$$\alpha = \left[\frac{\widetilde{Z}(1-\widetilde{Z})}{\widetilde{Z''^2}} - 1\right]\widetilde{Z} \tag{2.18b}$$

$$\beta = \left[\frac{\widetilde{Z}(1-\widetilde{Z})}{\widetilde{Z''^2}} - 1\right](1-\widetilde{Z}) \tag{2.18c}$$

The Dirac delta function as well as the mean stoichiometric scalar dissipation rate are shown in equation (2.19), where C_χ is a constant with the value of 2. Moreover, the variables ε and k are the turbulent dissipation rate and turbulent kinetic energy. First, they should be solved from the turbulence models; then, the mean stoichiometric scalar dissipation rate can be determined.

$$p_\chi(\chi_{st}) = \delta(\chi_{st} - \widetilde{\chi_{st}}) \tag{2.19a}$$

$$\widetilde{\chi_{st}} = C_\chi \frac{\varepsilon}{k}\widetilde{Z''^2} \tag{2.19b}$$

Finally, after generating the flamelet table with two independent variables χ and Z, the interaction of turbulence with chemistry is included. This interaction increases the number of independent variables to three, namely: the mean mixture fraction ($\widetilde{Z}$), the mixture fraction variance ($\widetilde{Z''^2}$), and the mean stoichiometric scalar dissipation rate ($\widetilde{\chi_{st}}$). Because of reducing the prohibitive computational cost, instead of solving equation (2.17) during the CFD simulation, this integration is done for different values of $\widetilde{Z}$, $\widetilde{Z''^2}$, and $\widetilde{\chi_{st}}$; then, the results of species fractions and temperatures are stored in a three-dimensional lookup table.

Whereas this three-dimensional lookup table is specified for adiabatic flames, it is also possible to use it for non-adiabatic flames. According to the assumption mentioned above that the heat loss/gain does not affect the species mass fractions, only one additional independent variable, mean enthalpy, can describe the effects of heat loss/gain.

To conclude, figure (2.4) shows how the steady flamelet model works in conjunction with the PDF concept. The starting point is from the given mean values of the flow field, which provide $\widetilde{Z}$ and $\widetilde{Z''^2}$ from two transport equations; this completely defines the presumed β PDF shape. From the turbulence model parameters, k and ε, the stoichiometric scalar dissipation can be determined (equation (2.19)). Finally, from the lookup table allocated to these independent variables, the species mass fractions and temperature can be determined. Accordingly, the mean density is calculated, so it can be used in the RANS equations, and the loop proceeds.

2.3.2 Flamelet Generated Manifold

The main drawback of the steady flamelet model is the "mixed is burnt" assumption; therefore, it cannot predict the flame quenching or ignition. Flamelet Generated Manifold (FGM) model is used to solve this problem. The procedure is very similar to the steady flamelet model with some differences.

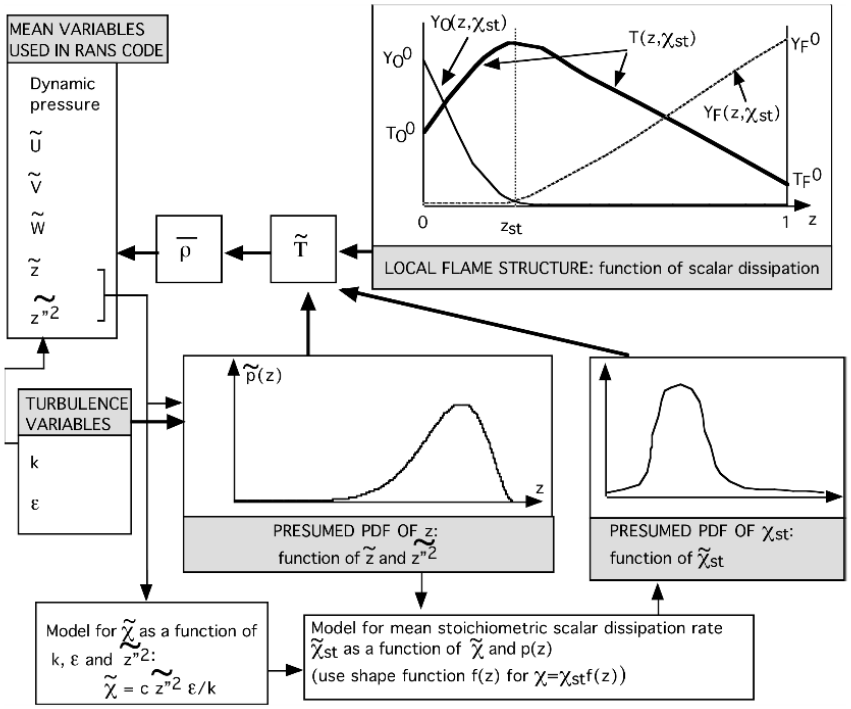

Figure 2.4: The flowchart of PDF-flamelet solution approach (Poinsot & Veynante 2011)

The first difference is in the definition of the flamelet table. Steady flamelet only considers the flamelets between the equilibrium scalar dissipation rate ($\chi = 0$) and the maximum scalar dissipation rate ($\chi_{extinction}$), when the flame extinguishes. However, in the FGM model, after the flame extinguishes for the steady flamelet equations (equation (2.14) without the temporal terms) , unsteady flamelet equations (equation (2.14) are solved for the maximum scalar dissipation rate ($\chi_{extinction}$) until reaching the mixing line. Figure (2.5) shows the steady flamelets with the blue color and different scalar dissipatin rates while the unsteady flamelets are shown in red with a constant scalar dissipation rate ($\chi_{extinction}$).

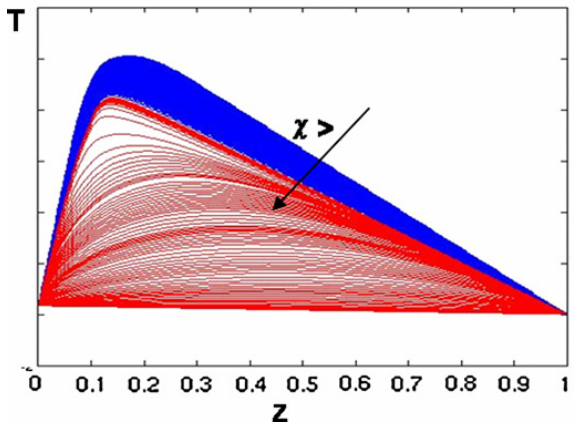

Figure 2.5: Temperature profiles for steady flamelets with different scalar dissipation rate (blue) and unsteady flamelets with the maximum value of scalar dissipation rate(red) (Chrigui et al. 2012)

To join the steady and unsteady flamelets, a new parameter is defined as the progress variable (c). For a combination of some species that their mixture fractions increase monotonically through the flame, the progress variable is defined as equation (2.20). $Y_{k,equilibrium}$ and $Y_{k,mixing}$ are two extremes of the range between the mixing line (the bottom flamelet in figure (2.5)) and the equilibrium line (the top flamelet in figure (2.5)) for a mixture fraction. Accordingly, there is no further need to use the scalar dissipation rate and the progress variable can act similarly to the scalar dissipation but in the range of 0 (no combustion, i.e. mixing line) and 1 (complete combustion, i.e. equilibrium line). Similar to the steady flamelet model, a sample of the table generated by the FGM model is shown in appendix (A.2)

$$c = \frac{Y_{k,equilibrium} - Y_k}{Y_{k,equilibrium} - Y_{k,mixing}} \tag{2.20}$$

The second main difference is in the PDF integration. While the fluctuations in the scalar dissipation rate were ignored in the steady flamelet, a β PDF shape is deployed to consider the fluctuations in the progress variable. Therefore, in addition to the mean mixture fraction and mixture fraction variance transport equations, two transport equations are required to calculate the mean progress variable ($\widetilde{c}$) and progress variable variance ($\widetilde{c''^2}$); thus, the mean value of species mass fractions and temperature are computed from equation (2.21) under the assumption of independent PDFs.

$$\widetilde{\phi} = \iint \phi\left(Z,c\right) p_Z\left(Z\right) p_c\left(c\right) dZdc \tag{2.21}$$

Similar to the steady flamelet model, the heat loss/gain can only affect the temperature, so there is no need to include the effects of heat loss/gain fluctuations in PDF calculations. Therefore, the final lookup table, which uses the flamelet generated manifold model with the PDF concept, has five dimensions: the mean mixture fraction ($\widetilde{Z}$), mixture fraction variance ($\widetilde{Z''^2}$), mean progress variable ($\widetilde{c}$), progress variable variance ($\widetilde{c''^2}$), and mean enthalpy ($\widetilde{H}$).

Finally, although the integration of equation (2.21) takes relatively long time and the resultant lookup table uses large space on the data storage device, it can reduce prohibitive computational time during the CFD calculations; hence, this is a robust approach to simulate the turbulent reacting flows.

2.4 Discrete Phase

In spray combustion, there is a liquid phase in the domain in addition to the gas phase. This phase has to be considered since in reality the interaction of the gas and liquid phases affects the combustion and its profile. The liquid phase provides the required fuel for combustion as well as the required momentum to accelerate the gas phase. Hence, it is highly important to consider as much significant relevant phenomena as possible during turbulent spray combustion. There are five main phenomena that play role from the first stages of injection to the complete combustion: atomization, dispersion, evaporation, micro-mixing, and combustion.

Firstly, the process starts with the injection of liquid fuel into the gas phase. At the interface of the phases, because of the difference in velocities, the instability develops which results in formation of ligaments and atomization; this part will be discussed later. After atomization, droplets with high momentum supply kinetic energy to the gas phase which accelerate the gas phase while the droplets decelerate. Moreover, because of the gradient in velocities, turbulence is present in both of the phases and changes the characteristics of the gas and liquid flows.

The concentration gradient at the droplet interface makes the liquid fuel evaporate and this process makes a fuel gas film near each droplet. Turbulence works as a mixer and it homogenizes the gas phase in the vicinity of droplets, so evaporation rate increases as turbulence intensifies.

If evaporation provides enough fuel in the gas phase and turbulence mixes well the fuel and oxidizer, combustion will sustain. Since combustion releases huge amount of heat, combustion provides enough energy to increase evaporation rate and gas-phase momentum. Thus, the whole procedure of interaction between these five phenomena are completely coupled and if any of these phenomena changes, the whole system will change.

In order to model the whole system of combustion, there are two main approaches: Euler-Euler and Euler-Lagrange. The former approach considers both the gas and liquid phases as a continuum, so for both of these phases, Navier-Stokes equations would be solved. On the other hand, Euler-Lagrange approach treats the gas phase as a continuum while the liquid phase is treated as a large number of particles which is described by Lagrangian flow motion.

Because of the little volume fraction of the liquid phase (dispersed phase), Euler-Lagrange approach is deployed for modeling the discrete phase. In what follows, the governing equations for describing atomization, dispersion, and evaporation are explained while the turbulence and combustion models were discussed in previous sections.

2.4.1 Atomization

After the liquid fuel injection, the fuel is dispersed in the gas phase until all the fuel is evaporated. In figure (2.6), the whole domain is divided in three regions: dense, dilute, and very dilute regime. This classification is based on the influence of dispersed phase on the gas phase as well as the probability of collision of droplets. In the very dilute regime which can be distinguished through very low volume fraction of the dispersed phase (less than 10^{-6}), droplets have little effect on the gas phase and the probability of droplet collision is very low. At the other extreme where the dispersed phase volume fraction is above 10^{-3} the effects of liquid phase on the gas phase and the collision of droplets are not negligible and this region is the main focus of studying of atomization. Eventually, dilute regime is the middle stage, in which the volume fraction is so small that it can be assumed that there is no collision between droplets; still, the dispersed phase affects the behavior of the continuous phase.

The atomization and collision of droplets happen mainly in the dense regime. Because of the dense dispersion of droplets, random collision of two or more droplets may happen and they merge into a droplet after collision, which is known as coalescence. As shown in figure (2.6), there are two stages of atomization: primary and secondary. Primary injection happens when the Kelvin-Helmholtz instability develops, so large droplets as well as ligaments form. When these ligaments or large droplets disintegrate further, secondary atomization happens.

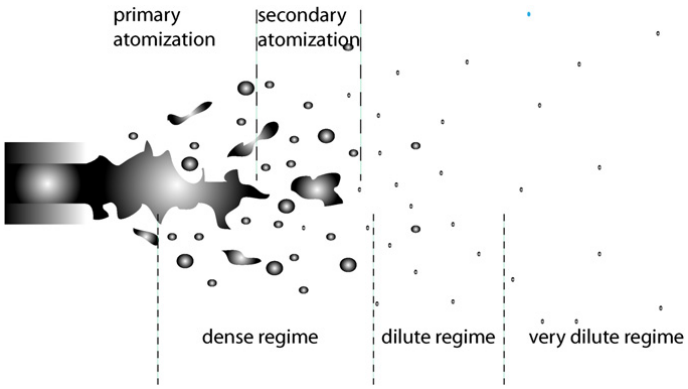

Figure 2.6: The interaction of the gas and liquid phases in an injector in different regimes (Jenny et al. 2012)

2.4.1.1 Primary Atomization

Depending on the type of spray nozzle, the required model as well as the parameters for describing the atomization is different. ANSYS Fluent offers some models for different atomizers. In the experimental setup, the pressure-swirl atomizer was used to spray the liquid fuel. Therefore, Linearized Instability Sheet Atomization (LISA) model has been chosen to model this type of nozzle. LISA model works based on two stages: film formation and sheet breakup. The whole procedure is explained in detail in ANSYS Fluent Theory Guide (ANSYS 2013), so these two stages are explained briefly here.

LISA model requires five parameters of the injector in ANSYS Fluent: injection pressure (p), temperature (T), half angle (θ), dispersion angle (β), and injector diameter (d). Pressure of the reservoir is needed to calculate the injection velocity. Temperature is needed to calculate the thermodynamic properties of the liquid phase which is only a function of temperature rather than pressure. Half angle, dispersion angle, and injector exit diameter are the geometric parameters of the injector. These parameters are specified in figure (2.7).

When the flow exits the atomizer, firstly film formation occurs before the development of droplets. The main equation in this stage is the mass balance as shown in equation (2.22). In this equation, ρ is density of the liquid phase, u is the axial component of velocity, U is the velocity magnitude, t is the film thickness, and d_0 is the most probable initial droplet diameter. As mentioned above, the velocity and its axial component are functions of the pressure and half angle; equations (2.23) and (2.24) show the correlation between these parameters.

$$\dot{m} = \pi \rho_l u t \left(d - t\right) \tag{2.22}$$

$$u = U\cos(\theta) \tag{2.23}$$

$$U = k_v \sqrt{\frac{2\Delta p}{\rho_l}} \tag{2.24}$$

where for an injected mass (m) the velocity coefficient (k_v) is:

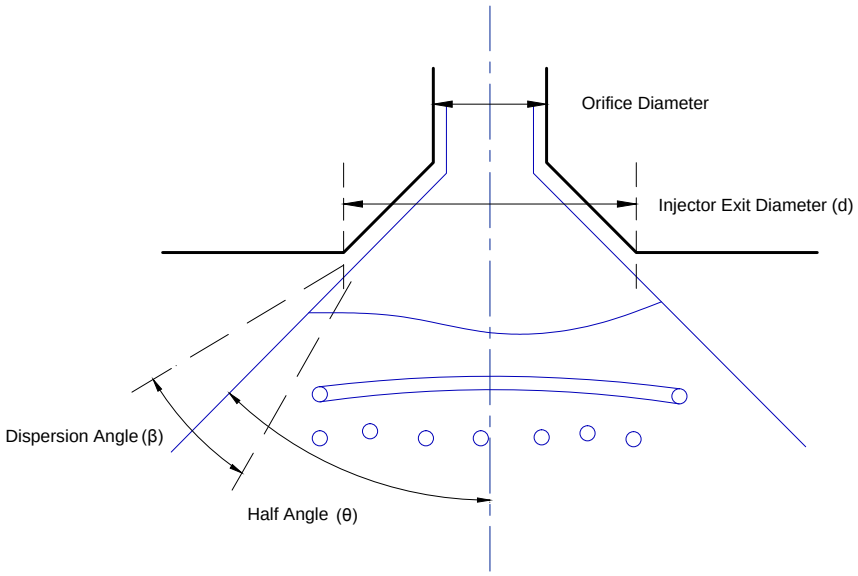

Figure 2.7: Schematic view of atomization in a pressure-swirl atomizer (ANSYS 2013)

$$k_v = \max\left(0.7, \frac{4m}{d_0^2 \rho_l \cos(\theta)} \sqrt{\frac{\rho_l}{2\Delta p}}\right) \tag{2.25}$$

After film formation, sheet breakup and atomization occur, where droplets are created. Because of the long derivation based on linear instability analysis of a two-dimensional and viscous liquid sheet in a gas phase, the derivation is not given here. Still, there are two parameters that are present in the derivation of the sheet breakup model: sheet constant and ligament constant. The first one shown in equation (2.26) is the logarithmic ratio of the critical amplitude (η_b) to the initial amplitude (η_0) of the liquid film. The value of sheet constant is obtained analytically to be 12. Dombrowski & Hooper (1962) show that this analytical result accurately matches the experiments for Weber numbers (defined as equation (2.27)) between 2 and 200, but it can still be used out of this range. Moreover, Ligament constant is assumed to be 0.5; this is the value that relates the ligament diameter and the corresponding breakup wavelength.

$$\text{Sheet constant} = \ln\left(\frac{\eta_b}{\eta_0}\right) \tag{2.26}$$

$$We = \frac{\rho_l |\vec{u_p} - \vec{u}|^2 d_p}{\sigma} \tag{2.27}$$

where $|\vec{u_p} - \vec{u}|$, d_p, and σ are the droplet relative velocity to the gas phase, droplet diameter, and droplet surface tension. The gas Weber number is defined similarly, but instead of the liquid density, the density of gas phase is applied. Lastly, an assumption was made during the derivation, that requires the gas Weber number to be more than 27/16 to accurately predict the primary atomization.

2.4.1.2 Secondary Atomization

For the secondary atomization, ANSYS Fluent provides four different models which can be used under different situations mainly controlled by the Weber number of the flow. These four models are: Taylor Analogy Breakup (TAB), Wave Breakup, Kelvin-Helmholtz/Rayleigh-Taylor (KHRT) breakup, and Stochastic Secondary Droplet (SST) models.

Since this study deals mainly with steady injection in ANSYS Fluent (as explained in section (2.4.4)), it is not possible to use secondary atomization models. However, in order to compare the results and verify if it is crucial to consider secondary breakup through using unsteady injection, Taylor Analogy Breakup will be employed, which is suitable for low Weber numbers.

Taylor Analogy Breakup (TAB) is based on the Taylor's analogy describing the oscillation and distortion of droplets similar to a spring-mass system. Therefore, this model consists of restoring, damping, and external forces similar to a spring-mass system, which are surface tension, viscosity, and drag force of the droplet, respectively. A critical value which provides the limit for the breakup of the droplet can be defined. When this critical value is surpassed, the large droplet split into smaller droplets.

2.4.2 Governing Equations of Particles

Since the initial contact between the liquid phase and the gas phase, mass, momentum, and energy exchange occurs at the interface. In this section, the focus is only on the modeling of different aspects of particle motion. The interaction between particles and the gas phase is the aim of next section, where the transferred mass, momentum, and energy from the particles affect the gas phase, and vice versa.

2.4.2.1 Particle motion

The equation describing the motion of a particle in a Lagrangian frame is only a function of time, so the sum of all forces acting on the particle makes it accelerate or decelerate. This ordinary differential equation (ODE) which must be integrated over time is shown in equation (2.28) and it is known as the trajectory equation (ANSYS 2013).

$$\frac{d\vec{u}_p}{dt} = \vec{F}_D + \frac{\vec{g}(\rho_p - \rho)}{\rho_p} + \vec{F} \tag{2.28}$$

On the right hand side, the terms are corresponding to the drag force, buoyancy (difference between the droplet density ρ_p and the gas-phase density ρ), and sum of all other forces that may act on the particle. The drag force in this equation is calculated according to equation (2.29), where μ and ρ are gas-phase viscosity and density.

$$F_D = \frac{18\mu}{\rho d_p^2} \frac{C_D Re}{24} \tag{2.29}$$

where

$$Re = \frac{\rho_p d_p |\vec{u}_p - \vec{u}|}{\mu} \tag{2.30}$$

The only unknown parameter in this set of equations is the drag coefficient C_D. There are different models to calculate the drag coefficient according to the shape, size, or velocity of the droplet. In this study two of these models are used: spherical drag law and dynamic drag model. The former is a simple algebraic equation shown in equation (2.31). The coefficients a_1, a_2, and a_3 are three parameters which are functions of the Reynolds number.

$$C_D = a_1 + \frac{a_2}{Re} + \frac{a_3}{Re^2} \tag{2.31}$$

On the other hand, the dynamic drag model is a complicated model that is able to consider distortion in the shape of a droplet. As mentioned in secondary atomization, the large droplets can be distorted and even split into smaller droplets; therefore, the drag force for this case is different from a spherical droplet, especially if the Weber number is large. This model calculates the drag coefficient by multiplying the spherical drag coefficient shown in equation (2.32) by a correction factor which is obtained from solving a second-order ODE.

$$C_{d,sphere} = \begin{cases} 0.424 & Re < 1000 \\ \frac{24}{Re}\left(1 + \frac{1}{6}Re^{2/3}\right) & Re \geq 1000 \end{cases} \tag{2.32}$$

It should be pointed out that the dynamic drag model is only available for unsteady injection (discussed in section 2.4.4) where secondary atomization can be activated and as a result distortion occurs. For steady injection, which is the foucs of this study, spherical drag law is employed.

2.4.2.2 Turbulent dispersion

In addition to the velocity field of the gas phase which affects the drag force acting on droplets, the turbulence which is present in the gas phase has substantial impact on the droplet path. This can be done by considering the effects of turbulence on the gas-phase velocity. This means that instead of the mean velocity, instantaneous velocity (sum of mean and fluctuating velocities) is applied to the trajectory equation (equation (2.28)). ANSYS Fluent uses the Discrete Random Walk (DRW) model to obtain the instantaneous velocities. The procedure is to find the fluctuating velocities and use them in equation (2.28) for a specific time span; then, the fluctuating velocities are calculated again and this goes on. In this procedure there are two unknown parts. First of all, the fluctuating velocities are not available; furthermore, the time span have to be defined according to the eddy characteristics.

In general, fluctuating velocities are computed based on the local RMS values of velocity components (equation 2.33). The coefficient ζ is a random number which has a Gaussian distributed value. In the Reynolds Stress model the value of fluctuating velocities may be different while in k-ε model, all the RMS velocity components are equal to $\sqrt{2k/3}$ which is the same for all directions.

$$u'' = \zeta \sqrt{\widetilde{u''^2}} \tag{2.33a}$$

$$v'' = \zeta \sqrt{\widetilde{v''^2}} \tag{2.33b}$$

$$w'' = \zeta \sqrt{\widetilde{w''^2}} \tag{2.33c}$$

In these equations, the value of ζ is constant in each time span while from one to another time span, it changes to take into account the stochastic behavior of turbulence. These time spans are defined according to two characteristic timescales. The first timescale is the time that a particle needs to cross an eddy, that is mainly controlled by the particle characteristics such as its relaxation time and relative velocity. The second timescale is characteristic lifetime of the eddy (τ_e) through which the droplet passes. One correlation that is deployed in ANSYS Fluent is shown in equation 2.34). T_L, k, and ε are Lagrangian integral timescale, turbulent kinetic energy, and turbulent dissipation rate, respectively. The coefficient C_L is a parameter that can be assumed to be 0.15 for k-ε model and 0.30 for the Reynolds Stress model.

$$\tau_e = 2T_L = 2\left(C_L \frac{k}{\varepsilon}\right) \tag{2.34}$$

After calculating these two periods of time, the minimum of them is selected to be used as the period when the parameter ζ and, as a result, the fluctuating velocities are constant while the particle advances.

In steady injection where each particle is tracked over the domain with its instantaneous velocity field, the calculation must be done for a number of particles to consider the stochastic behavior of turbulence; therefore, the number of tries is the number of particles that pass through random fluctuating velocity fields. Although it can improve the accuracy as well as includes the randomness behavior of turbulence, it causes the calculations expensive, so it is suggested to limit number of tries between 3 and 5 (Rochaya 2007).

Nonetheless, unsteady injection does not need to be solved a few times since the trajectory equation (equation (2.28)) is solved over a virtual time while the gas phase is solved.

2.4.2.3 Mass and Heat transfer

In ANSYS Fluent different types of particles are available in order to define how the discrete and gas phases exchange heat and mass. Because of the evaporation in the droplets from injection until complete evaporation, “Droplet” is chosen as the particle type. It consists of different laws to model the mass and heat transfer under different circumstances. These laws are: heating/cooling, evaporation, and boiling. These laws are only applicable under specific conditions. In what follows, these laws are explained briefly, and their range of application are presented. It should be pointed out that the liquid is assumed to be non-volatile such as pure ethanol.

Heating or Cooling

Heating and cooling can occur without any mass transfer from the droplet. This sort of heat transfer without any mass transfer is known in ANSYS Fluent as inert heating/cooling. A temperature known as evaporation temperature is defined to express the limit for heat transfer without mass transfer. For instance, the default value of evaporation temperature set by ANSYS Fluent is 271 (K). Below this temperature, heat transfer occurs through convection at the interface between the gas and liquid phases, and radiation between the droplet surface and the surrounding ambiance.

Evaporation

When temperature is above the evaporation temperature, but still below the boiling temperature of the liquid at the atmospheric pressure, evaporation occurs. In contrast to previous law, the mass can be transferred from the droplet interface with the rate shown in equation (2.35) according to Fick's law.

$$N_i = k_c\left(C_{i,s} - C_{i,\infty}\right) \tag{2.35}$$

where, N_i, k_c, and C are the molar flux of vapor, mass transfer coefficient, and vapor concentration; the mass transfer coefficient is calculated according to the Sherwood number, which is correlated with the Reynolds and Schmidt numbers. Therefore, the change in mass of the droplet with molar mass of $M_{w,i}$ and surface of A_p over an infinitesimal timestep dt is given in equation (2.36).

$$\frac{dm_p}{dt} = -N_i A_p M_{w,i} \tag{2.36}$$

According to this rate of evaporation, the energy balance for the droplet is shown in equation (2.37). The left hand side term describes the change in the energy content of the droplet where m_p, c_p, and T_p present the droplet mass, heat capacity, and temperature, respectively. On the right hand side of the equation, the first term refers to the convection between the droplet surface with the temperature (T_p) and the gas phase temperature (T_∞). The second term is the heat transfer as a result of the mass transfer with its corresponding latent heat (h_{fg}). The last term includes the effect of radiation with the surrounding (θ_R) if the droplet emissivity is ε_p.

$$m_p c_p \frac{dT_p}{dt} = hA_p\left(T_\infty - T_p\right) - \frac{dm_p}{dt} h_{fg} + A_p \varepsilon_p \sigma\left(\theta_R^4 - T_p^4\right) \tag{2.37}$$

If no mass transfer occurs, this equation will show the heat transfer of the first law, inert heating/cooling. Moreover, This heat and mass transfer model or evaporation model is known as infinite conductivity model. According to the model, there is no temperature gradient inside the droplet, but the temperature can change through time.

This formulation for the heat and mass transfer is rudimentary, and this can cause inaccuracy in the numerical simulation. When the evaporation rate is really high that causes temperature gradient inside the droplet or when the droplet internal recirculation cannot be ignored, more complex models are needed to accurately predict the evaporation.

Boiling

When the temperature of the droplet is equal to or above the boiling temperature, the droplet starts to boil. The boiling rate is given in equation (2.38). This applies to a case without radiation. In the equation, $c_{p,\infty}$ and k_∞ are the heat capacity and thermal conductivity of the gas; $\rho_p$and Re_d are the droplet density and Reynolds number (equation (2.30)).

$$\frac{d\left(d_p\right)}{dt} = \frac{4k_\infty}{\rho_p c_{p,\infty} d_p}\left(1+0.23\sqrt{Re_d}\right)\ln\left[1+\frac{c_{p,\infty}\left(T_\infty - T_p\right)}{h_{fg}}\right] \tag{2.38}$$

The heat transfer is exactly the same as equation (2.37), but since there is no temperature variation during boiling, the left hand side would be zero. Therefore, the combination of this equation and equation (2.38) gives the heat and mass transfer.

2.4.3 Coupling Discrete and Gas Phases

The interaction of the gas and liquid phases is taking into account through the exchanged mass, momentum, and heat between the phases. They are imposed to the gas phase as source terms in the governing equations. However, it is possible that the calculated values are so large that make the solution unstable, or cause solution divergence. Therefore, the source terms are mediated via multiplying by an under-relaxation factor. Choosing a value for under-relaxation factor is a trade off between the stability of the solution and the computational cost; if small values are chosen, the number of iterations to obtain converged results increases. If M, F, and Q represent the exchanged mass, momentum, and heat respectively, the source terms are updated with under-relaxation factor α according to equation (2.39) (ANSYS 2013).

$$M_{new} = M_{old} + \alpha\left(M_{calculated} - M_{old}\right) \tag{2.39a}$$
$$F_{new} = F_{old} + \alpha\left(F_{calculated} - F_{old}\right) \tag{2.39b}$$
$$Q_{new} = Q_{old} + \alpha\left(Q_{calculated} - Q_{old}\right) \tag{2.39c}$$

The procedure of how to solve a two-phase flow is shown in figure (2.8) and is described by the following three steps:

1. The discrete phase equations are solved based on the current gas-phase flow field.
2. The source terms of the discrete phase in the gas phase are updated according to the discrete phase results and the under-relaxation factor as shown in equation (2.39).
3. The gas phase is solved until the solution is converged for the gas phase based on the applied source terms from the discrete phase

The first step shows the one-way coupling between the gas and liquid phases, when the gas phase only affects the liquid phase. When both the gas phase and liquid phase affect each other, it is named a two-way coupling. The procedure mentioned above and shown in figure (2.8) is the procedure to make two-way coupling between the phases, and it is important to reach the equilibrium between two phases.

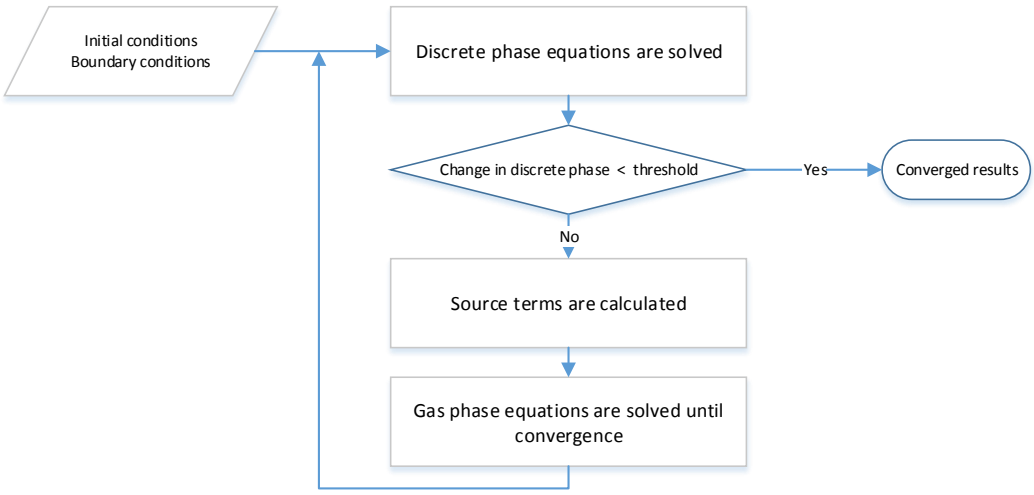

Figure 2.8: Simulation procedure of coupling the gas and liquid phases

It is also important to mention that in ANSYS Fluent, there are different levels of two way coupling. In general, if the iterative procedure is done as shown in figure (2.8), two-way coupling is achieved for mass, momentum, energy equations; however, the turbulence variables need to be coupled between two phases. When a droplet enters an eddy, it is possible that the droplet intensifies or damps the turbulence kinetic energy of the eddy, so it affects both the turbulent kinetic energy (k) and turbulent dissipation rate (ε) as an additional source term shown in equations (2.6) and (2.7). ANSYS Fluent offers an option named "Turbulence Two-way Coupling" to couple the turbulence variables in each discrete phase iteration. Although this option is available for the k-ε model, it cannot be used for the Reynolds stress model.

It is important to mention that in some situations, this option can make a groove in the domain where the turbulent dissipation rate approaches zero, and as a result, some problems such as high turbulence viscosity as well as large ε residual may occur. This means that the solution has not converged yet. Thus, despite of its importance to correctly model the turbulence, it is important to consider its problems when using it for the k-ε model. Since this option causes some problems and the turbulence models should be compared under similar situations, this option will not be used during the model validation.

2.4.4 Discrete-phase solution

Before explaining how the discrete phase is solved in ANSYS Fluent, there is a definition which is important to point out. In reality the number of droplets ejected from the injection can easily reach millions; this number is so large that it is computationally expensive if all of these droplets are tracked in the domain. Therefore, the concept of parcel is introduced to simplify the discrete phase calculations. A parcel is assumed to be a group of droplets with the same physical properties as well as velocities. As the number of parcels increases, the behavior of droplets can be predicted more accurately because each parcel lumps a smaller group of droplets; however, this costs more computational time, so a trade off between the number of parcels and the computational time have to be reached.

ANSYS Fluent offers two methods for solving the discrete phase: Steady injection and unsteady injection. Each one has their own pros and cons, but the main focus will be on steady injection.

In the steady injection, according to the last gas-phase velocity and turbulence profiles, injection takes place. It means that liquid parcels are released from the point defined as the injector, and they are tracked until they all evaporate, escape from the computational domain, or in case they cannot finish the path within a number of tracking steps. After this DPM iteration, the gas phase equations are solved for a number of iterations based on the renewed DPM source terms. Again a new injection takes place and the loop continues, this loop is repeated similarly as shown in figure (2.8) until the results in the gas phase and discrete phase do not change within a threshold.

On the other hand, unsteady injection proceeds in virtual timesteps. Although steady-state gas-phase solver may be applied, droplet injection is split over the virtual time. The procedure to solve the gas phase is exactly the same as shown in figure (2.8); nonetheless, proceeding in time does not occur in one DPM iteration, but each DPM iteration happens in a new timestep. The solution is converged when the discrete phase reaches an equilibrium; for instance, the number of evaporated droplets equals the number of injected droplets.

An advantage of the unsteady injection is its ability to simulate the dense region more accurately which is not the case for the steady injection. However, because of proceeding in the virtual time, it takes more time to achieve convergence. Therefore, if secondary breakup as well as coalescence are not the main concern, steady injection could be a better choice.

2.4.5 Postprocessing

There are two types of results provided by ANSYS Fluent. The first set of data is the effects of the discrete phase on the gas phase or its results in the domain such as evaporation rate, which is similar to other gas-phase results postprocessing; therefore, no additional processing is necessary. On the other hand, it is possible to gather the information of droplets passing through a specific cross section in the domain, which is known as Sample. The results of sample is a number of parcels with their properties such as location, velocities, diameter, number of droplets etc. These results cannot be deployed for comparison with experiments, directly. Hence, they need to be processed.

All of the sampled parcels can be classified in two ways: their diameter and their radial location at a specific height above the injector. If for each cross section the parcels are classified into 20 groups between the minimum and maximum radial position, and 8 different diameters between below 10 μm and above 70 μm, there will be 160 classes in which all the parcels can be arranged. Then, for each of these groups the axial velocity can be calculated as equation (2.40); likewise, the radial velocity is calculated. N is the number of parcels classified in each group while n_i is the number of droplets in each parcel; u_i, v_i, and w_i are the corresponding velocity components.

$$\bar{u} = \frac{\sum_{i=1}^{N} \left(\frac{u_i n_i}{\sqrt{u_i^2 + v_i^2 + w_i^2}} \right)}{\sum_{i=1}^{N} \left(\frac{n_i}{\sqrt{u_i^2 + v_i^2 + w_i^2}} \right)} \tag{2.40}$$

This averaging method is used to guarantee the same averaging method with experimental data. In experiment, the velocities are weighed with the time which each droplet needs to pass the probe volume with the length scale (L). Since the probe volume is constant, the measured time is proportional to the reciprocal of the droplet velocity magnitude. Nonetheless, ANSYS Fluent only provides the velocity components of the droplets passing a cross section; hence, using the reciprocal of velocity magnitude is the only choice that can generate comparable numerical results with the experimental results.

Moreover, another parameter is needed to represent the size of the droplets at a location in the domain. Sauter mean Diameter (SMD) is defined as the ratio of volume diameter (d_v) and surface diameter (d_s) shown in equation (2.41). On the contrary to previous definition of N, in this equation, N corresponds to the number of all parcels sampled at a specified location from the smallest to the largest droplet sizes. Therefore, there is only one SMD for each location.

$$SMD = \frac{d_v^3}{d_s^2} = \frac{\sum_{i=1}^{N} d_{s,p,i}^3 n_i}{\sum_{i=1}^{N} d_{s,p,i}^2 n_i} = \frac{\sum_{i=1}^{N} \left(\frac{6V_{p,i}}{\pi}\right) n_i}{\sum_{i=1}^{N} \left(\frac{A_{p,i}}{\pi}\right) n_i} = \frac{\sum_{i=1}^{N} 6V_{p,i} n_i}{\sum_{i=1}^{N} A_{p,i} n_i} \tag{2.41}$$

Chapter 3

Results and Discussion

In this chapter, the turbulence and combustion models are validated for two different cases by using similar spray models. The first case is the combustion of ethanol in a hot-diluted coflow while the second case uses the fresh air at the ambient temperature as the coflow. Since the main purpose of this project is to study the spray flameless combustion in furnaces, the main focus will be on the hot-diluted coflow, which simulates the behavior of the flameless combustion. The cold coflow case is presented here as a reference case to study the performance of spray combustion under a different coflow condition.

The chapter is divided into four main sections; in the first section, the settings required for each model are explained for both hot-diluted and cold coflows. Then, the performance of models are analyzed based on the comparison between the experimental data and the predicted results. The third section deals with the effects of different parameters that may or may not cause any difference in the final result. Finally, the turbulence and combustion models are validated for the second case in which the oxidizer is the cold coflow. According to these two cases, it is possible to draw conclusions on the performance of different turbulence and combustion models, especially the models set in ANSYS Fluent.

3.1 Configuration

The goal of this section is to assign the parameters of the models. The first priority is to set them based on the experimental setup; however, if no information is available, the parameters which result in the best data fitted on the experimental results will be used. This section starts with postprocessing the data from the experiment; then, it proceeds with model configurations for both the hot-diluted and cold coflow cases.

3.1.1 Postprocessing the Experimental Data

Through explaining the experimental setup in section (1.2), the injection angle was introduced to be 60°, and the injector diameter, that is different from the orifice diameter, was not discussed.

Due to the lack of information, the only choice is to find the diameter from the high-speed visualization images from the liquid sheet breakup shown in figure (3.1) for two different injections at similar sequence of exposure times. For both images, the field-of-view is 6.81 mm $\times$ 3.04 mm (Correia Rodrigues et al. 2014). Therefore, it can be deduced that the injection diameter is in the range of 1 mm to 2 mm. Since there is no further information, the value of 1.5 was chosen as the injector diameter (d). It should be mentioned that although any changes in this value can affect the final result, this is an error caused by the lack of information and it may be unavoidable. Still, this error does not have dire consequences on the final result if it only changes between 1 mm and 2 mm.

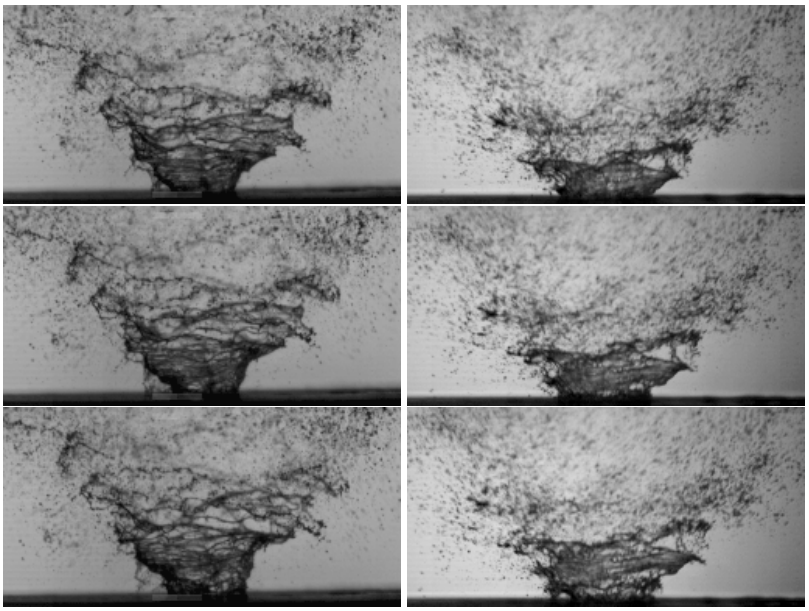

Figure 3.1: The liquid sheet breakup sequence of images for the cold coflow (Left) and hot-diluted coflow (Right) cases at 0 μs (top), 8 μs (middle), and 16 μs (bottom) (Correia Rodrigues et al. 2014)

Despite the fact that the injector angle is 60°, the postprocessing of experimental data shows different results. The relation between the radial position on each elevation above the injector with its corresponding angle is depicted in figure (3.2) and the correlation is given in equation (3.1). If the elevation is not far from the injector, the gas phase cannot deviate the droplet from the straight line on which the droplet proceeds. In this equation, R and x represent the radial and axial position of an arbitrary point; R_0 is half of the injection diameter, which is assumed to be 0.75 mm.

$$\tan(\alpha) = \frac{R - R_0}{x} \tag{3.1}$$

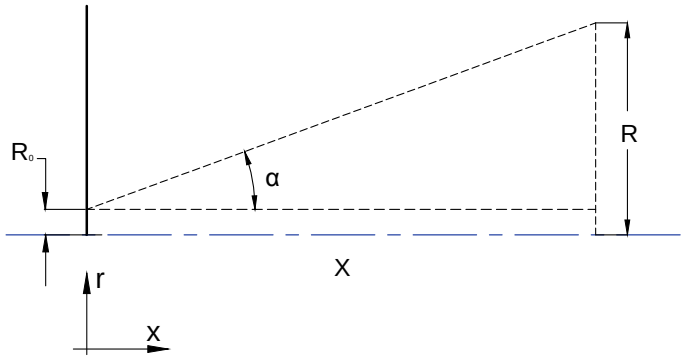

Figure 3.2: The relation between the position and the corresponding angle (α)

Considering the geometry, any experimental data at any radial and axial position can be mapped to its corresponding angle. Therefore, droplet concentrations vs the angle at two elevations of 8 mm and 10 mm are illustrated for the hot-diluted coflow case in figure (3.3) and for the cold coflow case in figure (3.4). These two elevations are the lowest elevations for which the experimental data are available; thus, the gas-phase effect is minimum and equation (3.1) can be used. For different ranges of droplet diameters, the figures show that the maximum concentration of droplets occurs between 35° and 40°. To choose the injector half-angle, the results from the cold coflow are more realistic for the injector, since the mean velocity for the hot-diluted coflow case is approximately ten times more than the cold coflow case (see table (1.2)). Hence, the most appropriate injector half-angle is chosen to be 40°.

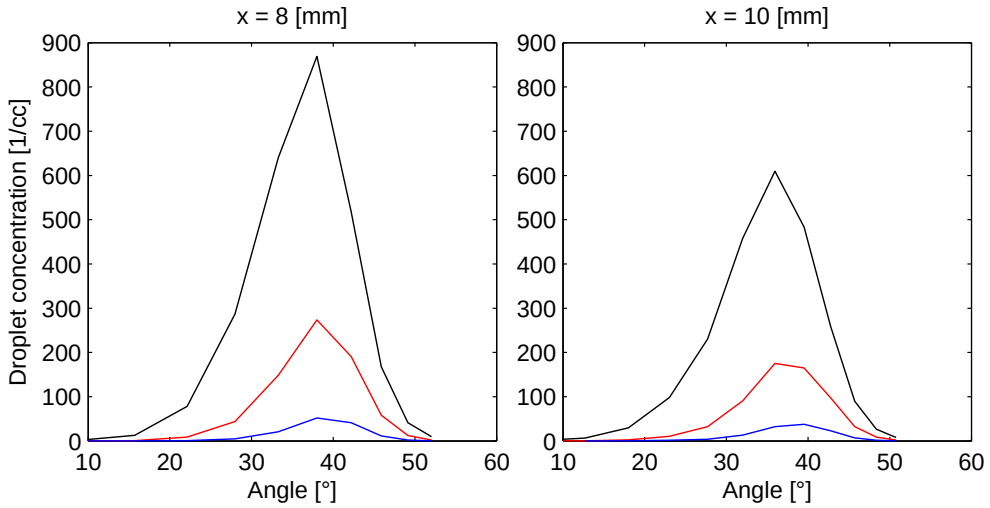

Figure 3.3: Experimental droplet concentration for different droplet diameter ranges in the hot-diluted coflow case (SHCiii) at two different elevations. Black line: droplet diameter = [30,40] μm, red line: droplet diameter = [40,50] μm, and blue line: droplet diameter = [50,60] μm

It is important to note that only some droplet diameters are included in the figures, because: firstly, the small droplets are not shown that they could easily be deviated by the gas phase even at low elevations. Secondly, the number of droplets with large diameters is not sufficient to show correctly the behavior of the injector.

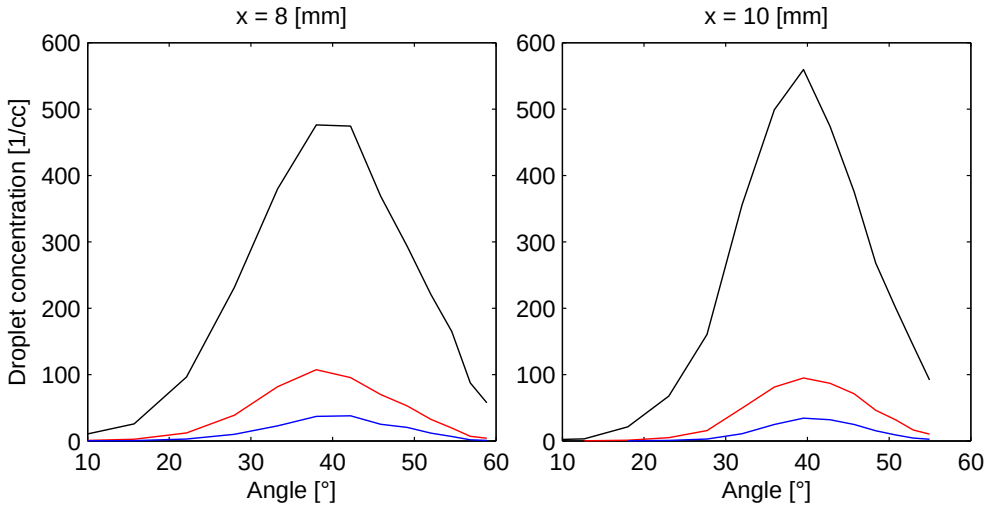

Figure 3.4: Experimental droplet concentration for different droplet diameter ranges in the cold coflow case (SCCii) at two different elevations. Black line: droplet diameter = [30,40] μm, red line: droplet diameter = [40,50] μm, and blue line: droplet diameter = [50,60] μm

3.1.2 Hot-Diluted Coflow Configuration

The starting point for any case of computational fluid dynamics is to define the domain of solution and its boundaries. The final domain used in this study is shown in figure (3.5). It is a two-dimensional domain representing an axisymmetric configuration. The length of the domain (in axial direction) is 300 mm while its width (in radial direction) is 150 mm. The injector is placed at the origin.

There are two reasons that these small values were assigned whereas larger domains have been used in different burners (Heye et al. 2014). First of all, the experimental data is only available up to 60 mm above the injector, so the domain must be large enough that the results in the zone between the injector and the elevation of 60 mm are not affected. After checking the results with larger domains, the effects of the outflow is negligible in this domain; hence, this smaller domain decreases the need for a large number of cells. The second reason is the definition of boundary condition at the ambient air inlet. In spite of the fact that the coflow is completely specified from the experimental setup, there is no data to specify the ambient air inlet, so the specification of this boundary condition is based on the furthest data available for the coflow, and it can be a good approximation if the length of this boundary is short.

The domain has two inlets: coflow and ambient air. The former inlet is the hot-diluted coflow provided by the secondary burner, while the latter is the fresh ambient air. They are both set to be velocity inlet boundary conditions. The injector wall is defined as the wall boundary condition. Because of the assumption of axisymmetric flow, the lower boundary is the axis. The top boundary condition is set symmetry, that makes using the pressure inlet/outlet unnecessary. Finally, as long as the inlet boundary conditions are velocity inlet, no additional information is necessary to be specified for the outflow.

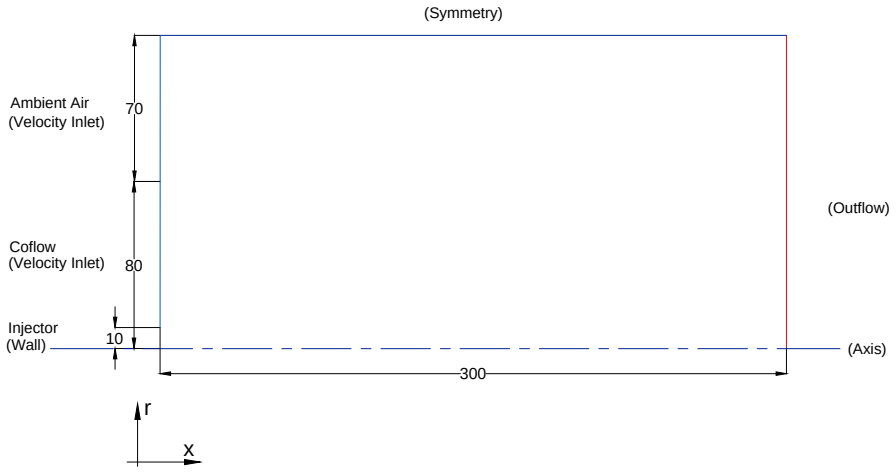

Figure 3.5: Numerical simulation domain and its boundary conditions

After defining the domain of solution, the models and their parameters deployed in ANSYS Fluent are discussed. Initially, three main turbulence models are used in this study: Reynolds stress, standard k-ε, and realizable k-ε models. Since they are completely integrated into ANSYS Fluent, there is no need to change any parameter of the models.

Combustion is the next model, For both the steady flamelet and FGM models, their tables should be generated. The flamelet table can be calculated based on two inputs: the chemical mechanism and the boundaries of the flamelet. The chemical mechanism is based on the work of Röhl & Peters (2009). This mechanism consists of 228 elementary reactions with 38 species.

The flamelet table is generated according to the boundaries of the fuel and oxidizer streams defined in table (3.1), where X represent the mole fractions. The fuel stream is ethanol at its approximate boiling temperature ($T_{boiling} = 351$ K).

Table 3.1: The hot-diluted coflow case flamelet boundaries

Oxidizer	Temperature	1360 K
	X_{O_2}	0.08705
	X_{CO_2}	0.05537
	X_{H_2O}	0.10933
	X_{N_2}	0.74825
Fuel	Temperature	350 K
	$X_{C_2H_5OH}$	1.00000

The radial profile of temperature for the oxidizer at the coflow inlet does not spread evenly, and it varies between 1100 K and 1400 K; therefore, the mass-weighted average of temperature, which is 1360 K, is specified as the oxidizer temperate to generate the flamlelet table. Moreover, only the oxygen mole fraction at the coflow inlet is available from the experimental data. Therefore, based on the assumption of equilibrium, the complete composition at the coflow was calculated by the in-house code “FLAME” (Ma et al. 2013).

In the next step, the parameters of the discrete phase model are assigned. That is shown in table (3.2). They are the necessary parameters to specify completely the injector in the LISA model. In section (3.1.1), the reasons why the half-angle and the injector diameter are different from the experimental setup (table 1.2) were explained , but the other parameters are explained here.

Table 3.2: Discrete phase parameters of the pressure-swirl atomizer

Properties	Value
Half-angle	40°
Dispersion angle	20°
Diameter	0.0015 m
Temperature	300 K
Pressure	6 bar
Number of parcels	5000
Mass flow rate	1.46 kg/hr
Liquid fuel	Ethanol

The temperature of the liquid fuel for the LISA model is assumed to be 300 K since the exact value is unknown. Although a flow of cooling water cools down the injector, the exhaust gas with an approximate temperature of 1300 K is in direct contact with the head of injector; thus, the cooling water and the hot gases may cancel the effects of each other, so the temperature of 300 K is only an estimate.

Still, the dispersion angle must be assigned. Moreover, despite the specification of pressure in table (1.2), the pressure used in this model is approximately half of the pressure used in the experiments (shown in table (1.2)). When the original pressure was set, the discrete phase model (DPM) results were completely different from the obtained experimental data, so the pressure was calibrated in order to achieve the best fit on the sauter mean diameter (SMD), axial velocity (u), and radial velocity (v) of droplets (Ma et al. 2013). The DPM results were compared with the experimental data for different droplet sizes at different elevations above the injector. For instance, SMD, u, and v are illustrated in figures (3.6) to (3.8), at different elevations and for droplet diameters between 30 μm and 40 μm.

It is important to note that there are also other ranges of droplet diameters; as an illustration, the results for droplet diameters between 30 μm and 40 μm are given. However, when the parameters of the discrete phase are set, other droplet diameters must also be considered. Hence, satisfying SMD, u, and v values for different elevations and droplet diameters can be difficult, especially because of the strong non-linearity in the interconnection between different models.

As the injector pressure changes, vertical shifts occur in all of the figures. If the pressure increases, SMD will decrease while the axial and radial velocities will increase. Accordingly, the pressure of 6 bar seems acceptable since the velocities and SMD match the experimental results.

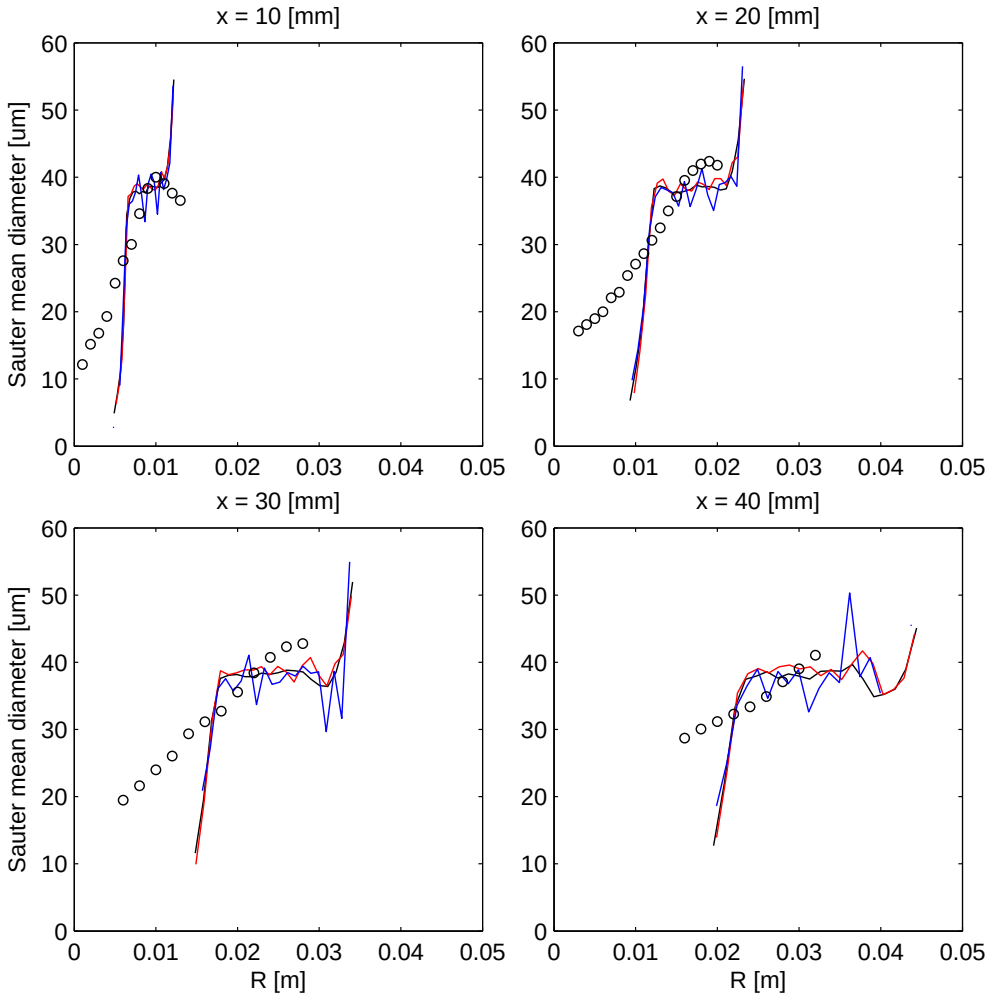

Figure 3.6: Sauter mean diameter (SMD) of droplets (SHCiii). Symbols: experiment, black line: 50000 parcels, red line: 5000 parcels, and blue line: 500 parcels

Moreover, in these figures, the black, red, and blue lines represent the results with different number of parcels, respectively, 50000, 5000, and 500 parcels. It can be seen that the profiles are virtually similar. This denotes that it is possible to use small number of parcels. However, according to the fluctuations in the DPM results of 500 parcels, the number of parcels are not enough to correctly capture the stochastic behavior of injection with quite a few droplets, so it is better to use more parcels. Since this can cost further computational time, the number of parcels in the order of 5000 can be a suitable choice.

Finally, according to figures (3.3) and (3.4), the dispersion angle could be any value based on the width of droplet concentration profiles. Nonetheless, by increasing the dispersion angle, the numerical results deviate from the experimental data; therefore, by trial and error, 20° can be a good approximation of the dispersion angle.

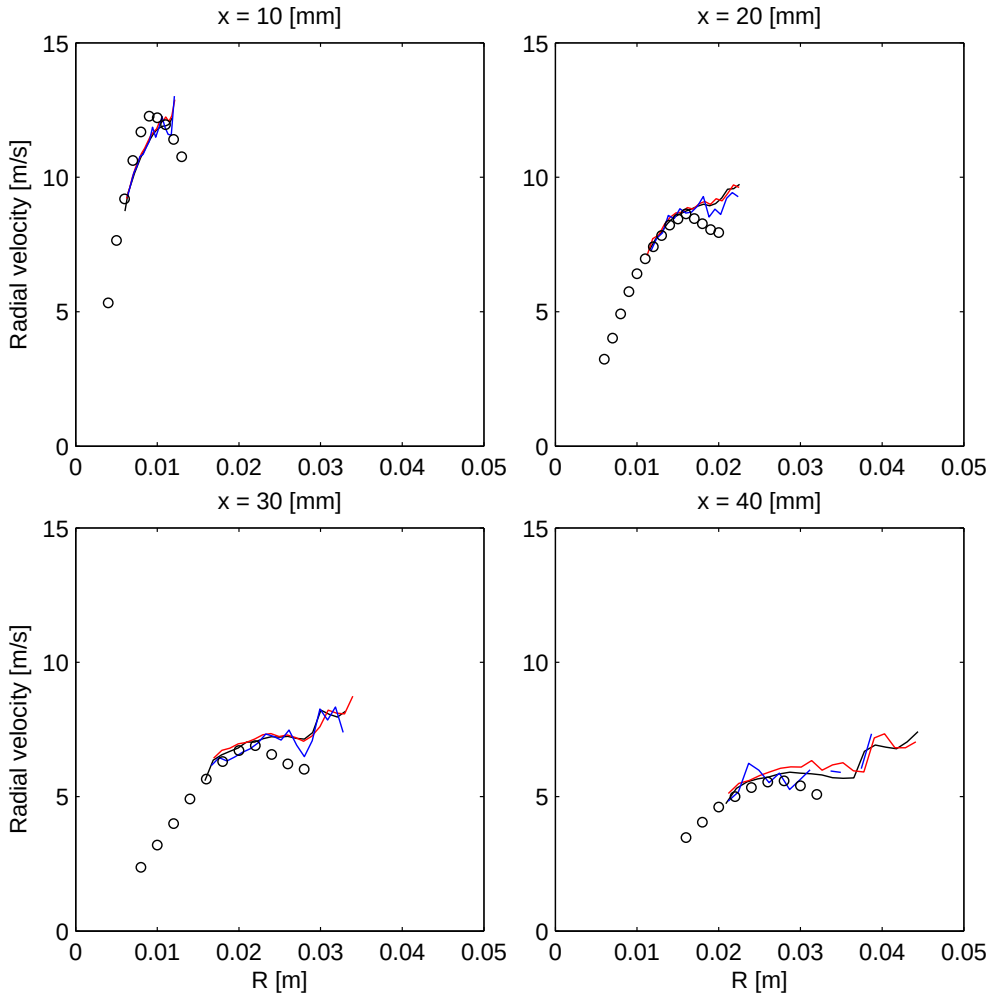

Figure 3.7: Radial velocity of droplet diameters between 30 μm and 40 μm (SHCiii). Symbols: experiment, black line: 50000 parcels, red line: 5000 parcels, and blue line: 500 parcels

When numerical and experimental results are compared in figures (3.6) to (3.8), it can be seen that for high elevations, in some radial positions, the numerical data is available while there is no experimental data. This can be the result of different factors such as different sampling and postprocessing of the numerical and experimental data, or the evaporation model that could not predict the correct evaporation rate of droplets.

3.1.2.1 Cold Coflow Configuration

Even though the the cold and hot-diluted coflow cases are completely different, the configuration of models for the cold coflow case is similar to the hot-diluted coflow case. The domain used in this study is exactly the same as the hot-diluted coflow case; however, the boundary conditions are changed according to the cold coflow case experimental data. Furthermore, there is no need to change any parameters of the turbulence models.

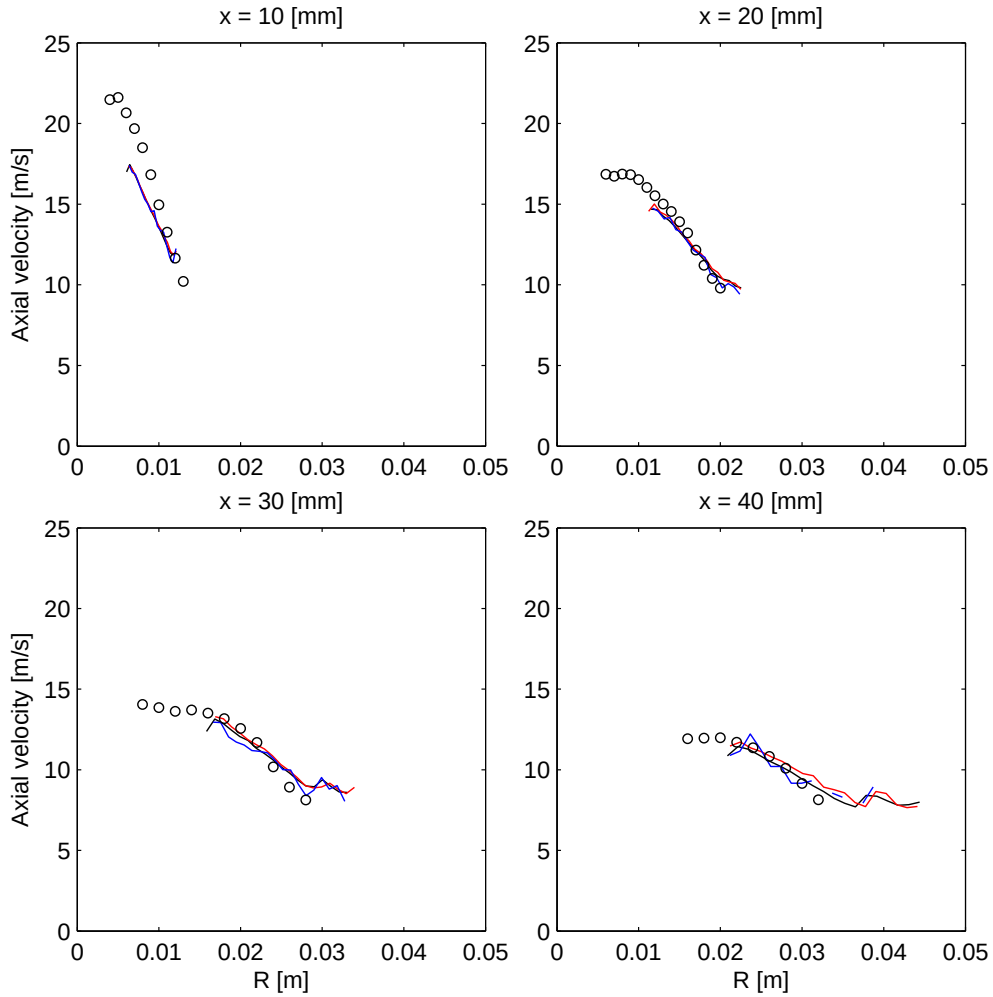

Figure 3.8: Axial velocity of droplet diameters between 30 μm and 40 μm (SHCiii). Symbols: experiment, black line: 50000 parcels, red line: 5000 parcels, and blue line: 500 parcels

Because of different gas-phase inlet temperature and composition, the flamelet table has to be changed. The boundaries of the flamelet table is defined in table (3.3). The composition and temperature of the oxidizer are specified from the ambient air.

Table 3.3: The cold coflow case flamelet boundaries

Oxidizer	Temperature	300 K
	X_{O_2}	0.21
	X_{N_2}	0.79
Fuel	Temperature	350 K
	$X_{C_2H_5OH}$	1.00

Lastly, for the discrete phase model, the parameters are specified according to the geometry of injector such as the diameter, half-angle, and dispersion angle do not need to be changed. Furthermore, as discussed in previous section, 5000 parcels is sufficient to capture the effects of the discrete phase while it is not so computationally expensive. The temperature and pressure are assumed to be similar to the hot-diluted coflow case since the temperature of ethanol is approximately the same as the ambient temperature (300 K); moreover, the pressure in the real case is a little higher than the hot-diluted coflow case (see table (1.2)), so the pressure of 6 bar can be used for the cold coflow case as well. The mass flow rate of ethanol for the cold coflow case is 1.7 kg/hr, which is different from the hot-diluted coflow case.

3.2 Model Validation in the Hot-Diluted Coflow Case

As mentioned in the introduction, a flameless burner works based on the recirculation of exhaust gases after combustion and mixing with the fresh air in order to increase the temperature of the mixture while its oxygen content is reduced. For creation of a homogeneous mixture of exhaust gases and the fresh air, intense turbulence in the burner is crucial, which indicates that high velocities are necessary. As a result, combustion in this type of burners can be simplified as the injection of a liquid fuel into a hot high-velocity coflow. This is similar to the experimental setup, where the injector is located inside a channel providing the flow with desired velocities, temperatures, and oxygen concentrations (see figure (1.2)). The experimental data are needed to validate the numerical simulation of the hot-diluted coflow case.

Since the experimental measurement for temperature and velocities were based on different approaches, the data for each set are available at different elevations above the injector. Therefore, numerical and experimental temperature profiles are compared at 15 and 40 mm elevations while the velocity profiles are compared at 10 and 30 mm elevations.

In two different parts for the steady flamelet and FGM models, the difference in turbulence models are compared. These turbulence models are: the Reynolds stress model, standard k-ε, and realizable k-ε.

3.2.1 Steady Flamelet Model

In figure (3.9), the axial velocities of three turbulence models at two different elevations are shown. In spite of the fact that the prediction of velocities are acceptable by these three models, there are two points to consider. Firstly, all the models could not capture the correct axial velocity profile in the vicinity of the axis; this can be seen obviously from the results at the elevation of 10 mm. Moreover, the numerical peak velocities, which are approximately the same for all the models, are different from the experimental peak velocity.

One of the possible reasons for wrong prediction near the axis is the spray model. As it can be seen from figure (3.8), the spray model does not provide enough droplets next to the axis. Even if a droplet in this zone has enough momentum, the number of droplets is so small that those droplets cannot insert the required momentum to accelerate the gas phase near the axis. Likewise, the peak velocities are in the zone near the axis, so the predicted peak velocities are less.

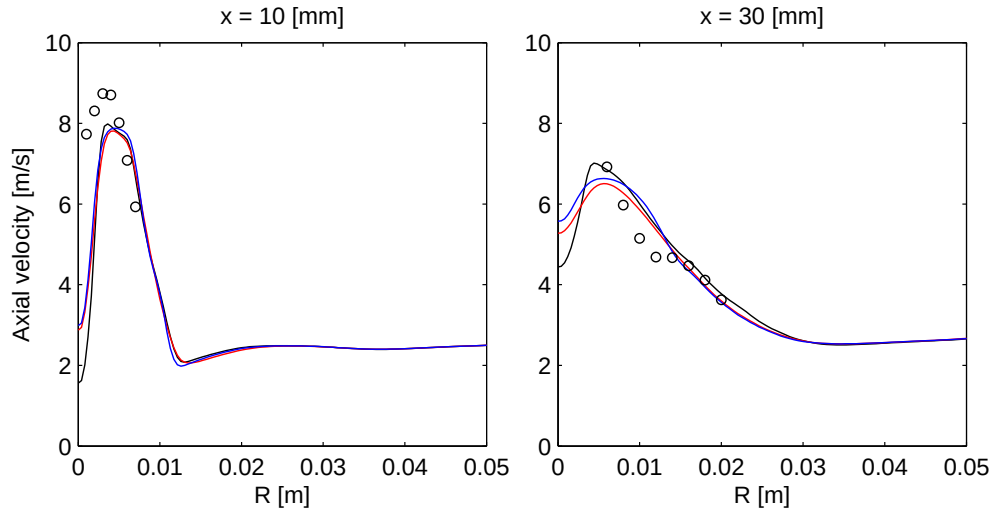

Figure 3.9: Gas-phase axial velocity for the steady flamelet model (SHCiii). Symbols: experiment, black line: Reynolds stress model, red line: standard k-ε, and blue line: realizable k-ε

Radial velocities shown in figure (3.10) are in harmony with the experimental results, but the problem of capturing the correct peak velocity at the lower elevation (i.e. x = 10 mm) still remains. According to the numerical results, there are one peak and two dips in the radial velocity profiles for both elevations; the first dip, which is close to the axis, has been captured well with all of the turbulence models. Nonetheless, the peak radial velocity, which is located between two dips, has not been captured well with any of the turbulence models although the k-ε models predict this point better than the Reynolds stress model. Similarly, This can be explained by the spray model that does not provide enough droplets near the axis to accelerate the gas phase. Likewise, for the higher elevations (x = 30 mm), these two dips and one peak can be observed with smaller magnitude. In the following two paragraphs, the reasons why there are two dips and one peak are given only for the lower elevation (x = 10 mm); it can be generalized to other elevations.

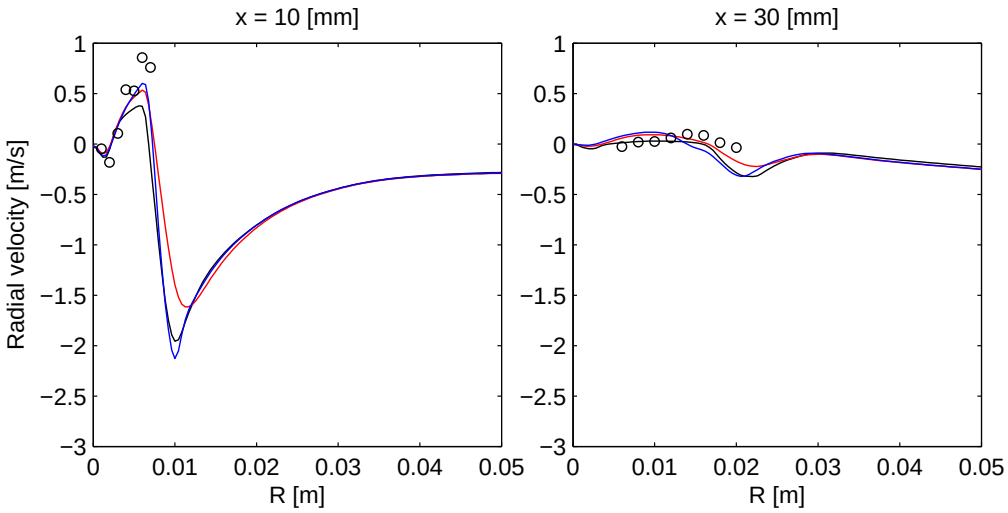

Figure 3.10: Gas-phase radial velocity for the steady flamelet model (SHCiii). Symbols: experiment, black line: Reynolds stress model, red line: standard k-ε, and blue line: realizable k-ε

Starting from the axis, the first change in radial velocities occurs when the negative velocity becomes positive. This can be explained by the streamwise decrease in the gas-phase axial velocity. In figure (3.11), the experimental gas-phase axial and radial velocities for two elevations close to each other (10 mm elevation vs. 12 mm elevation) are depicted. From the left figure, it can be seen that at 3 mm away from the axis, the peak axial velocity occurs for both the elevations; still, from 10 mm elevation to 12 mm elevation, the axial velocity at similar radial positions decreases much faster than the other neighbor points; as a result of the continuity of mass, it is concluded that the difference in axial velocities must be added to the radial velocities. Hence, for radial positions between 0 and 3 mm, the radial velocity is negative while radial positions between 3 mm and 10 mm present positive radial velocities.

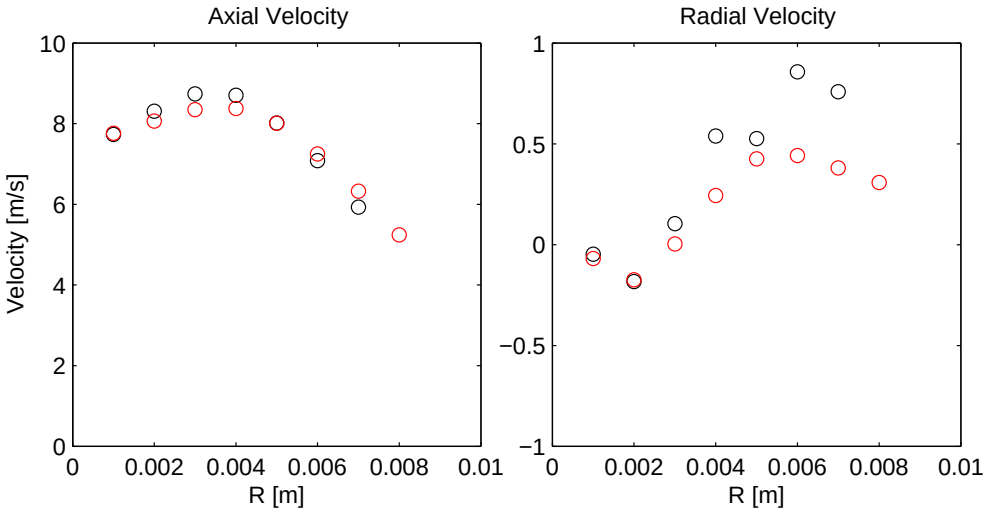

Figure 3.11: Experimental gas-phase velocity components (SHCiii). Black symbols: 10 mm elevation and red symbols: 12 mm elevation

Furthermore, this positive radial velocity is caused by the momentum exchange between droplets moving outward and the gas phase, so the gas phase also accelerates in the positive radial direction. Out of this zone where the radial velocity is positive, there is a large zone with negative velocities. This negative radial velocity is caused by the hot-diluted coflow entrainment.

The temperature profiles are given in figure (3.12). As it can be seen the profiles match well with the experimental data, except in two points.

The first point is the dip in temperatures near the axis. This can be related to the evaporation model. The infinite conductivity model overpredicts the evaporation rate; therefore, all the droplets are evaporated much faster than the reality. Although the number of droplets provided by the spray model is small, all of them are evaporated fast, which makes the mixture near the axis rich. The mixture fraction is shown in figure (3.13). This rich mixture cannot burn well because of its large deviation from the stoichiometric mixture fraction ($Z_{st} = 0.045$). This situation was observed by Rochaya (2007). Furthermore, because of small radial velocity and large axial velocity near the axis, it is difficult to make the mixture lean by mixing with the coflow; therefore, this dip is present in the low and high elevations.

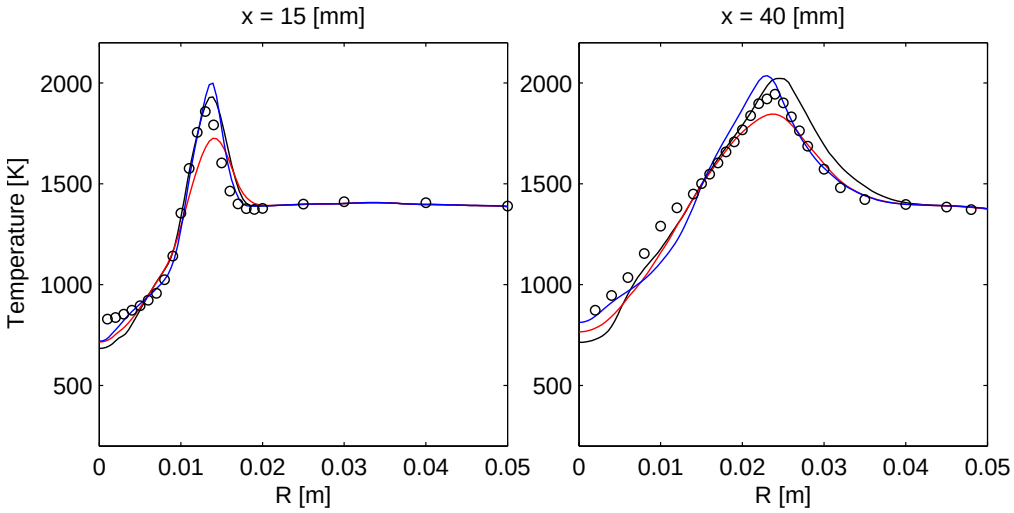

Figure 3.12: Gas-phase temperature for the steady flamelet model (SHCiii). Symbols: experiment, black line: Reynolds stress model, red line: standard k-ε, and blue line: realizable k-ε

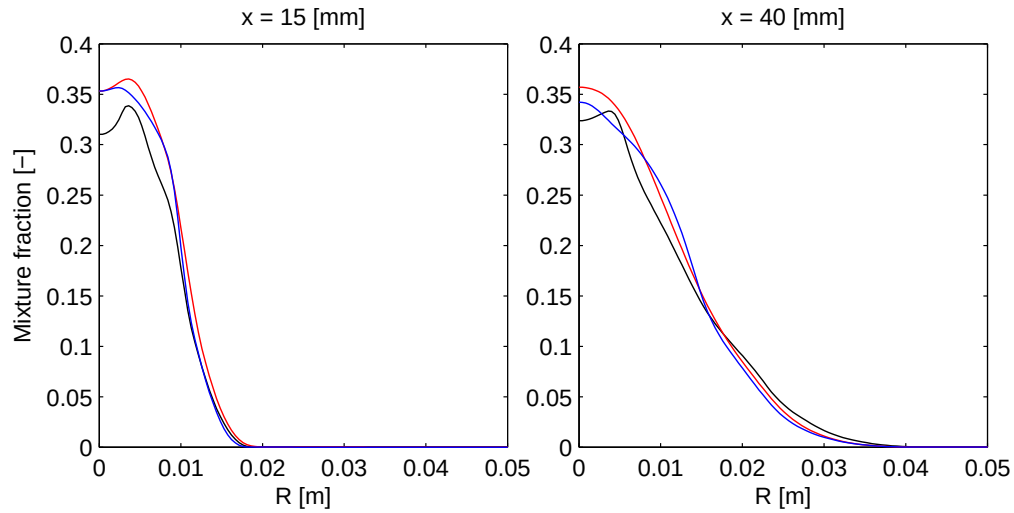

Figure 3.13: Gas-phase mixture fraction for the steady flamelet model (SHCiii). Black line: Reynolds stress model, red line: standard k-ε, and blue line: realizable k-ε

The second point is where the peak temperatures are located. Although the Reynolds stress and realizable k-ε models overpredict the peak temperature, the standard k-ε model underpredicts the temperature almost everywhere. The most probable reason why the models do not predict the peak temperature may be the scalar dissipation rate as shown in figure (3.14). The scalar dissipation predicted from the standard k-ε model is comparatively much higher than the two other cases. As the scalar dissipation increases, the flame approaches extinction and the flamelet table temperature decreases. Therefore, for a given mixture fraction, the corresponding temperature would be less for the standard k-ε model than the realizable k-ε and Reynolds stress models.

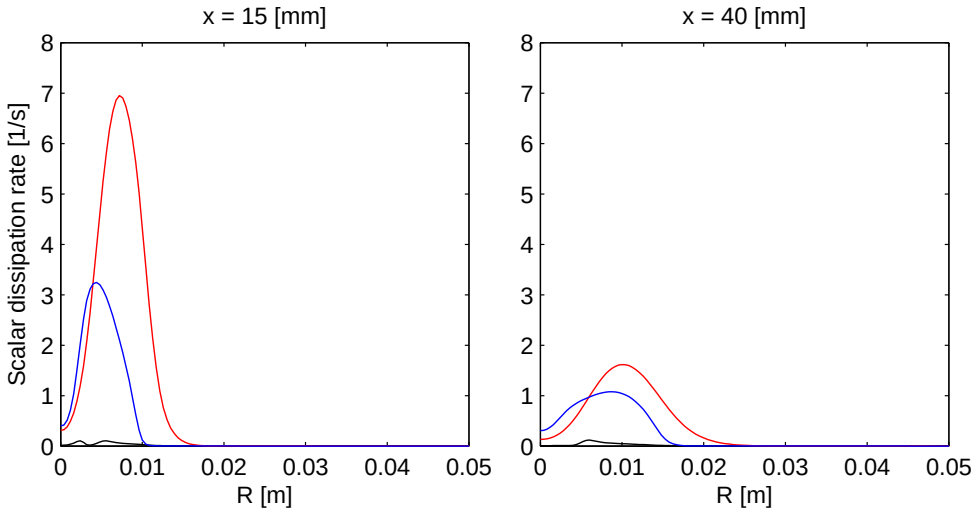

Figure 3.14: Scalar dissipation rate for the steady flamelet model (SHCiii). Black line: Reynolds stress model, red line: standard k-ε, and blue line: realizable k-ε

It is important to note that the scalar dissipation rate can be parameterized by its stoichiometric value, which imposes strain on the flamelet and changes its structure (Müller et al. 2013); moreover, the model developed for the mean stoichiometric scalar dissipation rate $\widetilde{\chi_{st}}$ (equation (2.19)) is a function of both the mixture fraction and the turbulence variables; therefore, the structure of flame as well as the temperature profile can be affected directly by the turbulence variables. Thus, different prediction of k and ε by different turbulence models may change the flame structure.

3.2.2 Flamelet Generated Manifold Model

In this section, the results of different turbulence models are given when the Flamelet Generated Manifold model is used to describe local flame structure.

Figures (3.15) and (3.16) show the axial and radial velocity profiles. While the results for the radial velocities are comparable in accuracy with the steady flamelet model, the axial velocities remain significantly underpredicted. Since the only difference between these set of results is in their combustion models, which are responsible for production/consumption of species as well as the heat release, the temperature profile is checked as shown in figure (3.17).

When temperature profiles for the steady flamlet model (figure (3.12)) and the FGM model (figure ((3.17)) are compared, there are some similarities such as the low peak temperature of the standard k-ε model. Still, there are important differences. First, the temperature profiles for different turbulence models at both elevations show a considerable difference (up to 300 K) between the axis and the the peak temperatures. Second, the Reynolds stress model experiences a decrease and then an increase in temperature in vicinity of the axis.

As a result of low temperature prediction, the density of the gas-phase mixture is predicted more than the reality as shown by the experimental data; therefore, because of the constant mass flow rate of the hot-diluted coflow, the velocity must decrease as it can be seen from the figure (3.15).

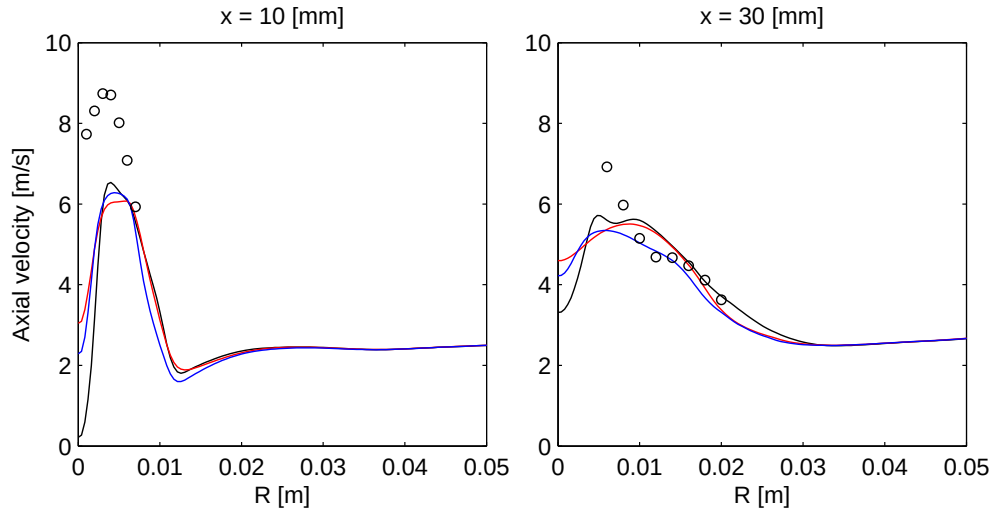

Figure 3.15: Axial velocity for the FGM model (SHCiii). Symbols: experiment, black line: Reynolds stress model, red line: standard k-ε, and blue line: realizable k-ε

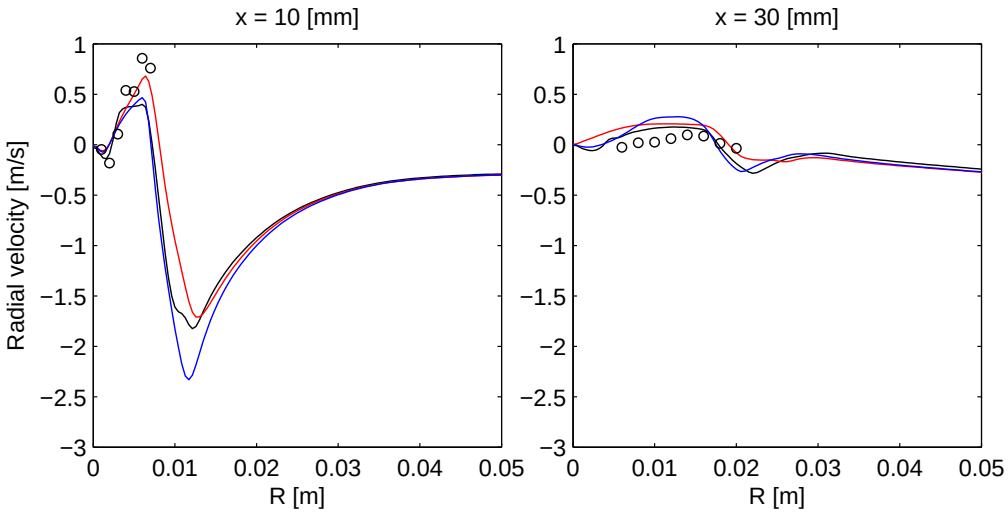

Figure 3.16: Gas-phase radial velocity for the FGM model (SHCiii). Symbols: experiment, black line: Reynolds stress model, red line: standard k-ε, and blue line: realizable k-ε

But it is of paramount importance to realize why the temperature profiles are different from the experimental data as well as the steady flamelet model. In the flamelet model, the effect of the scalar dissipation rate is studied in order to realize the difference in temperature profiles for different turbulence models. However, in the FGM model, the progress variable specifies the temperature according to the mixture fraction and enthalpy loss/gain. The progress variable profiles are shown in figure (3.18).

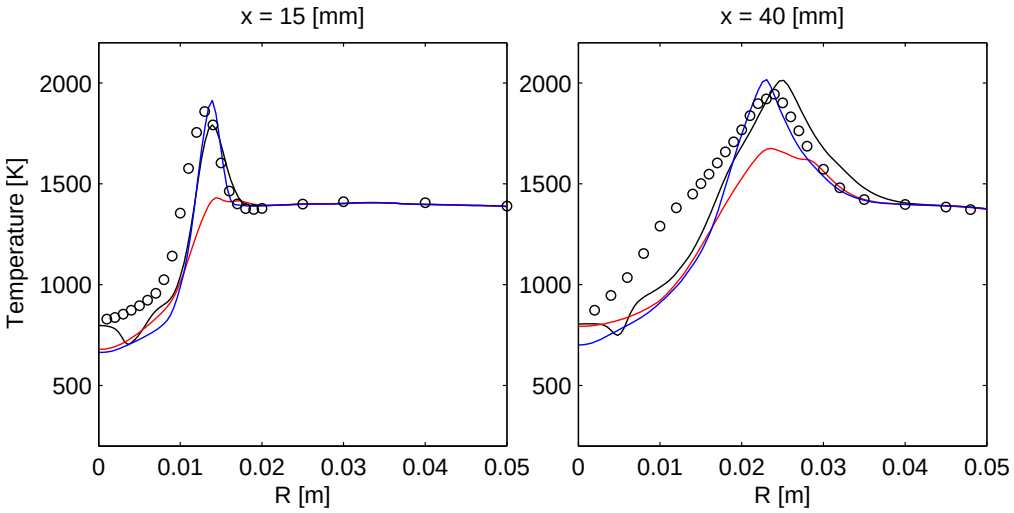

Figure 3.17: Gas-phase temperature for the FGM model (SHCiii). Symbols: experiment, black line: Reynolds stress model, red line: standard k-ε , and blue line: realizable k-ε

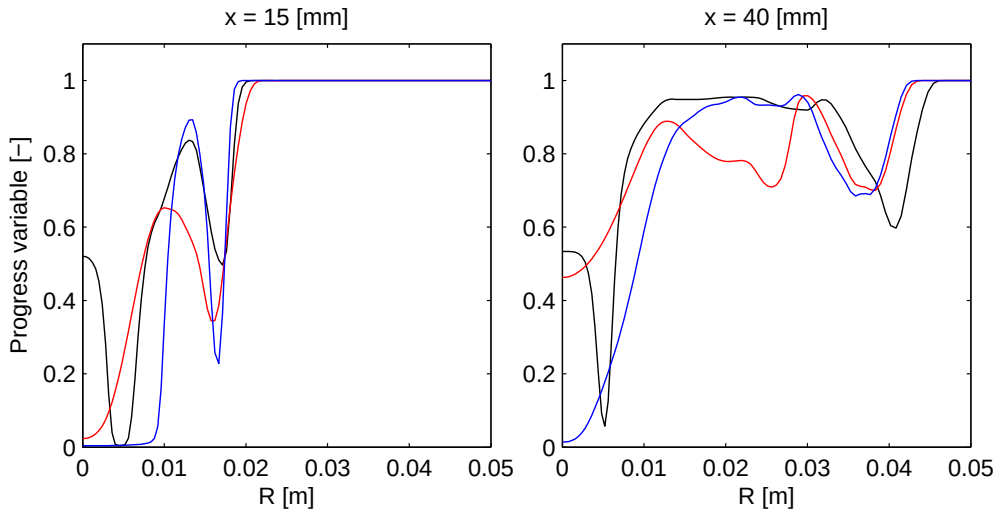

Figure 3.18: Progress variable for the FGM model (SHCiii). Black line: Reynolds stress model, red line: standard k-ε, and blue line: realizable k-ε

At the lower elevation (x = 15 mm), the progress variable for the k-ε models starts from zero, then increases to its maximum values, which correspond to the maximum temperatures; since the maximum progress variable for the standard k-ε is smaller than two other turbulence models, its peak temperature is also lower than the others. Then, the progress variables decrease to their minimum values where the outer layer of the hot-diluted coflow mixes with the fuel-oxidizer mixture. Finally, the progress variable increases to unity for all the turbulence models because there is only the products of the secondary burner in the outer layer.

For the Reynolds stress model, the progress variable starts from 0.5 and then decreases to zero, instead of starting from zero at the axis ; this is the reason why there is a dip for the Reynolds stress model in its temperature profile while this is not the case for the k-ε models. The explanation may come from the small axial velocity near the axis predicted by the Reynolds stress model (see figure (3.15)). This increases the residence time of the mixture very close to the axis, so the reaction may occur, and the progress variable is not zero; however, the radial velocity increases significantly as moving away from the axis, so the residence time decreases quickly and no reaction may occur, which makes the progress variable decrease from 0.5 to 0.

For the higher elevation (x = 40 mm), the progress variable profiles expand as droplets disperse in the domain. Moreover, the progress variables reach their maximum values for the fuel-oxidizer mixture, so the temperatures are higher in this elevation compared to the lower one, but the progress variable for the standard k-ε does not reach the maximum value of unity except in one point. Therefore, the temperature is underpredicted.

3.2.3 General Conclusion

In this section, different turbulence and combustion models are compared. The Reynolds stress and realizable k-ε models show comparatively similar results with good prediction of temperature profiles; however, the standard k-ε model could not predict the peak temperature, which may be related to different prediction of turbulence variables.

In combustion models, the steady flamelet predicts temperature profiles better than the FGM model. This may be related to the FGM table and the definiton of the progress variable. However, this is only correct for the ignited zone. The OH concentration for two combustion models along with the Reynolds stress model are depicted in figure (3.19). OH Laser-Induced Fluorescence (LIF) imaging is an approach to experimentally study the flame front, so OH concentration can be a good representative of the flame structure.

Although the FGM model could not capture the temperature profile as good as the steady flamelet model, the steady flamelet model cannot predict the lift-off because of the “mixed is burnt” assumption, and the flame is attached to the injector. Moreover, the flame structures in both combustion models are different. While the steady flamelet model only predicts one zone with the highest rate of reaction, the FGM model shows two zones in which the reaction occurs.

This difference in flame structure and lift-off can cause a lot of different results such as different rate of evaporation, velocity and temperature profiles, etc. Still, the evaporation rate is not affected much by the lift-off height because of the high temperature of the hot-diluted coflow case, which provides the required heat for evaporation of droplets.

3.3 Parameter Study

The focus in previous section was only on the validation of different turbulence and combustion models. Still, there are some models and options available in ANSYS Fluent that may increase the accuracy of predictions significantly, or have little effect on the final results. Some of them which were not covered in the previous section are studied in this section on the case of the hot-diluted coflow.

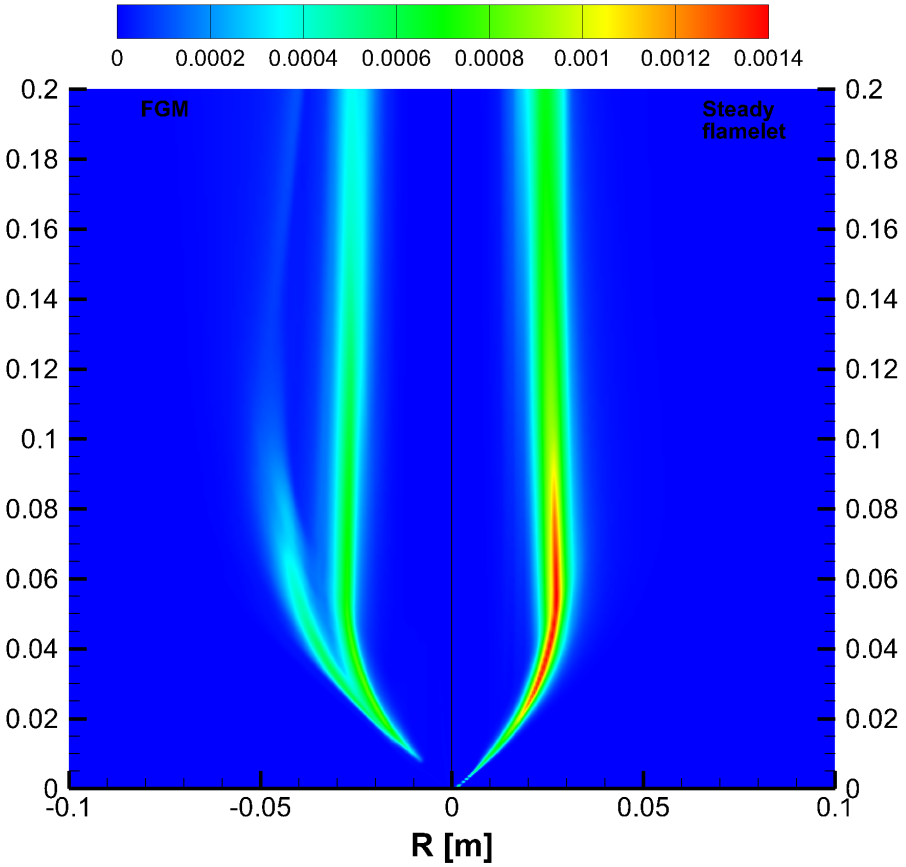

Figure 3.19: OH mass fraction contour for the hot-diluted coflow case. Left: the FGM model, right: the steady flamelet model

It should be pointed out that the combination of the Reynolds stress and FGM models is employed to investigate different options and models. This is the combination used in most of the cases unless it is stated that other turbulence or combustion models are employed.

3.3.1 Turbulence Two-way Coupling

As mentioned in section (2.4.3), in general, only mass, momentum, and energy are exchanged between two phases in ANSYS Fluent; still, droplets may affect the turbulence by producing or dissipating the turbulent kinetic energy. "Turbulence Two-way Coupling" is the option to include the effects of droplets on the gas-phase turbulence variables.

In figures (3.20) and (3.21), the Reynolds stress in the axial direction ($\widetilde{u''u''}$) is given for the steady flamelet model. The former figure shows $\widetilde{u''u''}$ without "Turbulent Two-way Coupling" option while the latter includes this option. Accordingly, the performance of the k-ε models has improved significantly. It should be noted that this option is not available for the Reynolds stress model; however, this model predicts Reynolds stresses properly without "Turbulent Two-way Coupling" option.

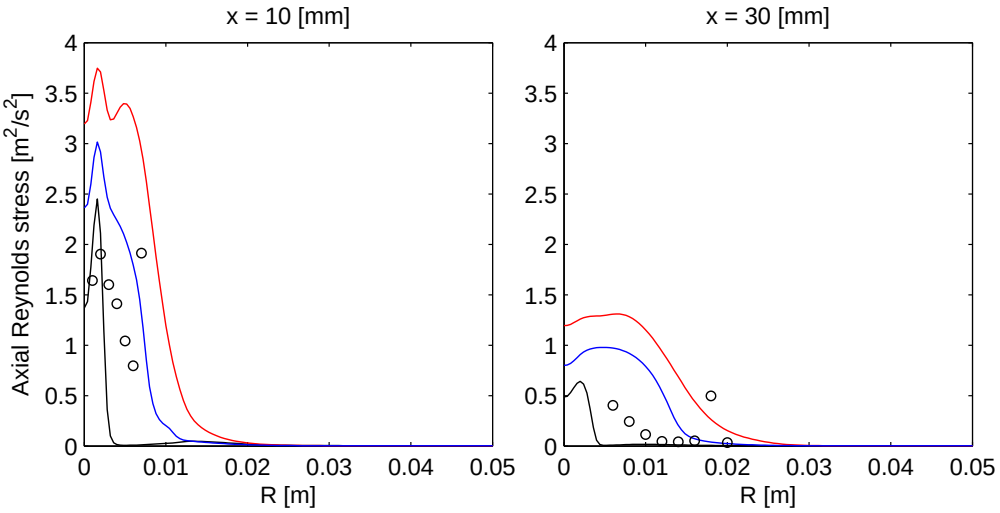

Figure 3.20: Gas-phase axial Reynolds stress ($\widetilde{u''u''}$) for the steady flamelet model without "Turbulent Two-way Coupling" (SHCiii). Symbols: experiment, black line: Reynolds stress model, red line: k-ε Standard, and blue line: realizable k-ε

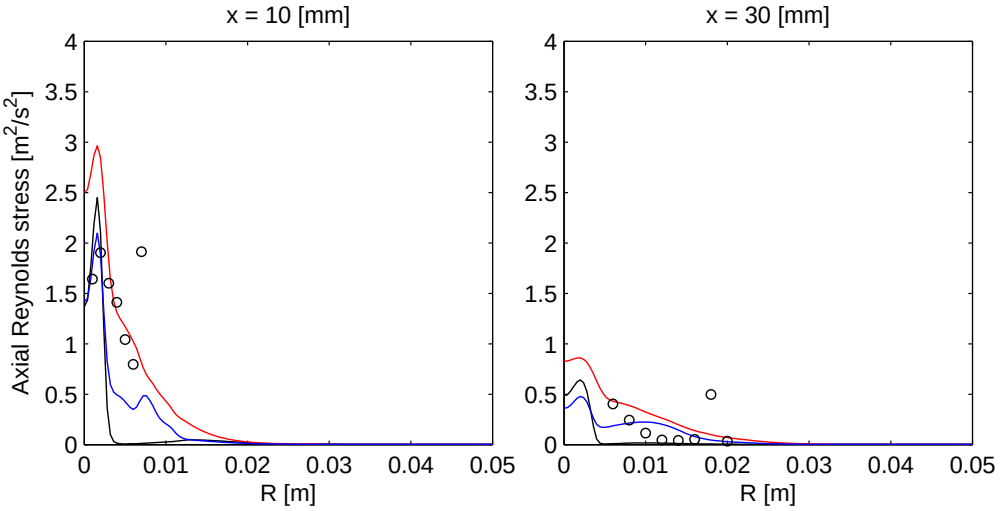

Figure 3.21: Gas-phase axial Reynolds stress ($\widetilde{u''u''}$) for the steady flamelet model with "Turbulent Two-way Coupling" for the k-ε models (SHCiii). Symbols: experiment, black line: Reynolds stress model, red line: standard k-ε , and blue line: realizable k-ε

From equation (2.19), the turbulence variables (k and ε) and the scalar dissipation rate are directly connected to each other; therefore, if the the Reynolds stresses are computed more accurately, it is expected that consequently the combustion variables as well as temperature profiles are computed more accurately. The temperature profiles for the steady flamelet model with "Turbulent Two-way Coupling" for different turbulence models are shown in figure (3.22). Comparing these temperature profiles with temperature profiles illustrated in figure (3.12) shows that the predicted results by the standard k-ε model with the "Turbulent Two-way Coupling" option has improved significantly while the changes of the realizable k-ε is negligible.

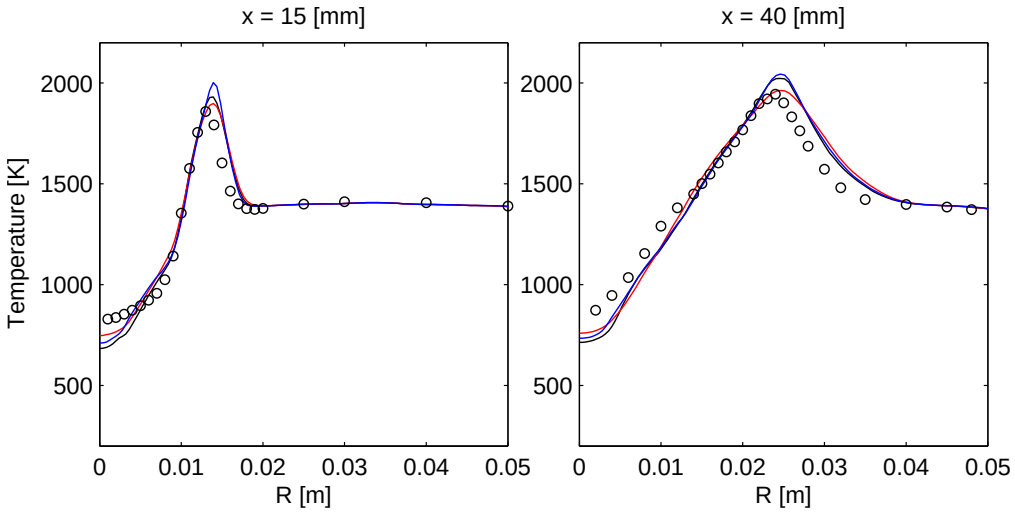

Figure 3.22: Gas-phase temperature for the steady flamelet model with "Turbulent Two-way Coupling" activated for the k-ε models (SHCiii). Symbols: experiment, black line: Reynolds stress model, red line: standard k-ε , and blue line: realizable k-ε

For the FGM model, the Reynolds stresses have improved similarly after applying this option, which are not shown here, but the resultant temperature profiles are given in figure (3.23). Comparing this figure with figure (3.17) shows significant improvement in the standard k-ε model results, so it can predict the peak temperature; still, little change does the realizable k-ε model show when "Turbulent Two-way Coupling" is activated for this model.

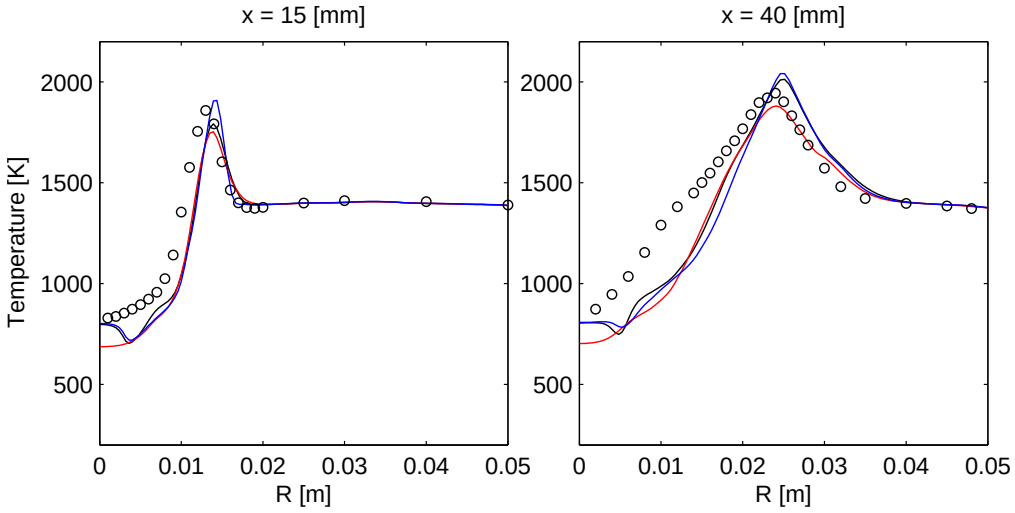

Figure 3.23: Gas-phase temperature for the FGM model with "Turbulent Two-way Coupling" activated for the k-ε models (SHCiii). Symbols: experiment, black line: Reynolds stress model, red line: standard k-ε , and blue line: realizable k-ε

The results given in this section confirm the importance of turbulence coupling between the gas and discrete phases, especially for the standard k-ε model. Therefore, if it is possible to activate the option in the standard k-ε model without any instability problem for solution convergence, more accurate results will be obtained.

3.3.2 Secondary Atomization and Coalescence

In the dense regime, which is in the vicinity of the injector, droplets are so close to each other that they may collide or they can split into smaller droplets during their development. These two effects can be considered when the "Stochastic Collision", "Coalescence", and "Breakup" options are activated in ANSYS Fluent. However, as explained in sections (2.4.1.2) and (2.4.4), these options are only available for unsteady injection.

In order to compare the effects of secondary atomization as well as coalescence, the sauter mean diameter (figure (3.24)) and the axial velocity (figure (3.25)) of droplets are compared at two low elevations (x = 8 and 12 mm) for two cases; one case uses the steady injection while the other uses the unsteady injection with all available options for coalescence and secondary atomization. The aim of choosing low elevations is to see the differences between the cases as close as possible to the injector and the dense regime.

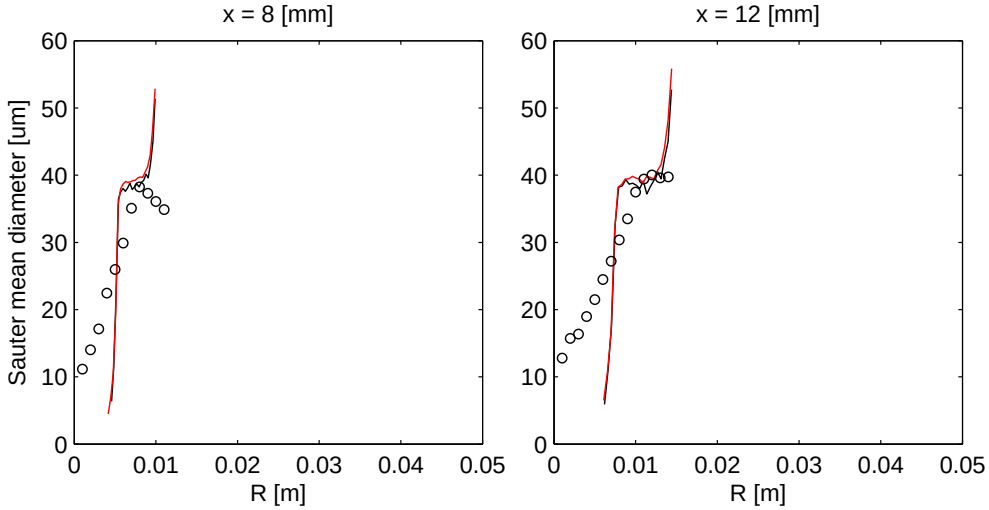

Figure 3.24: Sauter mean diameter (SMD) of droplets (SHCiii). Symbols: experiment, black line: steady injection, and red line: unsteady injection

According to these figures, the difference in the sauter mean diameter and axial velocity profiles is so small that it can be deduced that these two elevations are above the region where the dense regime is present, so the dense regime must cover very small region whose effects are not visible even in the lowest elevation (x = 8 mm). The reason for this behavior is related to the high temperature of the hot-diluted coflow, which evaporates droplets very close to the injector. Inasmuch as the the dense regime is only present in small region, it is concluded that there is no need to consider the secondary atomization and coalescence in this simulation.

3.3.3 Buoyancy

The effects of buoyancy are considered in ANSYS Fluent through source terms included in the transport equations of the momentum and turbulence variables. However, if the flame is small, it is argued that the effects of buoyancy can be ignored.

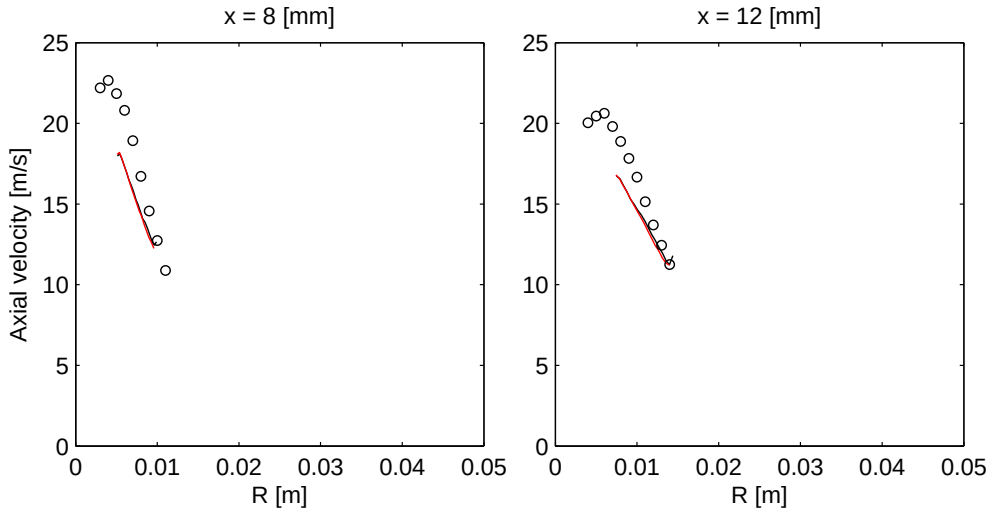

Figure 3.25: Axial velocity of droplet diameters between 30 μm and 40 μm (SHCiii). Symbols: experiment, black line: steady injection, and red line: unsteady injection

In figure (3.26), gas-phase axial velocity profiles at two different elevations are brought; for both elevations, the difference in velocities is small, and the buoyancy force does not accelerate the gas phase more than the case which it is not present.

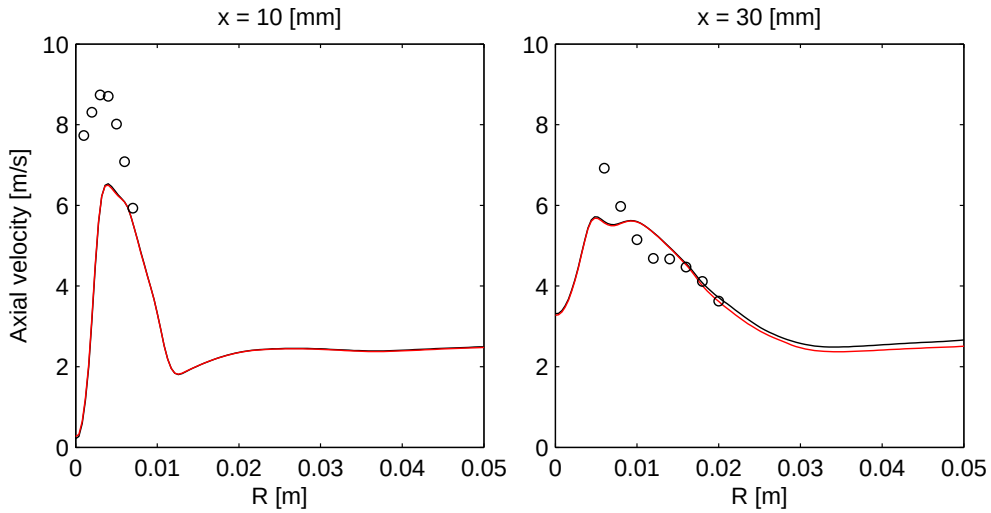

Figure 3.26: Gas-phase axial velocity (SHCiii). Symbols: experiment, black line: with buoyancy, and red line: without buoyancy

In addition to the momentum equations, buoyancy affects the turbulence variables, so it may affect the combustion models and temperature profiles as shown in figure (3.27); however, the difference in temperature profiles at different elevations is so small that its effects can be ignored.

Overall, the effects of buoyancy in such a small flame are negligible. The main reason can be the fact that the flame is small and the buoyancy force can be ignored compared to other driving forces such as the high-momentum of the coflow. However, it cannot be generalized to large flames similar to what happens in industrial furnaces.

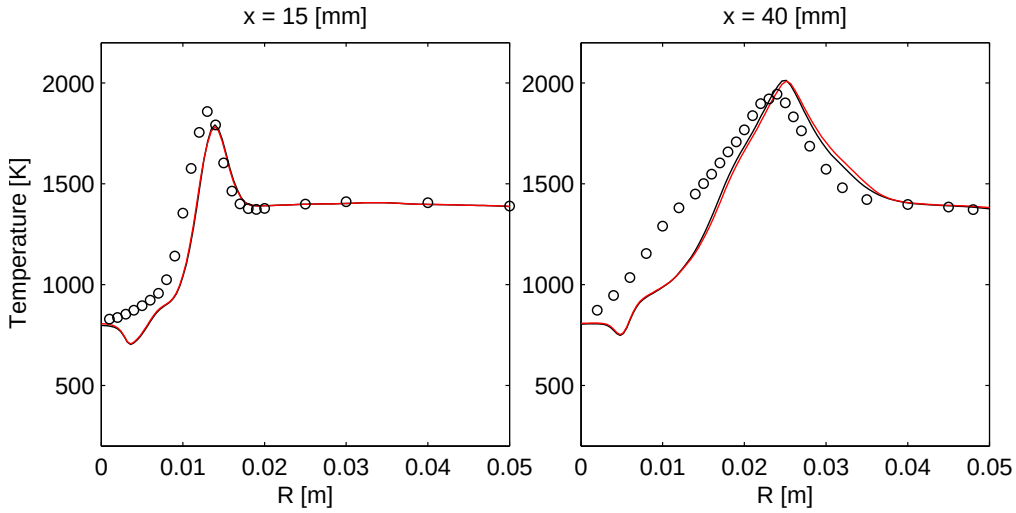

Figure 3.27: Gas-phase temperature (SHCiii). Symbols: experiment, black line: with buoyancy, and red line: without buoyancy

3.3.4 Radiative Heat Transfer

Radiation is an important way of heat transfer when temperature is high. This phenomenon can happen in flames, especially flames with small particles or soot. Since in this study the effects of radiative heat transfer are not included, the related models were not explained in the computational modeling chapter. ANSYS Fluent offers different radiative heat transfer models for different situations. Discrete Ordinates (DO) and P1 approximation (P1) radiation models are two famous models that may be applied to this case.

As a brief description, for both models, the radiative transfer equation (RTE) must be solved. This equation describes the augmentation and attenuation of a ray when it passes through a medium. Augmentation can occur through absorption while attenuation occurs through emission. Scattering can both attenuate or augment the ray.

In the P1 model, it is assumed that the medium is isotropic, so at the end, only one partial differential equation is solved. This makes the model very simple and computationally efficient. On the other hand, DO model provides a more sophisticated approach and discretizes the medium around each cell into small solid angles. Then, it transforms the radiative transfer equation into a transport equation. For each discretized solid angle, a transport equation will be solved. Therefore, as the number of discretization increases, the DO model is more computationally expensive. Further information regarding these models can be found in “Radiative Heat Transfer” by Modest (2013).

The weighted-sum-of-gray-gases model (WSGGM) is used to calculate the absorption coefficients for both radiation models. Moreover, it is necessary to specify the number of discretization around each spatial location for the DO model, so 25 solid angles are used for this discretization.

In this section, these two models are activated in addition to other models. Since radiation is only a heat loss/gain for a cell, its effects on other variable except temperature is negligible, and the corresponding temperature profile to each model is shown in figure (3.28).

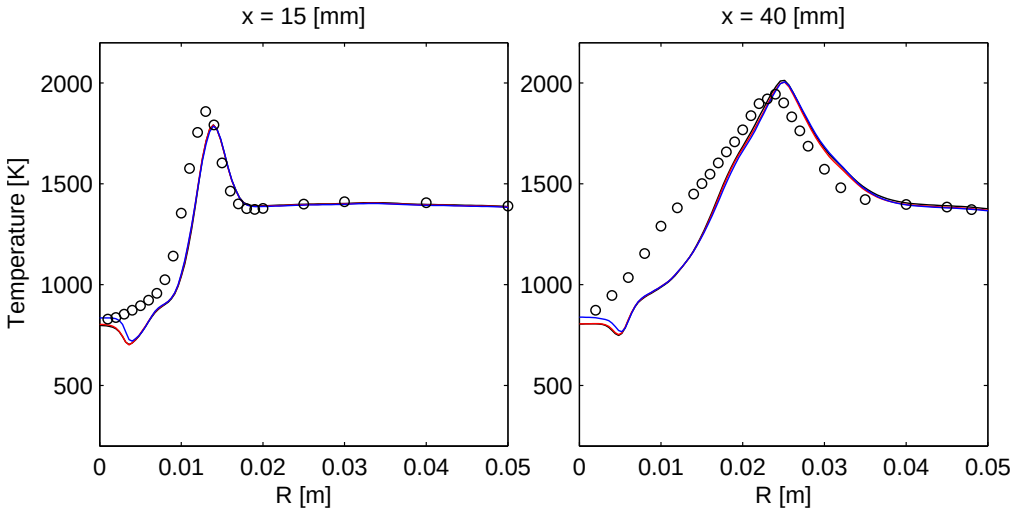

Figure 3.28: Gas-phase temperature (SHCiii). Symbols: experiment, black line: without radiation, red line: P1 approximation model, and blue line: Discrete Ordinates model

According to the results, the deviation from the temperature profile of inactivated radiation is small. The significant difference is only visible in the region near the axis where the DO model predicts better. However, it should be noted that when the DO model is activated, one transport equation is added to the set of equation for each additional solid angle. This means that for this simulation, 25 additional transport equations were solved. This number of solid angles increases the computational time immensely. Since no tangible improvement have been observed, it is not necessary to consider radiation in this study .

The reason why radiation is of little importance in this flame can be traced back to the mixture in the domain. Two main species that can contribute to radiation are carbon dioxide and water without any soot or luminous particle. Since the flame is small, the absorption coefficient cannot be large enough to cause considerable difference in the flame temperature profile; therefore, radiation can be ignored without any prohibitive loss of accuracy. The effect of radiation would be significant if there was soot in the flame, or the domain was vast.

3.3.5 General Conclusion

This section discussed the importance of some options and models in the hot-diluted coflow case. It was concluded that if it is possible, the turbulent two-way coupling between the phases should be considered.

On the other hand, it was shown that radiative heat transfer, buoyancy, and secondary atomization as well as coalescence do not play important roles in this specific case that the flame and the domain are small.

3.4 Model Validation in the Cold Colfow Case

The section is devoted to comparison of the experimental data and the predicted numerical simulation for the cold coflow. The model configuration was explained in section (3.1.2.1). Similar to the hot-diluted coflow case, the results for different turbulence and combustion models are compared under similar spray conditions. The validation process is split into two parts; in the first part, the steady flamelet model will be validated with three turbulence models; likewise, the FGM will be validated in the second part.

Similar to the hot-diluted coflow case, the cold coflow case experimental data are available for a wide range of elevations. For both temperature and velocity profiles, the comparison between numerical and experimental results will be carried out at elevations of 20 mm and 45 mm above the injector.

3.4.1 Steady Flamelet Model

Similar to the hot-diluted coflow case, the results for the steady flamelet model in combination with different turbulence models are compared based on the velocity components and temperature profiles.

Figures (3.29) and (3.30) show the axial and radial velocities for two different elevations. The models overpredict the axial velocity, and they underpredict the radial velocity.

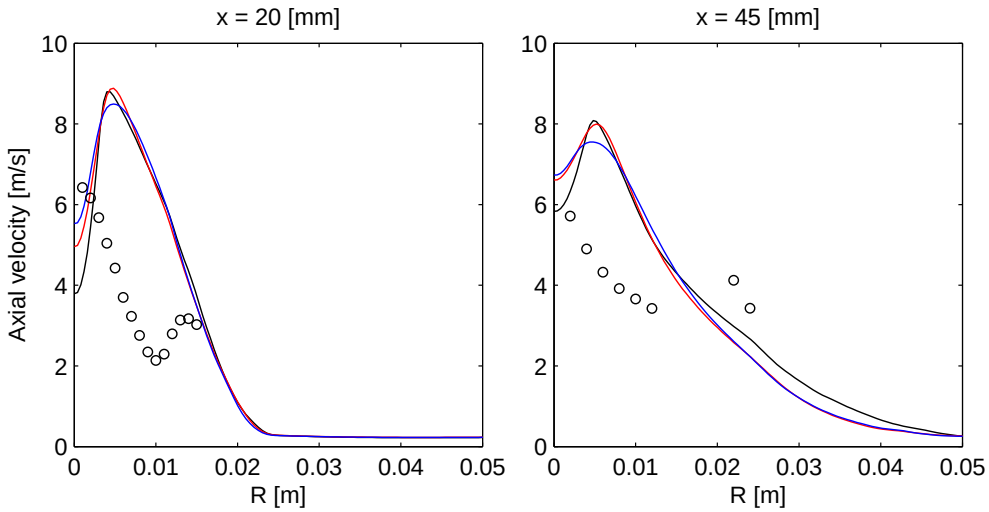

Figure 3.29: Gas-phase axial velocity for the steady flamelet model (SCCii). Symbols: experiment, black line: Reynolds stress model, red line: standard k-ε, and blue line: realizable k-ε

When temperature profiles in figure (3.31) are compared, a large discrepancy between experimental and numerical results are observed. For the elevation of 20 mm, the temperature near the axis is overpredicted up to 500 K while the peak temperature is captured almost by all the models. At higher elevations (x = 45 mm), the temperature profile is completely different from the experimental data. In experiments, two peak temperatures were observed while the steady flamelet predicts only one peak temperature. Moreover, the problem of the high-temperature profile near the axis remains.

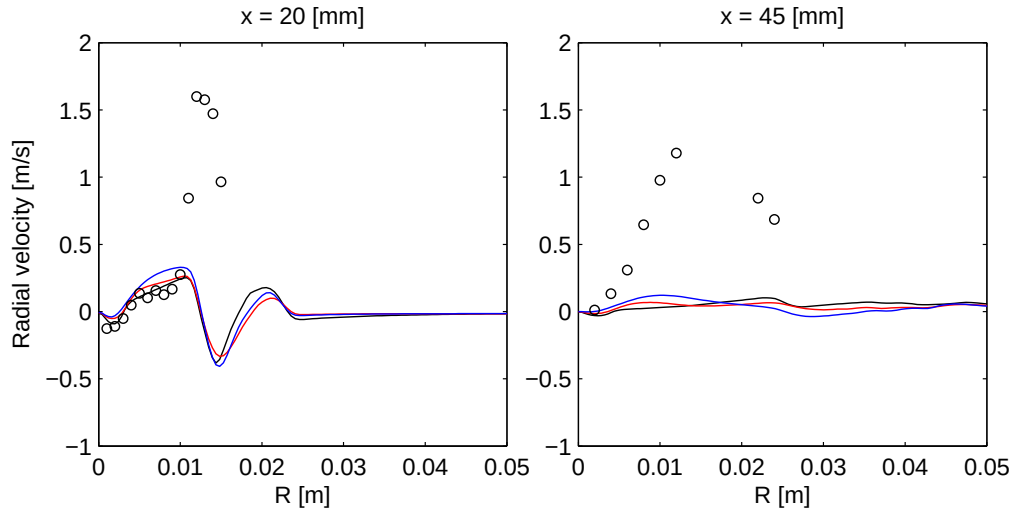

Figure 3.30: Gas-phase radial velocity for the steady flamelet model (SCCii). Symbols: experiment, black line: Reynolds stress model, red line: standard k-ε, and blue line: realizable k-ε

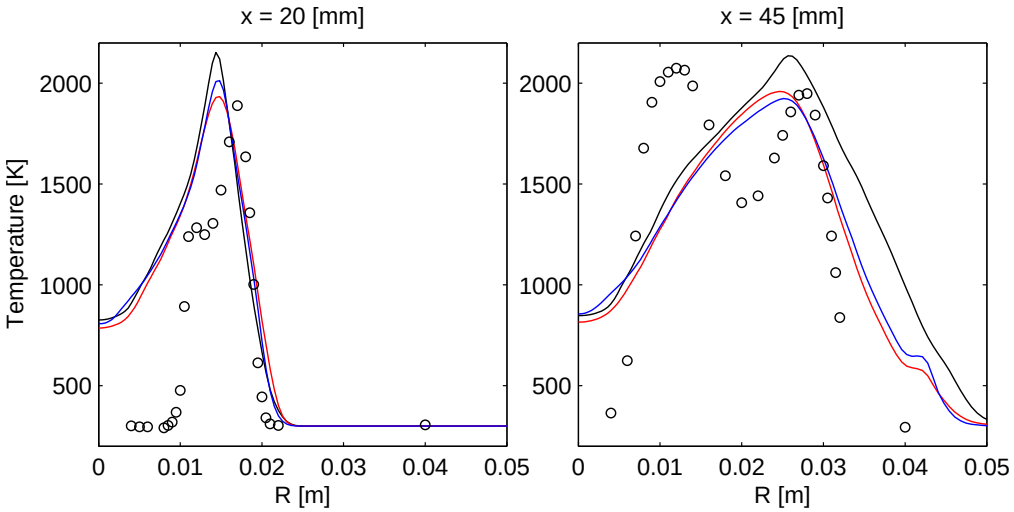

Figure 3.31: Gas-phase temperature for the steady flamelet model (SCCii). Symbols: experiment, black line: Reynolds stress model, red line: standard k-ε, and blue line: realizable k-ε

According to the temperature profiles at two elevations, the steady flamelet can only predict one peak temperature, which is related to the diffusion of the oxidizer to the fuel side. The inside of the flame, where the premixed oxidizer and fuel burns, does not show the second peak temperature.

These differences may be rooted in the fundamental assumption of "mixed is burnt" for the steady flamelet model. Therefore, whenever sufficient fuel is evaporated and mixed with the oxidizer, the mixture will burn. This causes the attached flame while a lift-off of at least 10 mm was observed during the experiments (figure (1.3)). Since the temperature is predicted higher than the real condition, the evaporation would be overpredicted and all droplets would evaporate faster, and a zone near the injection with rich mixture would form. Because of the highly rich mixture near the axis, the oxidizer with low momentum can only diffuse into this zone and burn as non-premixed combustion; still, in the experience the entrained oxidizer will penetrate into this zone and mix before burning inside the flame which brings about the second peak temperature. Thus, the "mixed is burnt" assumption would completely change the real phenomena in the case of cold coflow.

When the axial and radial velocities as well as temperature of the cold coflow case are compared with the results of the hot-diluted coflow case for the steady flamelet model (figures (3.9), (3.10), and (3.12)), it can be seen that the profiles are similar in the vicinity of the axis where the flame is far from the effects of the hot-diluted coflow case (instead of the cold coflow case with its low velocity and temperature boundary conditions). This is because of the assumption mentioned in previous paragraph and its consequences which cause a highly rich mixture near the axis and injector. Even though the boundary conditions and the flamelet table are different, the steady flamelet model predicts similar structure for both cases.

3.4.2 Flamelet Generated Manifold Model

When the steady flamelet model is considered, as long as the evaporated fuel and the oxidizer are mixed, the mixture burns because of "mixed is burnt" assumption. This is not the case for the FGM model. It is possible that a mixture of fuel and oxidizer does not burn. Although there is no necessary additional task to ignite the mixture in the steady flamelet model, it is important to impose an initial value for the progress variable into the domain for the FGM model, so the mixture starts burning. In the hot-diluted coflow case auto-ignition occurs when the evaporated fuel mixes with the hot oxidizer while more efforts are needed to ignite the mixture in the case of cold coflow. In what follows, a brief description of how to start the ignition for the cold coflow case using the FGM model in ANSYS Fluent is given. Then, three turbulence models in combination with the FGM model will be validated.

The procedure used to ignite the mixture for the FGM model consists of three main steps as follows:

1. When the gas-phase velocity in the whole domain is very small, one discrete phase iteration has to be done with the under-relaxation factor of unity. Because of the small gas-phase velocity everywhere, the droplet Reynolds number (equation (2.30)) reaches its maximum value because of the maximum velocity difference between two phases. This directly affects both the mass and heat transfer. In spite of the fact that the temperature is below the boiling temperature, a great portion of droplets will evaporate, and all the evaporated mass will be transferred to the gas-phase calculations.
2. Before the next discrete phase model iteration, the gas-phase solution should be converged for the cold condition without any ignition.

3. After reaching a reasonable cold gas-phase solution, the progress variable of unity have to be patched in a small zone in the domain. It does not matter where the progress variable is set since the gas-phase equations need to be solved for a large number of iteration to converge to a solution for the current discrete phase.

After the last step, the initial condition required for starting the two-phase flow solution is ready; hence, discrete phase equations can be added again to the set of equations. The solution can continue until residuals of equations are below the required threshold for convergence.

The axial and radial velocities for three turbulence models are shown in figures (3.32) and (3.33).

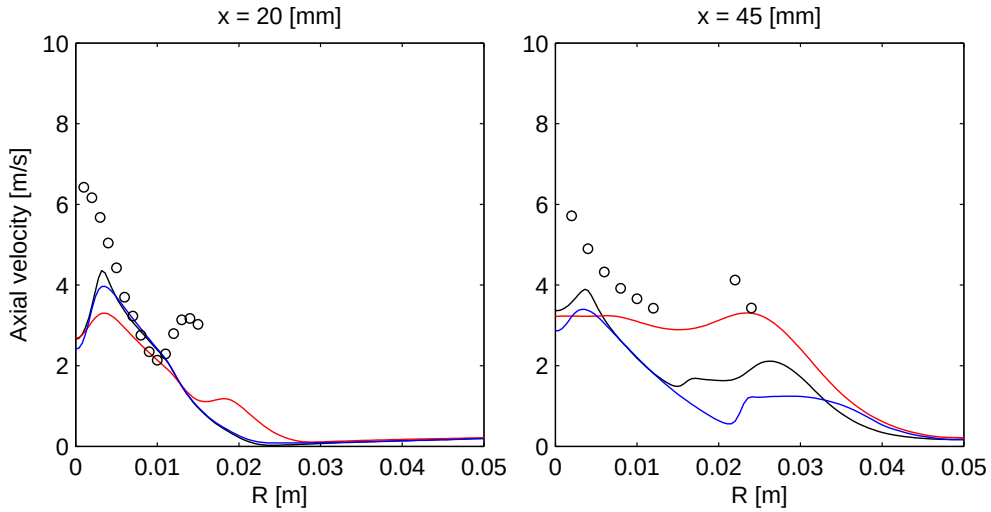

Figure 3.32: Axial velocity for the FGM model (SCCii). Symbols: experiment, black line: Reynolds stress model, red line: standard k-ε, and blue line: realizable k-ε

Similar to the hot-diluted coflow case, the maximum axial velocity at the elevations of 20 mm and 45 mm could not be reached by any of the turbulence models. Moreover, the experimental axial velocity does not monotonically decrease over the radial position, but there is a minimum at the radial positions of 10 mm and 15 mm at the elevations of 20 mm and 45 mm, respectively. The only turbulence model that shows this change at the lower elevation is the standard k-ε model; notwithstanding, all the models show the change at the higher elevation, but the standard k-ε model could only give the best result.

The radial velocity profiles are also different from the hot-diluted coflow case profiles. The k-ε model shows the best performance for predicting the shape of profiles at both elevations although the maximum values are not completely accurate. In these figures, the Reynolds stress and realizable k-ε models could not predict well the shape of axial and radial velocity profiles at 20 mm elevation.

Figure (3.34) depicts the temperature profiles. Almost none of the models could capture the correct trend as well as the maximum temperature. In contrast to the steady flamelet model, the FGM model can predict two-peak temperature profiles.

If the temperature can be a good representative of the lift-off, the standard k-ε predicts the best lift-off. According to the results of the axial and radial velocities, it seems that there is a strong relation between predicting the correct lift-off and other variables such as velocity components or the flame location.

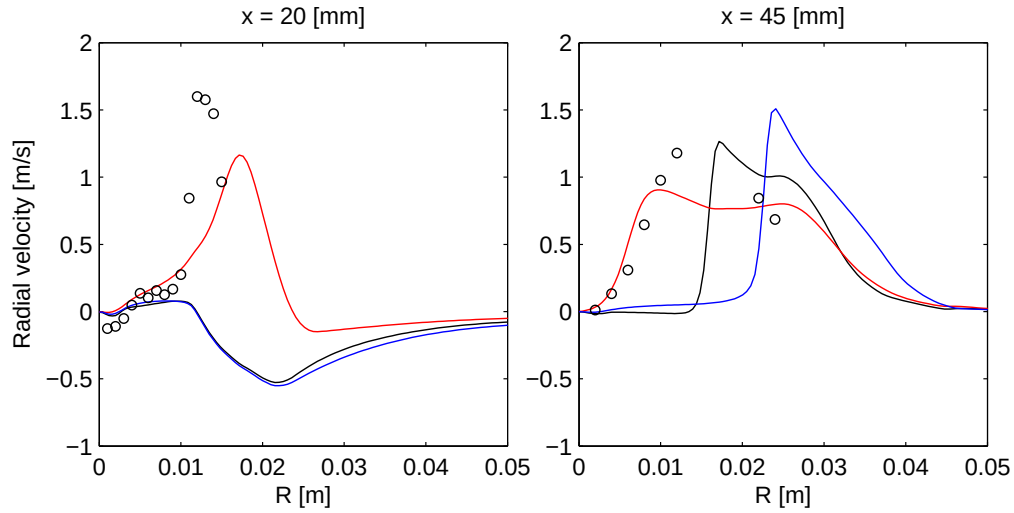

Figure 3.33: Gas-phase radial velocity for the FGM model (SCCii). Symbols: experiment, black line: Reynolds stress model, red line: standard k-ε, and blue line: realizable k-ε

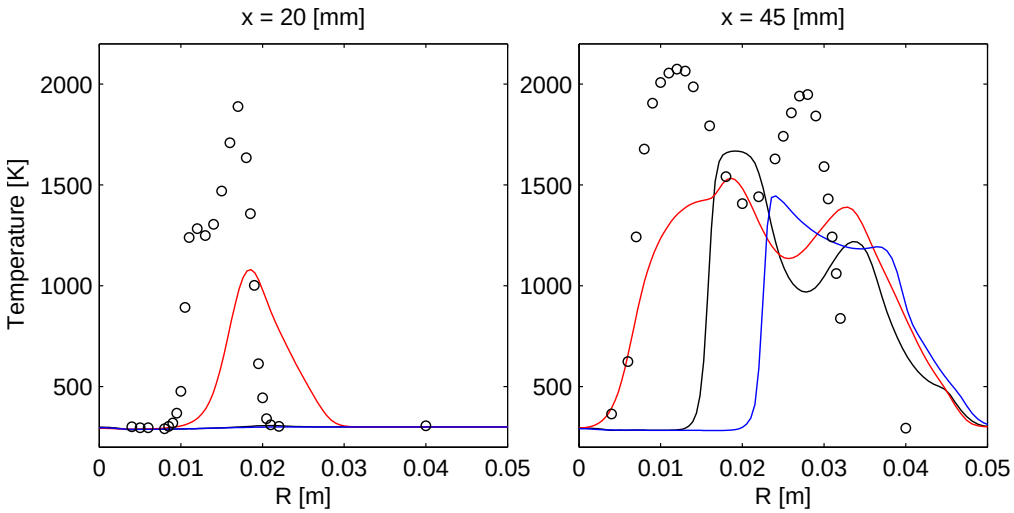

Figure 3.34: Gas-phase temperature for the FGM model (SCCii). Symbols: experiment, black line: Reynolds stress model, red line: standard k-ε , and blue line: realizable k-ε

The correct lift-off means the correct prediction of the location where temperature increases significantly. This high temperature provides the necessary heat for fast evaporation of droplets, so this is an interrelation between the lift-off, turbulence model, and the evaporation model. If the lift-off is correctly predicted by a model, the velocity and temperature profiles will be obtained more accurately as the standard k-ε model could predict the correct profiles. However, this argument concerns the shape of profiles; for instance, the standard k-ε model could not predict the value of the maximum temperature correctly. This can be connected to the progress variable (figure (3.35)). Accordingly, the progress variable never reaches one, showing incomplete combustion. However, this cannot be the only answer because it is the combination of the progress variable and the mixture fraction that gives the temperature for a point.

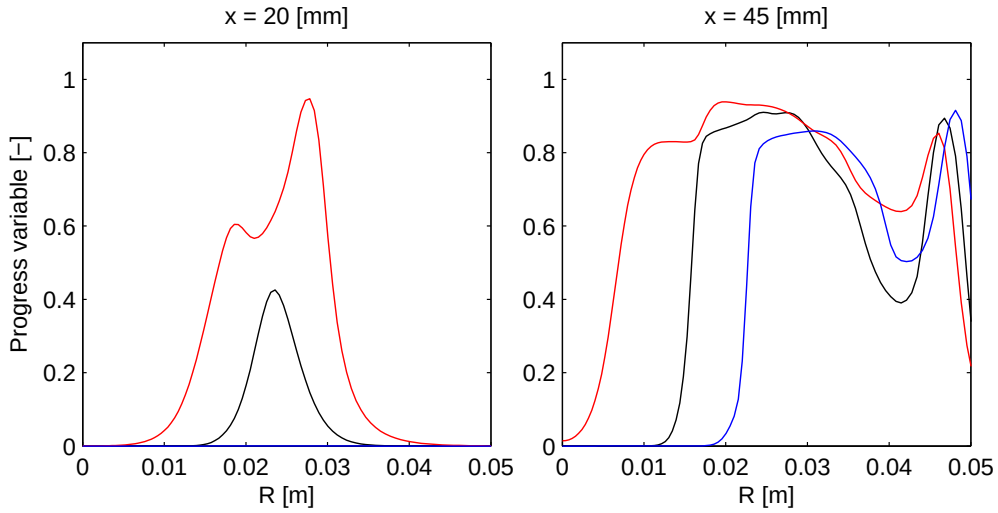

Figure 3.35: Progress variable for the FGM model (SCCii). Black line: Reynolds stress model, red line: standard k-ε, and blue line: realizable k-ε

In order to clarify the problem, the other important parameter for assigning the temperature in the FGM model should be investigated; the mixture fraction for two elevations is shown in figure (3.36). At the elevation of 45 mm, the points where the mixture fraction is equal to the stoichiometric mixture fraction ($Z_{st} = 0.111$) correspond to the points where the progress variable becomes comparatively small, explaining why the turbulence models underpredict the peak temperatures.

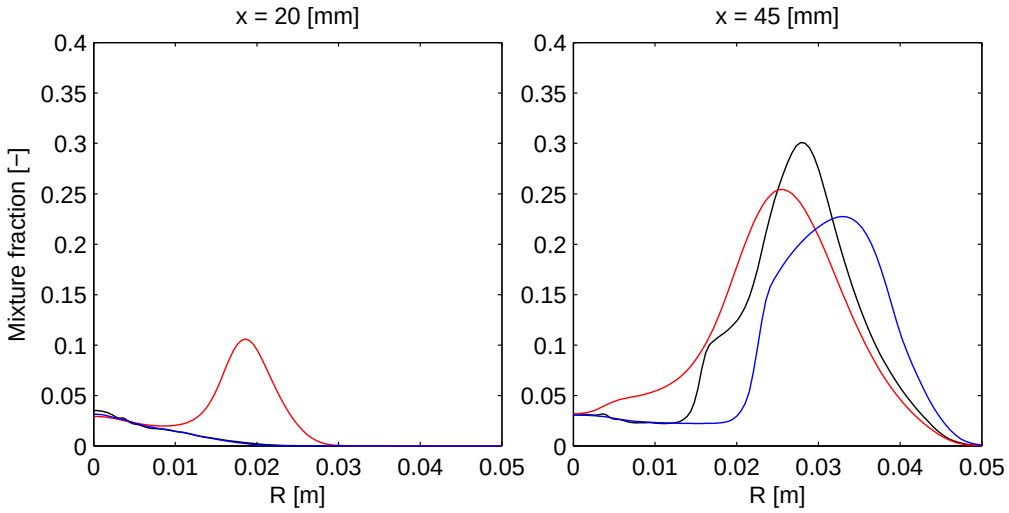

Figure 3.36: Mixture fraction for the FGM model (SCCii). Black line: Reynolds stress model, red line: standard k-ε, and blue line: realizable k-ε

The reason why the maximum temperature cannot be obtained through the FGM model may be related to different factors. Similar to the hot-diluted coflow case, the FGM table can be the cause of this discrepancy; furthermore, the complete two-way coupling which considers the turbulence as well as another important factor. The evaporation model is highly important as described for the ethanol combustion in a gas turbine combustion chamber by (Sadiki, Ahmadi, Chrigui & Janicka 2011) and (Sadiki, Ahmadi & Chrigui 2011).

3.4.3 General Conclusion

In general, the results from the steady flamelet model show large discrepancy in the experimental data. This is because of the attached flame to the injector. Hence, the evaporation rate is predicted based on a faster rate, so the heat release is not predicted correctly. It should be mentioned that the steady flamelet model along with the Reynolds stress model could predict the maximum temperature which is not the case for the FGM model with any turbulence models.

The FGM model, on the other hand, can predict well most of the details observed in the experimental results. Turbulence models also may affect the results. Accordingly, the best turbulence model was identified to be the standard k-ε model, which predicts lift-off correctly. Based on the correct prediction of the lift-off height, evaporation rate as well as all the variables are obtained in better agreement with the experimental data.

Still, the maximum temperature and velocities were captured by none of the turbulence models; as mentioned, it is not possible to find just a model or option that is responsible for inaccurate results, but the combination of different models causes the discrepancy. For instance, the simple evaporation model, the FGM table, the lack of turbulent two-way coupling, inaccurate atomization model may result in inaccurate numerical results. Still, effects of the evaporation model have been shown to be the most important factor to define the correct coupling of heat and mass between two phases, as well as the correct prediction of evaporated fuel (Sadiki, Ahmadi, Chrigui & Janicka 2011), (Sadiki, Ahmadi & Chrigui 2011), (Chrigui et al. 2012), and (Olguin & Gutheil 2014).

When comparing the cold coflow flame structure (figure (3.37)) with the hot-diluted coflow flame structure (figure (3.19)), the similarity of the predicted flame structure by the steady flamelet model for both cases is evident. Because of the high temperature of the attached flame, evaporation is overpredicted; therefore, a highly rich region near the axis forms where obtaining the peak temperature near the axis is not possible. Because of the attached flame, the temperature of the coflow has negligible effect on the evaporation rate of the steady flamelet model.

On the contrary, the FGM model provides a better description of the flame structure. In the hot-diluted coflow case, because of the high momentum of the hot-diluted coflow and its low oxygen content, the main reaction occurs in a region far from the axis, and the oxygen is low enough that no further oxygen is available to penetrate inside the flame to be burnt. However, in the cold coflow case, firstly the axial velocity of the coflow is approximately ten times less; secondly, the oxygen mass fraction is almost three times the hot-diluted coflow oxygen mass fraction, so it is possible that oxygen molecules penetrate into the evaporated fuel in the vicinity of the axis and form a premixed region plus the non-premixed region in the outer layer. Hence, as it can be seen from figure (3.37), there are two main regions where reactions occur and almost half of the reaction occurs inside the flame as premixed combustion.

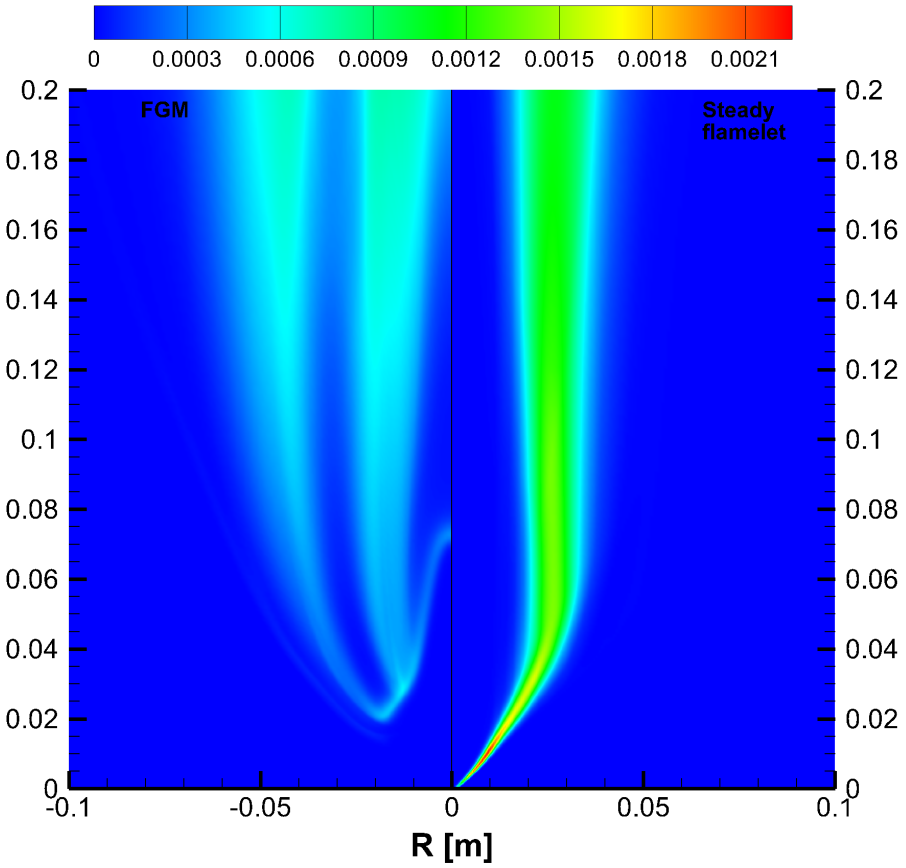

Figure 3.37: OH mass fraction contour for the cold coflow case. Left: the FGM model, right: the steady flamelet model

Chapter 4

Conclusion and Recommendations

The combination of different combustion models as well as turbulence models for modeling turbulent spray flames has been studied. A standard Lagrangian spray model was used for droplet evolution. Although the spray model is an important factor and its effects are visible on the flame structure, it was used unchanged through the simulations. The combination of the steady flamelet or FGM models along with the Reynolds stress or k-ε models were the focus for two different cases of the hot-diluted coflow as well as the cold coflow in order to simulate the situation in a flameless burner and a conventional burner, respectively. These numerical results have been compared with the available experimental data of the Delft Spray-in-Hot-Coflow burner.

For the first case known as SHCiii in which the oxidizer is the hot-diluted coflow, there is good agreement between the numerical and experimental results of the steady flamelet model in combination with almost all of the turbulence models. Also, the FGM model showed that it can predict acceptably the temperature and velocity profiles for the Reynolds stress and realizable k-ε models while the standard k-ε model underpredicts peak temperatures in a similar situation for the other turbulence models, but this underprediction can be remediated considerably by coupling turbulence between the gas and discrete phases.

The second case representing the conventional burners with the cold coflow (Case SCCii) was a more challenging case. Because of the different coflow boundary condition, the structure of the flame is completely different as a result of different evaporation, ignition, and other phenomena. Since the steady flamelet model is based on the "mixed is burnt" assumption, the flame is attached to the injector, so the evaporation rate deviates significantly from the reality, and this wrong evaporation rate makes a fuel-rich zone near the axis, where the oxidizer cannot mix with the fuel; therefore, the temperature profile as well as axial and radial velocities show large discrepancy between the numerical and experimental results. The performance of turbulence model in combination with the steady flamelet model is very similar.

On the other hand, the FGM model shows that it can predict almost all the details and phenomena of the flame because of predicting similar temperature and velocity profiles to the experiment; however, how good the FGM model can predict all the details is related to the combination of injection, evaporation, and turbulence models as well as complete two-way coupling between the phases. According to previous studies, the evaporation model is of outstanding importance, but it is not possible to isolate the effects of a single sub-model. Any changes in one model may cause a sequence of changes that affect other models and numerical results as well. Nonetheless, it can firmly be concluded that the lift-off height should be correctly predicted in order to observe acceptable results.

In addition to the basic combination of models, there are some options and models that may or may not improve the results of the hot-diluted coflow case. As mentioned, complete two-way coupling (mass, momentum, heat, and turbulence) between the phases can affect almost all the variables like temperature and velocities. Also, it was observed that the flamelet and FGM tables may affect the results although a detailed comparison has not been done yet. On the contrary, the effects of the radiative heat transfer, the buoyancy force, and secondary atomization as well as coalescence are negligible only in this specific case for the hot-diluted coflow case. The first two ones may be ignored in small flames with little loss of accuracy. The last two phenomena are negligible as long as the dense regime covers a very small region in the domain.

Moreover, the evaporation model is an important factor that can change the structure of the flame completely. Next, the correct coupling between the gas and discrete phase can play an important role. FGM tables are also important for correct prediction of the flame. All of the mentioned parameters and models are important factors in correct prediction of flame. They are interrelated to each other, and each one can affect the performance of the others in the prediction of the flame structure. Therefore, they must be carefully chosen.

According to the evaporation rate, the effect of lift-off can be explained for the FGM model. In the hot-diluted coflow case, droplets are mainly evaporated by the hot-diluted coflow similar to the steady flamelet where the lift-off height does not change the evaporation rate significantly; however, in the cold coflow case, the evaporation rate relies mainly on the lift-off height, where the temperature is high enough to provide the necessary energy for evaporation. Out of this region, the evaporation rate is very little.

The conclusion of this study is that the FGM model is superior to the steady flamelet model in the case of better prediction of flame structure while the steady flamelet is capable of achieving the peak temperatures; moreover, the turbulence models do not make significant changes in the flame structure and their performances are approximately the same, but it was observed that the Reynolds stress and realizable k-ε models show similar temperature and velocity profiles while the standard k-ε model gives different results.

The NO_x formation in the hot-diluted coflow case was not studied through numerical simulation in this study since no experimental data is available to validate the simulation; however, from other studies like the work of Wünning & Wünning (1997), it can be deduced that the low temperatures in the flameless burners can suppress thermal NO_x formation. Furthermore, Correia Rodrigues et al. (2014) observed that few temperature samples trespass the temperature threshold that cause thermal NO_x in the hot-diluted coflow case, so the only conclusion is that flameless combustion may reduce the thermal NO_x formation, and no further conclusion can be drawn about the formation of prompt NO_x or the nitrous oxide.

Finally, some recommendations are given for the future studies:

- FGM tables can be generated from different boundary conditions, different definition of the progress variable, or different formulation, all of which are based on assumptions on local flame structure. Then, the effect of each of these parameters can be investigated.
- Based on correct temperature and species mass fractions, the thermal and prompt NO_x formation as well as NO_x formation from nitrous oxide can be studied and the importance of each mechanism in the flameless combustion can be identified.
- More complicated and accurate evaporation models that consider the temperature gradients or internal circulation in the droplet are suggested to be used. As shown by different studies such as (Rochaya 2007) and (Chrigui et al. 2012) as well as this study, the evaporation rate can cause significant difference in the final result.
- As an alternative to the RANS approach used in the current study, it could be worthwhile to use LES instead. The advantage of LES is that it predicts the transient evolution of the large scale slow pattern and therefore can give a better prediction of the mixing of fuel and oxidizer, which can be essential for prediction of flame structure. This recommendation can only be followed if sufficient computational resources are available.

Chapter 5

Bibliography

ANSYS (2013), 'ANSYS FLUENT Theory Guide'.

Bray, K., Domingo, P. & Vervisch, L. (2005), 'Role of the progress variable in models for partially premixed turbulent combustion', *Combustion and Flame* **141**(4), 431–437.
URL: *http://www.sciencedirect.com/science/article/pii/S0010218005000520*

Chrigui, M., Gounder, J., Sadiki, A., Masri, A. R. & Janicka, J. (2012), 'Partially premixed reacting acetone spray using LES and FGM tabulated chemistry', *Combustion and Flame* **159**(8), 2718–2741.
URL: *http://linkinghub.elsevier.com/retrieve/pii/S0010218012000971*

Correia Rodrigues, H., Tummers, M., van Veen, E. & Roekaerts, D. (2014), 'Spray flame structure in conventional and hot-diluted combustion regime', *Combustion and Flame* (in press).

Danon, B. (2011), Furnaces with multiple ameless combustion burners, PhD thesis, Delft University of Technology.
URL: *http://repository.tudelft.nl/view/ir/uuid:abab2e18-db5e-4447-bb88-e990d163b352/*

de Goey, L. P. H., van Oijen, J. A. & Roekaerts, D. (2010), Lecture notes of the J. M. Burgerscentrum Courses on Combustion, Technical report, University of Eindhoven, Eindhoven.

Dixon-Lewis, G. (1991), Structure of laminar flames, *in* 'Symposium (International) on Combustion', pp. 305–324.
URL: *http://www.sciencedirect.com/science/article/pii/S0082078406802742*

Dombrowski, N. & Hooper, P. (1962), 'The effect of ambient density on drop formation in sprays', *Chemical Engineering Science* **17**(4), 291–305.
URL: *http://linkinghub.elsevier.com/retrieve/pii/0009250962850088*

Gutheil, E. (2011), Issues in Computational Studies of Turbulent Spray Combustion, *in* B. Merci, D. Roekaerts & A. Sadiki, eds, 'Experiments and Numerical Simulations of Diluted Spray Turbulent Combustion SE - 1', Vol. 17 of *ERCOFTAC Series*, Springer Netherlands, pp. 1–39.
URL: *http://dx.doi.org/10.1007/978-94-007-1409-0_1*

Heye, C. R., Kourmatzis, A., Raman, V. & Masri, A. R. (2014), A Comparative Study of the Simulation of Turbulent Ethanol Spray Flames, *in* B. Merci & E. Gutheil, eds, 'Experiments and Numerical Simulations of Turbulent Combustion of Diluted Sprays', Vol. 19, Springer International Publishing, chapter 2, pp. 31–54.
URL: *http://dx.doi.org/10.1007/978-3-319-04678-5_2*

Hollmann, C. & Gutheil, E. (1996), Modeling of turbulent spray diffusion flames including detailed chemistry, *in* 'Symposium (international) on combustion', pp. 1731–1738.
URL: *http://www.sciencedirect.com/science/article/pii/S0082078496803985*

Humza, R. M., Hu, Y. & Gutheil, E. (2014), Probability Density Function Modeling of Turbulent Spray Combustion, *in* B. Merci & E. Gutheil, eds, 'Experiments and Numerical Simulations of Turbulent Combustion of Diluted Sprays SE - 6', Vol. 19 of *ERCOFTAC Series*, Springer International Publishing, pp. 129–153.
URL: *http://dx.doi.org/10.1007/978-3-319-04678-5_6*

Jenny, P., Roekaerts, D. & Beishuizen, N. (2012), 'Modeling of turbulent dilute spray combustion', *Progress in Energy and Combustion Science* **38**(6), 846–887.
URL: *http://linkinghub.elsevier.com/retrieve/pii/S0360128512000445*

Luo, K., Fan, J. & Cen, K. (2013), 'New spray flamelet equations considering evaporation effects in the mixture fraction space', *Fuel* **103**, 1154–1157.
URL: *http://linkinghub.elsevier.com/retrieve/pii/S0016236112004802*

Ma, L., Correia Rodrigues, H. R., Naud, B., Tummers, M. J. & Roekaerts, D. J. E. M. (2014), Modeling spray jet flame in hot-diluted coflow with transported PDF, *in* 'Journées dEtude of the Belgian Section of the Combustion Institute', pp. 1–2.

Ma, L., Zhu, S., Rodrigues, H., Tummers, M., van der Meer, T. & Roerkaerts, D. (2013), Numerical Investigation of Ethanol Spray-in-Hot-Cofloe Flame Using Steady Flamelet Model, *in* '8th Mediterranean Combustion Symposium', Izmir, Turkey.

Marinov, N. M. (1999), 'A detailed chemical kinetic model for high temperature ethanol oxidation', *International Journal of Chemical Kinetics* **31**(3), 183–220.

Modest, M. F. (2013), *Radiative Heat Transfer*, 3rd edn, Academic Press.

Müller, C. M., Breitbach, H. & Peters, N. (1994), 'Partially premixed turbulent flame propagation in jet flames', *Symposium (International) on Combustion* **25**(1), 1099–1106.
URL: *http://www.sciencedirect.com/science/article/pii/S0082078406807472*

Müller, H., Ferraro, F. & Pfitzner, M. (2013), Implementation of a Steady Laminar Flamelet Model for non-premixed combustion in LES and RANS simulations, *in* '8th International OpenFOAM Workshop', Jeju, Korea.

Okuyama, M., Hirano, S., Ogami, Y., Nakamura, H., Ju, Y. & Kobayashi, H. (2010), 'Development of an Ethanol Reduced Kinetic Mechanism Based on the Quasi-Steady State Assumption and Feasibility Evaluation for Multi-Dimensional Flame Analysis', *Journal of Thermal Science and Technology* **5**(2), 189–199.
URL: *http://joi.jlc.jst.go.jp/JST.JSTAGE/jtst/5.189?from=CrossRef*

Olguin, H. & Gutheil, E. (2014), 'Influence of evaporation on spray flamelet structures', *Combustion and Flame* **161**(4), 987–996.
URL: *http://linkinghub.elsevier.com/retrieve/pii/S0010218013003842*

Peters, N. (1984), 'Laminar diffusion flamelet models in non-premixed turbulent combustion', *Progress in Energy and Combustion Science* **10**(3), 319–339.
URL: *http://www.sciencedirect.com/science/article/pii/036012858490114X*

Peters, N. (1986), Laminar flamelet concepts in turbulent combustion, *in* 'Symposium (International) on Combustion', Vol. 21, pp. 1231–1250.
URL: *http://www.sciencedirect.com/science/article/pii/S0082078488803552*

Pitsch, H., Chen, M. & Peters, N. (1998), 'Unsteady flamelet modeling of turbulent hydrogen-air diffusion flames', *Symposium (International) on Combustion* **27**(1), 1057–1064.
URL: *http://www.sciencedirect.com/science/article/pii/S0082078498805067*

Pitsch, H. & Peters, N. (1998), 'A Consistent Flamelet Formulation for Non-Premixed Combustion Considering Differential Diffusion Effects', *Combustion and Flame* **114**(12), 26–40.
URL: *http://www.sciencedirect.com/science/article/pii/S0010218097002782*

Poinsot, T. & Veynante, D. (2011), *Theoretical and numerical combustion*, CNRS, Toulouse.

Pope, S. B. (2000), *Turbulent flows*, Cambridge University Press, Cambridge ; New York.

Rochaya, D. (2007), Numerical simulation of spray combustion using bio-mass derived liquid fuels, PhD thesis, Cranfield.
URL: *https://dspace.lib.cranfield.ac.uk/handle/1826/2231*

Röhl, O. & Peters, N. (2009), A reduced mechanism for ethanol oxidation, *in* '4th European Combustion Meeting (ECM 2009)', pp. 1–5.
URL: *http://combustion.org.uk/ECM_2009/P810336.pdf*

Sadiki, A., Ahmadi, W. & Chrigui, M. (2011), Toward the Impact of Fuel Evaporation-Combustion Interaction on Spray Combustion in Gas Turbine Combustion Chambers. Part II: Influence of High Combustion Temperature on Spray Droplet Evaporation, *in* B. Merci, D. Roekaerts & A. Sadiki, eds, 'Experiments and Numerical Simulations of Diluted Spray Turbulent Combustion SE - 4', Vol. 17 of *ERCOFTAC Series*, Springer Netherlands, pp. 111–132.
URL: *http://dx.doi.org/10.1007/978-94-007-1409-0_4*

Sadiki, A., Ahmadi, W., Chrigui, M. & Janicka, J. (2011), Toward the Impact of Fuel Evaporation-Combustion Interaction on Spray Combustion in Gas Turbine Combustion Chambers. Part I: Effect of Partial Fuel Vaporization on Spray Combustion, *in* B. Merci, D. Roekaerts & A. Sadiki, eds, 'Experiments and Numerical Simulations of Diluted Spray Turbulent Combustion SE - 3', Vol. 17 of *ERCOFTAC Series*, Springer Netherlands, pp. 69–110.
URL: *http://dx.doi.org/10.1007/978-94-007-1409-0_3*

Saxena, P. & Williams, F. A. (2007), 'Numerical and experimental studies of ethanol flames', *Proceedings of the Combustion Institute* **31**(1), 1149–1156.
URL: *http://linkinghub.elsevier.com/retrieve/pii/S1540748906003609*

van Oijen, J. (2002), Flamelet-generated manifolds: development and application to premixed laminar flames, PhD thesis.

van Oijen, J. A., Lammers, F. A. & de Goey, L. P. H. (2001), 'Modeling of complex premixed burner systems by using flamelet-generated manifolds', *Combustion and Flame* **127**(3), 2124–2134.
URL: *http://www.sciencedirect.com/science/article/pii/S0010218001003169*

van Oijen, J. & de Goey, L. (2000), 'Modelling of Premixed Laminar Flames using Flamelet-Generated Manifolds', *Combustion Science and Technology* **161**(1), 113–137.
URL: *http://www.tandfonline.com/doi/abs/10.1080/00102200008935814*

Warnatz, J., Maas, U. & Dibble, R. W. (2006), *Combustion : physical and chemical fundamentals, modeling and simulation, experiments, pollutant formation*, 4th edn, Springer, Berlin ; New York.

Weber, R., Smart, J. P. & Kamp, W. V. (2005), 'On the (MILD) combustion of gaseous, liquid, and solid fuels in high temperature preheated air', *Proceedings of the Combustion Institute* **30**(2), 2623–2629.
URL: *http://linkinghub.elsevier.com/retrieve/pii/S0082078404001547*

Wünning, J. (2003), FLOX-Flameless Combustion, *in* 'Thermprocess Symposium'.

Wünning, J. & Wünning, J. (1997), 'Flameless oxidation to reduce thermal NO-formation', *Progress in energy and combustion science* **23**, 81–94.
URL: *http://www.sciencedirect.com/science/article/pii/S0360128597000063*

Appendices

Appendix A

The Flamelet and FGM Tables

As an illustration, a part from the generated tables by the steady flamelet and FGM models are given in the following sections. The chemical mechanism as well as the thermodynamic properties to generate the flamelet and FGM tables can be found from the the work of Röhl & Peters (2009).

A.1 The Steady Flamelet Table

A flamelet, which its scalar dissipation rate is 16.0, is shown below. As mentioned, each flamelet stores the data of temperature and species mass fractions. As it can been seen, for a specific scalar dissipation rate, there are 41 points on the mixture fraction axis from 0 to 1, and the corresponding temperatures and species mass fractions are stored as well. Since the table is huge, only part of the species are shown.

```
HEADER
CHI 1.600000E+01
NUMOFSPECIES 38
GRIDPOINTS 41
PRESSURE 1.013250E+05
BODY
Z
0.000000000E+00 8.911431135E-03 1.635090853E-02 2.256156348E-02 2.774636785E-02
3.207476744E-02 3.568821970E-02 3.870481669E-02 4.122314453E-02 4.425451279E-02
4.788565891E-02 5.223525323E-02 5.744544586E-02 6.056597908E-02 6.368651231E-02
6.742446532E-02 7.116241833E-02 8.011748577E-02 9.084437726E-02 1.036936608E-01
1.190852670E-01 1.375222123E-01 1.596070390E-01 1.860615064E-01 2.177501791E-01
2.557086820E-01 3.011775459E-01 3.556427493E-01 4.208842823E-01 4.599593004E-01
4.990343185E-01 5.926468976E-01 6.487141459E-01 6.767477700E-01 6.907645821E-01
6.977729881E-01 7.047813941E-01 7.719419479E-01 8.391025018E-01 9.195512509E-01
1.000000000E+00
TEMPERATURE
1.360000000E+03 1.472693164E+03 1.551388302E+03 1.608509924E+03 1.651182504E+03
1.683750238E+03 1.709004722E+03 1.728806691E+03 1.744438927E+03 1.762100763E+03
1.781334065E+03 1.800835579E+03 1.817385379E+03 1.822991642E+03 1.825365902E+03
1.824285013E+03 1.819643242E+03 1.797284375E+03 1.760581225E+03 1.712316734E+03
1.655413346E+03 1.592596616E+03 1.525909602E+03 1.456058536E+03 1.382517124E+03
```

1.304087787E+03 1.219456108E+03 1.127767827E+03 1.028715293E+03 9.736649733E+02
9.212995563E+02 8.052300776E+02 7.403177864E+02 7.088859586E+02 6.933891137E+02
6.856903556E+02 6.780228999E+02 6.060370091E+02 5.345540422E+02 4.462374575E+02
3.500000000E+02
massfraction-h2
0.000000000E+00 7.458445738E-05 1.686692075E-04 2.690397681E-04 3.694571565E-04
4.668044334E-04 5.595658573E-04 6.468564882E-04 7.279558568E-04 8.369889919E-04
9.862134857E-04 1.193342800E-03 1.477659780E-03 1.658687777E-03 1.843504311E-03
2.064828721E-03 2.281035430E-03 2.762970556E-03 3.256054801E-03 3.740282943E-03
4.203848391E-03 4.619055137E-03 4.937766033E-03 5.114476060E-03 5.130372766E-03
4.998348747E-03 4.747039364E-03 4.398443820E-03 3.959116892E-03 3.692921099E-03
3.425861326E-03 2.785178078E-03 2.401656676E-03 2.209939545E-03 2.114089552E-03
2.066166424E-03 2.018244454E-03 1.559069545E-03 1.099924107E-03 5.499532910E-04
0.000000000E+00
massfraction-h
0.000000000E+00 2.295295717E-05 6.052641790E-05 9.821906742E-05 1.314676627E-04
1.589088672E-04 1.805585913E-04 1.970317140E-04 2.091660450E-04 2.212239056E-04
2.309045115E-04 2.338253891E-04 2.228874042E-04 2.095629638E-04 1.922184078E-04
1.680836418E-04 1.429285611E-04 8.840965950E-05 4.799776156E-05 2.696748582E-05
1.838541024E-05 1.431546703E-05 1.082119683E-05 7.218292667E-06 4.083340898E-06
1.937368472E-06 8.010859782E-07 3.110723144E-07 1.118238530E-07 5.895088257E-08
3.060872423E-08 7.135858190E-09 3.137689588E-09 2.077099451E-09 1.685905726E-09
1.517215541E-09 1.363721604E-09 4.786673598E-10 1.425777734E-10 2.320318952E-11
0.000000000E+00
massfraction-ch4
0.000000000E+00 9.020270436E-10 4.301407724E-09 1.467878488E-08 4.715995273E-08
1.397066810E-07 3.608033487E-07 7.984652443E-07 1.530094310E-06 3.193255404E-06
7.268750032E-06 1.785474783E-05 4.608260614E-05 7.740471880E-05 1.232217839E-04
2.019587631E-04 3.117942756E-04 7.139811867E-04 1.411320284E-03 2.363588919E-03
3.447196504E-03 4.544960287E-03 5.544793279E-03 6.326340634E-03 6.797506692E-03
6.935486229E-03 6.780833654E-03 6.392562028E-03 5.810107435E-03 5.438000083E-03
5.056180372E-03 4.119495563E-03 3.554362841E-03 3.271258334E-03 3.129614365E-03
3.058773490E-03 2.987921201E-03 2.308430174E-03 1.628682485E-03 8.143443398E-04
0.000000000E+00
massfraction-co2
8.655654851E-02 9.782950685E-02 1.056863730E-01 1.111031162E-01 1.147994630E-01
1.172997592E-01 1.189785022E-01 1.200987583E-01 1.208427110E-01 1.215150888E-01
1.220193220E-01 1.222404861E-01 1.220726052E-01 1.218316348E-01 1.215200305E-01
1.210904533E-01 1.206324901E-01 1.194980952E-01 1.181659457E-01 1.165988424E-01
1.147327131E-01 1.124859646E-01 1.097554676E-01 1.064205327E-01 1.023548595E-01
9.742876372E-02 9.149474171E-02 8.437065783E-02 7.583030182E-02 7.071431586E-02
6.559802039E-02 5.334026814E-02 4.599867184E-02 4.232786353E-02 4.049245756E-02
3.957475419E-02 3.865705057E-02 2.986281645E-02 2.106857191E-02 1.053430130E-02
0.000000000E+00
massfraction-co
0.000000000E+00 3.139380829E-03 6.742937168E-03 1.046813258E-02 1.409102195E-02
1.747385079E-02 2.054120324E-02 2.326052424E-02 2.562814898E-02 2.857344874E-02
3.217995825E-02 3.646536224E-02 4.123303078E-02 4.373352822E-02 4.593913040E-02
4.820236176E-02 5.011119930E-02 5.355159237E-02 5.663486044E-02 5.956037490E-02
6.229303256E-02 6.458459274E-02 6.603178974E-02 6.625894638E-02 6.511558759E-02
6.270137375E-02 5.920302019E-02 5.472034659E-02 4.922364856E-02 4.591335315E-02
4.259683158E-02 3.463979485E-02 2.987261623E-02 2.748885449E-02 2.629694502E-02
2.570098444E-02 2.510502034E-02 1.939382011E-02 1.368254031E-02 6.841229635E-03
0.000000000E+00
massfraction-o2

```
9.894149793E-02 8.082126512E-02 6.684211288E-02 5.597722828E-02 4.750362241E-02
4.087277217E-02 3.567043957E-02 3.158166380E-02 2.836339629E-02 2.474743504E-02
2.083033916E-02 1.680370488E-02 1.300321588E-02 1.122969669E-02 9.789208802E-03
8.430943330E-03 7.378313159E-03 5.765260946E-03 4.569804978E-03 3.552784053E-03
2.606460935E-03 1.728559936E-03 9.855450436E-04 4.621167567E-04 1.774651836E-04
5.875768632E-05 1.793850907E-05 5.300700314E-06 1.684492838E-06 8.614179847E-07
4.489388659E-07 1.565308931E-07 8.632937518E-08 6.446484686E-08 5.579960703E-08
5.193727893E-08 4.836044455E-08 2.725601645E-08 1.413309423E-08 5.030887034E-09
0.000000000E+00
massfraction-o
0.000000000E+00 6.773275907E-04 1.200447723E-03 1.518727193E-03 1.681127450E-03
1.736924888E-03 1.723961381E-03 1.669509065E-03 1.593000768E-03 1.464379253E-03
1.263373332E-03 9.772114203E-04 6.301917296E-04 4.561309413E-04 3.167132213E-04
1.961145678E-04 1.168940132E-04 3.468856358E-05 9.498658204E-06 3.032460025E-06
1.299580685E-06 6.779566492E-07 3.586256435E-07 1.642881284E-07 5.642399751E-08
1.371164121E-08 2.507402238E-09 3.854414707E-10 5.227745390E-11 1.516930919E-11
4.324413854E-12 3.656442357E-13 9.122941788E-14 4.605161607E-14 3.281278394E-14
2.770123170E-14 2.336127841E-14 5.335165767E-15 1.028674832E-15 8.318413884E-17
0.000000000E+00
massfraction-oh
0.000000000E+00 1.272434935E-03 2.052425875E-03 2.619543576E-03 3.014824077E-03
3.272973047E-03 3.425267547E-03 3.498670944E-03 3.516019403E-03 3.477396278E-03
3.337081544E-03 3.032599789E-03 2.511338186E-03 2.167180538E-03 1.824894560E-03
1.443807952E-03 1.114185584E-03 5.591783660E-04 2.418895972E-04 1.068150619E-04
5.889171360E-05 3.995359359E-05 2.844089864E-05 1.862726709E-05 1.032830546E-05
4.690043221E-06 1.786068734E-06 5.972129541E-07 1.725052104E-07 7.857288940E-08
3.496539700E-08 5.596354552E-09 1.692625230E-09 8.194770551E-10 5.530943135E-10
4.515435686E-10 3.671604845E-10 5.560703921E-11 1.326044587E-11 2.110737028E-12
0.000000000E+00
massfraction-h2o
6.996105843E-02 7.823596942E-02 8.484464022E-02 9.015178406E-02 9.445549040E-02
9.796389528E-02 1.008290619E-01 1.031680977E-01 1.050753468E-01 1.073041635E-01
1.098516195E-01 1.126771524E-01 1.156612111E-01 1.172213534E-01 1.186153257E-01
1.200816374E-01 1.213538443E-01 1.237392598E-01 1.258236087E-01 1.277167582E-01
1.294155319E-01 1.306497071E-01 1.309096215E-01 1.296395226E-01 1.264880898E-01
1.214062039E-01 1.144989819E-01 1.058002054E-01 9.517712721E-02 8.878018872E-02
8.237006884E-02 6.698599146E-02 5.776767626E-02 5.315801815E-02 5.085311584E-02
4.970065091E-02 4.854817803E-02 3.750384768E-02 2.645939458E-02 1.322968221E-02
0.000000000E+00
massfraction-c2h5oh
0.000000000E+00 1.653158135E-13 2.282679404E-12 1.703442535E-11 8.714023393E-11
3.374624798E-10 1.053572829E-09 2.761064068E-09 6.233349707E-09 1.600099654E-08
4.789379080E-08 1.675268460E-07 6.698330762E-07 1.571741156E-06 3.382876304E-06
7.740165722E-06 1.654207866E-05 6.895217790E-05 2.770162063E-04 9.880446138E-04
3.054270547E-03 8.118314595E-03 1.861056364E-02 3.723036825E-02 6.611667820E-02
1.063561097E-01 1.583547691E-01 2.227520813E-01 3.009720871E-01 3.480108491E-01
3.951206399E-01 5.081196413E-01 5.758156322E-01 6.096654587E-01 6.265906335E-01
6.350532696E-01 6.435159338E-01 7.246136544E-01 8.057118426E-01 9.028559997E-01
1.000000000E+00
massfraction-n2
7.445408951E-01 7.379059702E-01 7.323669751E-01 7.277428885E-01 7.238825896E-01
7.206599191E-01 7.179695561E-01 7.157235763E-01 7.138485782E-01 7.115916006E-01
7.088880638E-01 7.056496129E-01 7.017704115E-01 6.994470469E-01 6.971236823E-01
6.943406234E-01 6.915575645E-01 6.848901506E-01 6.769035412E-01 6.673367241E-01
6.558770439E-01 6.421499841E-01 6.257069274E-01 6.060104946E-01 5.824169819E-01
```

```
5.541553241E-01 5.203018955E-01 4.797503242E-01 4.311753349E-01 4.020823859E-01
3.729894369E-01 3.032910435E-01 2.615466843E-01 2.406745047E-01 2.302384149E-01
2.250203700E-01 2.198023251E-01 1.697985462E-01 1.197947674E-01 5.989738368E-02
0.000000000E+00
```

A.2 The Flamelet Generated Manifold Table

Likewise, a part of the table generated from the FGM model is shown in the following. Although the whole shape is similar to the steady flamelet table, the configuration is different. The first point is the difference in the heading of the table. While in the steady flamelet, each flamelet represent a specific scalar dissipation rate, the mixture fraction is specified in the header. Then, for different progress variables from 0 (pure mixing) to 1 (complete combustion), the values of species mass fractions and temperatures are given. Furthermore, since the FGM model can be used for partially premixed flames, at the end of each flamelet, the source terms which are used in the progress variable transport equation are stored.

```
HEADER
PREMIX_CHI 0.000000E+00
Z                 1.190853E-01
NUMOFSPECIES        38
GRIDPOINTS        32
PRESSURE        1.013250E+05
BODY
REACTION_PROGRESS
0.000000000E+00 5.625000000E-02 1.125000000E-01 1.687500000E-01 2.250000000E-01
2.812500000E-01 3.375000000E-01 3.937500000E-01 4.500000000E-01 5.062500000E-01
5.625000000E-01 6.187500000E-01 6.750000000E-01 7.312500000E-01 7.875000000E-01
8.437500000E-01 9.000000000E-01 9.508132748E-01 9.604275079E-01 9.668740305E-01
9.718608224E-01 9.759835686E-01 9.795270729E-01 9.826516818E-01 9.854574013E-01
9.880111737E-01 9.903602004E-01 9.925391181E-01 9.945741609E-01 9.964857158E-01
9.982899681E-01 1.000000000E+00
TEMPERATURE
1.144810127E+03 1.200716610E+03 1.255383464E+03 1.308642210E+03 1.360249366E+03
1.408427674E+03 1.454357836E+03 1.496991183E+03 1.535969561E+03 1.572929088E+03
1.606065678E+03 1.634201744E+03 1.654532870E+03 1.655666653E+03 1.643424183E+03
1.623195972E+03 1.602967760E+03 1.584694664E+03 1.581237264E+03 1.578919013E+03
1.577125699E+03 1.575643108E+03 1.574368819E+03 1.573245170E+03 1.572236198E+03
1.571317829E+03 1.570473089E+03 1.569689523E+03 1.568957695E+03 1.568270276E+03
1.567621444E+03 1.567006495E+03
massfraction-h2
0.000000000E+00 2.775696770E-04 5.155495280E-04 7.488760491E-04 9.889959886E-04
1.243219667E-03 1.512171757E-03 1.808003739E-03 2.148189426E-03 2.518664805E-03
2.957201842E-03 3.492864332E-03 4.192846004E-03 5.038451235E-03 5.917234578E-03
7.105264516E-03 8.293294454E-03 9.366497862E-03 9.569555583E-03 9.705709570E-03
9.811033269E-03 9.898107863E-03 9.972948560E-03 1.003894196E-02 1.009820025E-02
1.015213728E-02 1.020174998E-02 1.024776988E-02 1.029075107E-02 1.033112413E-02
1.036923089E-02 1.040534768E-02
massfraction-h
```

```
0.000000000E+00 1.256624012E-07 4.310148969E-07 9.380108927E-07 1.754948792E-06
3.215353555E-06 5.222517978E-06 8.044956927E-06 1.163270774E-05 1.567444733E-05
1.954370893E-05 2.169829006E-05 1.834662639E-05 8.724552770E-07 7.957604993E-07
7.320270637E-07 6.682936280E-07 6.107202133E-07 5.998269136E-07 5.925227530E-07
5.868725240E-07 5.822012924E-07 5.781863644E-07 5.746460610E-07 5.714670718E-07
5.685735485E-07 5.659120100E-07 5.634432115E-07 5.611374290E-07 5.589715629E-07
5.569272750E-07 5.549897424E-07
massfraction-ch4
0.000000000E+00 7.968105865E-04 1.261818031E-03 1.652695024E-03 2.014626940E-03
2.316466311E-03 2.585089943E-03 2.806217933E-03 2.980588024E-03 3.125200453E-03
3.241230496E-03 3.343843097E-03 3.449514532E-03 6.038695315E-03 6.204431872E-03
4.562082259E-03 2.919732646E-03 1.436120873E-03 1.155410969E-03 9.671897457E-04
8.215887548E-04 7.012155889E-04 5.977547367E-04 5.065245088E-04 4.246050024E-04
3.500416759E-04 2.814563770E-04 2.178378034E-04 1.584199955E-04 1.026077017E-04
4.992835938E-05 0.000000000E+00
massfraction-co2
7.624893882E-02 7.771055744E-02 7.932633051E-02 8.103063190E-02 8.282588099E-02
8.480994556E-02 8.698070667E-02 8.951955198E-02 9.274116255E-02 9.642487528E-02
1.011372574E-01 1.071666970E-01 1.147534696E-01 1.154355401E-01 1.065222277E-01
1.016526567E-01 9.678308575E-02 9.238417291E-02 9.155186730E-02 9.099379087E-02
9.056208355E-02 9.020517679E-02 8.989841509E-02 8.962791722E-02 8.938502567E-02
8.916394521E-02 8.896058962E-02 8.877196038E-02 8.859578642E-02 8.843030282E-02
8.827410843E-02 8.812607071E-02
massfraction-co
0.000000000E+00 6.926814641E-03 1.369947482E-02 2.038360669E-02 2.697679085E-02
3.338115953E-02 3.959883168E-02 4.544841961E-02 5.061524231E-02 5.531996282E-02
5.899601400E-02 6.135500763E-02 6.215666824E-02 6.986303106E-02 8.716477671E-02
1.004227809E-01 1.136807851E-01 1.256573649E-01 1.279234190E-01 1.294428505E-01
1.306182267E-01 1.315899491E-01 1.324251454E-01 1.331616091E-01 1.338229111E-01
1.344248298E-01 1.349784903E-01 1.354920566E-01 1.359717118E-01 1.364222612E-01
1.368475196E-01 1.372505704E-01
massfraction-o2
8.715902323E-02 7.738826974E-02 6.881995478E-02 6.051092080E-02 5.241620995E-02
4.476645288E-02 3.739041288E-02 3.041252250E-02 2.387746261E-02 1.763834401E-02
1.191189874E-02 6.876759767E-03 2.646148228E-03 5.446109483E-06 3.573400946E-09
2.627500695E-09 1.681600445E-09 8.271241896E-10 6.654512025E-10 5.570464506E-10
4.731885359E-10 4.038604179E-10 3.442728336E-10 2.917293954E-10 2.445484048E-10
2.016041568E-10 1.621029136E-10 1.254622226E-10 9.124093445E-11 5.909621796E-11
2.875590390E-11 0.000000000E+00
massfraction-o
0.000000000E+00 7.996654730E-08 3.596411255E-07 8.428054599E-07 1.580978917E-06
2.848573917E-06 4.331667449E-06 5.896722801E-06 7.076860391E-06 7.326661709E-06
6.420698650E-06 4.180302001E-06 1.316249075E-06 2.613520139E-10 1.309762012E-10
9.630603027E-11 6.163585937E-11 3.031666077E-11 2.439084555E-11 2.041747598E-11
1.734382394E-11 1.480273391E-11 1.261866457E-11 1.069278499E-11 8.963455697E-12
7.389416132E-12 5.941573349E-12 4.598578652E-12 3.344262557E-12 2.166059239E-12
1.053992852E-12 0.000000000E+00
massfraction-oh
0.000000000E+00 1.988160297E-06 6.885608639E-06 1.490270065E-05 2.657483340E-05
4.583515471E-05 6.842697300E-05 9.297176240E-05 1.135616700E-04 1.242986879E-04
1.215156012E-04 1.004220702E-04 5.895566242E-05 2.000379271E-06 1.464043785E-06
1.181393225E-06 8.987426649E-07 6.434110990E-07 5.951005501E-07 5.627074264E-07
5.376493015E-07 5.169329190E-07 4.991271683E-07 4.834263244E-07 4.693278680E-07
4.564954200E-07 4.446917985E-07 4.337429571E-07 4.235170731E-07 4.139117028E-07
4.048455177E-07 3.962527805E-07
```

```
massfraction-h2o
6.162972711E-02 7.083278902E-02 7.851457942E-02 8.587213500E-02 9.302639395E-02
9.975859106E-02 1.061908630E-01 1.121278757E-01 1.173870353E-01 1.220603794E-01
1.257724960E-01 1.282186787E-01 1.294106855E-01 1.292754758E-01 1.254692397E-01
1.209350308E-01 1.164008220E-01 1.123048575E-01 1.115298719E-01 1.110102296E-01
1.106082535E-01 1.102759265E-01 1.099902912E-01 1.097384222E-01 1.095122583E-01
1.093064034E-01 1.091170527E-01 1.089414142E-01 1.087773731E-01 1.086232862E-01
1.084778488E-01 1.083400062E-01
massfraction-c2h5oh
1.190852670E-01 9.975344120E-02 8.667671164E-02 7.477308200E-02 6.337599672E-02
5.303054243E-02 4.329173270E-02 3.444102212E-02 2.649769360E-02 1.935988074E-02
1.310859687E-02 7.813335236E-03 3.100704030E-03 1.107721175E-08 2.427839162E-10
1.785175855E-10 1.142512547E-10 5.619645067E-11 4.521206869E-11 3.784683579E-11
3.214936348E-11 2.743907425E-11 2.339057611E-11 1.982067117E-11 1.661510150E-11
1.369738450E-11 1.101359204E-11 8.524151139E-12 6.199089250E-12 4.015113739E-12
1.953732892E-12 0.000000000E+00
PREMIX_CDOT
0.000000000E+00 2.441461358E+01 1.187121304E+02 2.893271199E+02 5.584369944E+02
1.028274065E+03 1.606140054E+03 2.237341182E+03 2.744181462E+03 2.986910745E+03
2.815341298E+03 2.095209129E+03 8.739927788E+02 7.406873045E-01 4.708375169E-01
4.627043128E-01 3.442008626E-01 1.507873406E-01 1.055841526E-01 7.380080590E-02
4.841300502E-02 2.690112360E-02 8.036260734E-03 0.000000000E+00 0.000000000E+00
0.000000000E+00 0.000000000E+00 0.000000000E+00 0.000000000E+00 0.000000000E+00
0.000000000E+00 0.000000000E+00
```